

The Application Of Smooth Particle Hydrodynamics To The Modelling Of Solid Materials

By

Mark Daniel Fuller

Supervisor

Dr Simon Gill

A thesis in partial fulfillment of the requirements for the
degree of Doctor of Philosophy

University of Leicester
Engineering Department

April 2010

The Application of Smooth Particle Hydrodynamics to the modeling of solid materials

Mark Daniel Fuller

Abstract

This thesis explores the mesh-free computer modelling technique of Smooth Particle Hydrodynamics (SPH), and explores its usage in solid mechanics applications. A review of the context in which SPH can be used, the theory behind the governing equations and the adaptations carried out to enable elastic body problems to be simulated is presented. An algorithm is proposed to improve the ability for SPH to model contact between deformable surfaces.

Non-linear behaviour is simulated via the introduction of plasticity, a statistical damage model and the introduction of friction between surfaces. It is shown how SPH can successfully model the buckling in slender rods and match predictions even under extreme deformations. The culmination of these techniques is used to simulate the mechanical properties of thermal barrier coatings (TBC). The simulated effect of increasing the size of gaps in the columnar structure of TBC is shown to reduce hardness. Higher coefficients of inter-column friction are suggested to be able to enhance the load bearing properties of the TBC system.

The future research and improvements to the SPH technique are explored along with a discussion about the appropriate methodology of adapting SPH to meet a range of modelling requirements.

Acknowledgements

*I would like to thank my supervisor Simon for his patients
and giving me the freedom to really explore this challenging topic.*

My parents for fostering my love of all things science,

and

Sarah who has encouraged me throughout the whole process.

Thank you all.

Contents

1. Introduction

1.1. Scope of Research	1
1.2. Computational Models	3
1.3. Mesh-free Methods	5
1.4. Smooth Particle Hydrodynamics	6
1.5. Rival Techniques	8

2. Smooth Particle Hydrodynamics

2.1. Introduction	11
2.2. The SPH Formulation	12
2.2.1. The Kernel Approximation	12
2.2.2. Utilization of the Kernel	15
2.3. Continuity Equation	17
2.4. Eqn. of State for a linear elastic solid	19
2.5. Acceleration Equation	22

3. SPH with Elasticity

3.1. Introduction	26
3.2. Quasi-static analysis of stress in a plate containing a circular hole	27
3.3. Elastic Collisions and XSPH	30
3.3.1. Interactions with a solid wall	30
3.3.2. Conservation of Linear Momentum	33
3.4. Conservation of Angular Momentum	36
3.5. Colliding Rubber Rings and the Tensile Instability Correction	40
3.6. Summary	43

4. Contact Mechanics

4.1. Impact Dynamics	44
4.2. The Standard SPH Approach	46
4.3. Penetration Algorithm	48
4.3.1. Identifying Surfaces	49
4.3.2. Creation of Normal Vectors	53
4.3.3. Improved Surface Evaluation	54
4.3.4. Penalty Force	57
4.3.5. Simulations	58
4.4. Friction	59
4.4.1. Simulations of Friction	61
4.4.2. Rolling Contact	65
4.5. Summary	66

5. Non-linear Materials

5.1. Introduction	67
5.2. Elasto-plasticity	68
5.2.1. Indentation of an elasto-plastic substrate	69
5.3. Damage Mechanics	73
5.3.1. Modeling failure through the kernel	73
5.3.2. Continuum damage models	76
5.4. Summary	82

6. Buckling

6.1. Introduction	83
6.2. Classic beam bending theory	84
6.3. SPH simulations of buckling	89
6.4. Summary	98

7. Thermal Barrier Coatings

7.1. Introduction	99
7.2. SPH simulations of TBCs	103
7.2.1. Deformation mechanism	105
7.2.2. Force-displacement curves	108
7.2.3. Effect of material and geometric parameters	110
7.3. Summary	113

8. Conclusions

8.1. General Observations	114
8.2. Adaptations	115
8.3. Complete Lagrangian method	116
8.4. A multi-CPU approach	118
8.5. Future Applications	122

Appendix A

References

Introduction

1

1.1. Scope of Research

This research considers the utilization of Smooth Particle Hydrodynamics (SPH) in the modelling of solid materials. This technique has been widely used in other fields, such as the collisions between proto-planetary bodies in Fig.1.1, but has yet to be fully exploited in a mechanical engineering context. Here we investigate improvements to the SPH method especially the potential to model problems containing contact between dissimilar materials; whilst still maintaining the core benefits that result from using the SPH method; most notably the natural handling of large deformations. The accuracy of the SPH approach is studied in a series of benchmark problems, and its validity as a method is assessed.

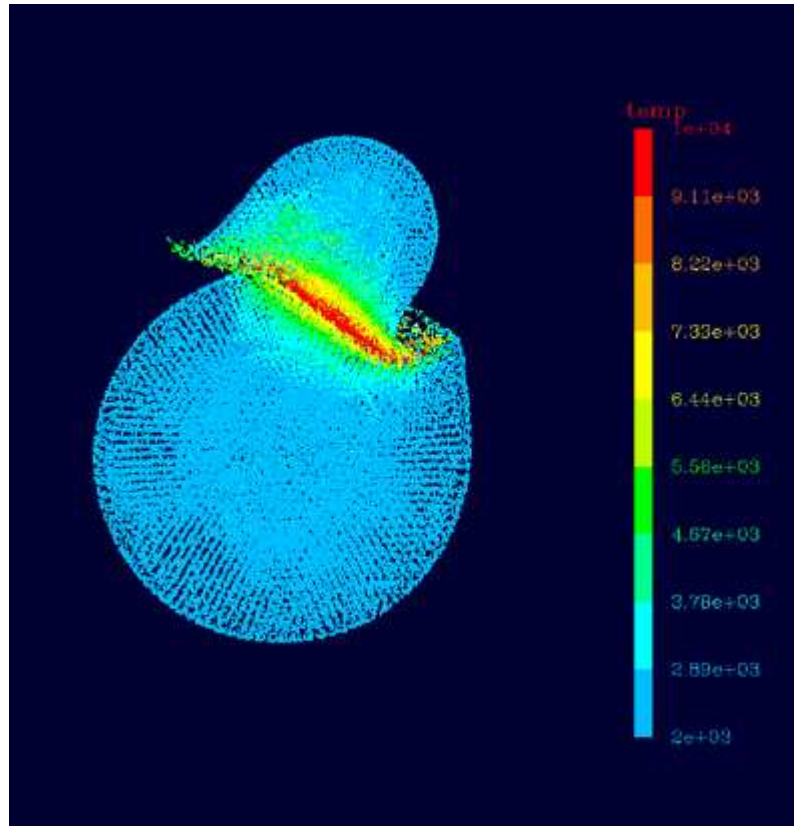


Fig.1.1. SPH simulation of the “Origin of the Earth-Moon system” from <http://www.boulder.swri.edu/science.php>, Southwest Research Institute, 1050 Walnut St, Suite 300, Boulder, CO 80302.

The remaining sections in this chapter provide a brief introduction to the topic, detailing some of the research already carried out in associated areas. Chapter 2 looks at the SPH methodology in more depth, deriving the governing equations for elastic body simulations. Chapter 3 uses these equations to simulate a variety of models with more specific attention to the pro and cons of this method when applied to elastic solids. With these limitations in mind Chapter 4 details the penalty force method developed in order to allow materials to interact across boundaries, and introduces a friction co-efficient. Chapter 5 deals with some non-linear material behaviour by looking at plastic deformation and damage modelling. A non-linear geometry is discussed in Chapter 6 as SPH is applied to the buckling of bars. Chapter 7 begins the process of using these developments in the analysis of Thermal

Barrier Coatings (TBC). These coatings have developed as a way of protecting materials from extremes of heat by depositing an insulating surface with a columnar microstructure. These columns interact with one another and can deform and fracture leading a loss of performance and increased susceptibility to further damage. This makes thermal barrier coatings an ideal candidate for simulation using this contact enabled SPH method. Chapter 8 looks into the potential for this method and where further enhancements might be made to improve analysis of TBCs and into other areas of interest. Appendix A contains setup data for the SPH simulations studied in depth from Chapter 3 onwards.

1.2. Computational Models

A scientific model reduces the intrinsic complexities of any real world problem down into simpler constituent parts. The skill of the engineer is to determine which elements can be safely removed without compromising the integrity of the whole. Creating a model of a situation is essential in order to understand and convey the information about materials to others.

The methodology of computational models is no different to the analytical solutions derived from the scientific model. They still require the skill to determine the required elements that can be safely removed but still produce reliable information. It is easy to over-burden a modern computational simulation with too much physics and forget the basic principles of a model. Each addition or removal of new physical phenomena should show how this individual element affects the overall results.

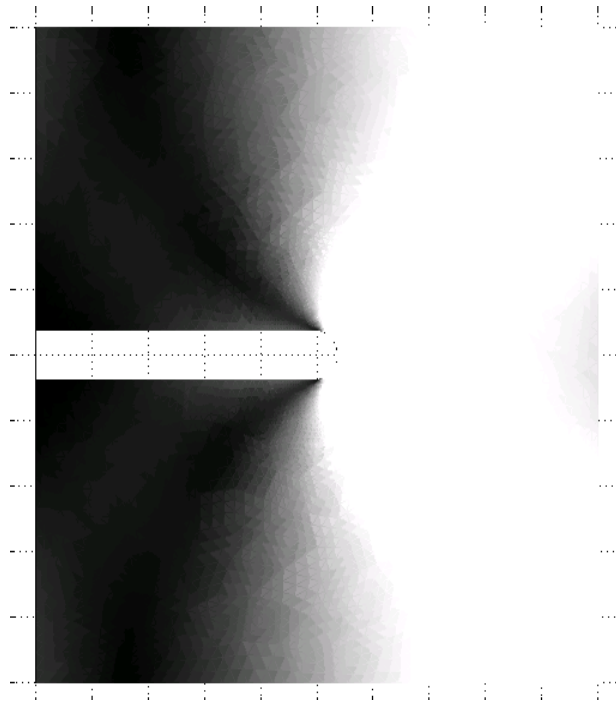


Fig.1.2: A Finite Element simulation using FEMLAB, showing the stress distribution caused by a pseudo-crack. Constructed from approximately 16000 interconnecting nodes, the triangular mesh structure is clearly visible in the shading of the von-Mises stresses.

Computational models are becoming increasingly powerful and are a fantastic way to simulate models that would be otherwise impossible to do analytically. The Finite Element Method (FEM) is the favoured model for engineering applications; the software package FEMLAB, used to generate the image in Fig. 1.2 is in wide use and is suitable to a wide range of problems including mechanical, thermal and electrical engineering. It uses a grid to discretize the problem into elements that describe the dependency relative to its neighbours. This grid is better described as a mesh since there is no reason for the element to be regular. This fact allows additional elements to be located at the point of interest increasing resolution and accuracy.

1.3. Mesh-free Methods

For dynamically evolving problems such as crack growth, a FEM mesh requires recalculating at every time step, a cumbersome task that increases the computational complexity immensely; hence the need for a mesh-less method of modelling. Various approaches are available to attempt such a move away from grid-based models. The diffuse element method (Nayroles et al., 1992), the element free Galerkin method (Belytschko et al., 1994) and smooth particle hydrodynamics (Monaghan, 1988). These techniques use a scattered set of nodes in the region of interest which are free to deform and hence sidestep the costly re-meshing procedure required by FEM.

In these methods the array of nodes are generated from the deforming material (*Lagrangian*), as opposed to background spatial co-ordinates (*Eulerian*). This allows particles to flow with the material and deform along with it. Particle interactions are moderated by a shape function which is based on the local coordinates and material properties. The main computational expense often comes from the nearest neighbour analysis that is required to determine the locality of particles. Although there are many techniques to speed this process along, the most famously effective probably being tree-based algorithms (see Hernquist and Katz, 1989).

Many techniques, either by design or through necessity, use a combination of Lagrangian and Eulerian methods or a grid and particle approach (e.g. Sulsky and Schreyer, 1996). These hybrid methods have shown promise, but as previously discovered by attempting to couple SPH and FEM in the same simulation, Wang et al. (2005) have shown the methods are not always compatible.

1.4. Smooth Particle Hydrodynamics

One of the original mesh-less methods to be developed was Smooth(ed) Particle Hydrodynamics, or SPH it has been available as a technique since the late 1970's when computational power began to make modelling on academic machines possible. For many years it remained confined to the astrophysical flows it was designed to model, situations that were too distant to view directly and no other technique could compete. The interest remains since SPH predicted gross behaviour that matched with observational results well, even if there were doubts over the mathematical robustness of its assumptions. It is only recently that SPH has begun to be directly compared against other modelling techniques in alternative disciplines, see Fig.1.3 that applies our in-house SPH code to the problem of crack propagation.

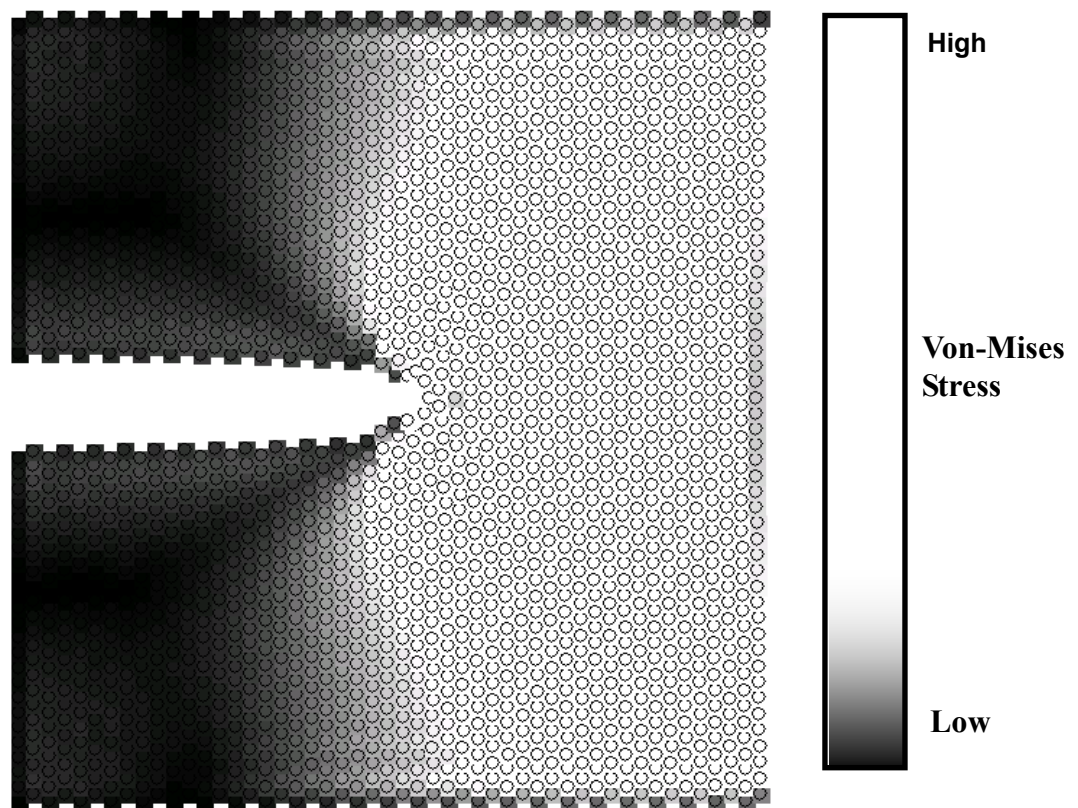


Fig.1.3: An SPH particle based mesh-free model, mimicking the FEM simulation from Fig.1.2. Constructed from approximately 2500 particles.

One such comparison, of a Riemann Shock Tube in Monaghan (1997) follows the SPH method through the mathematics, assumptions and finally compares to known analytical results and other models values. The work itself shows how well SPH can handle fluid dynamic problems in a variety of forms and also details information about the viscosity parameters and extending the method with additional parameters such as thermal energy equations. Still its purpose was to validate SPH in relativistic problems so as to model high speed gas jets forming pulsars and other magneto-hydrodynamics astrophysical simulations. The first complete attempt to move into solid material SPH models by Monaghan (1992) demonstrated the problem of particle clustering (see Section 3.5) called here the *tensile instability*. A variety of methods are used to show stability and correct for any potential clumping. The most vivid demonstration occurs with two colliding rubber rings, which when modelled without instability removal, seem to unrealistically split and reform during impact. The reduction of the tensile instability is taken further by Gray, Monaghan and Swift (2001), in a paper which concentrates solely on modelling elastic behaviour with SPH. Here clumping is resisted by a powerful short ranged force which acts on any principal stress that is compressive. This improved method is shown to work in a variety of solid material problems including the bouncing rings, sinusoidal and highly non linear oscillations.

Monaghan recognizes and discusses the merits of other authors in enhancing the SPH method and in Gray, Monaghan and Swift (2001) particular attempts to remove the tensile instability. The most common discussion comes from the selection and properties of the smoothing kernel. Oger and Savage (1999) suggest a quadratic kernel which is shown to minimize the effect of discontinuities, in this particular example, at the edge of a broken-ice field. A more robust selection technique has

been laid down in Capuzzo-Dolcetta and Lisio, (2000) where some mathematical postulates are given for the selection of a kernel, concerning the smoothness of the first and second derivative of the kernel and its ability to correctly interpolate polynomials up to certain orders (linear and higher-order completeness)

Bonet and Kulasegram, (2002) offers a number of corrections collectively known as the Corrected-SPH (CSPH) method. One concerns the *kernel* allowing superior interpolation between randomly distributed SPH particles and also a less computationally intensive approximation that offers similar results. The second method is an integration corrector step which further enhances the prediction of values. Finally, an improved stabilization method which prevents individual particle vibrations from adversely influencing results. These techniques are drawn together by Rodriguez-Paz and Bonet, (2003) which uses CSPH to model avalanches and debris flows in mountainous regions. This paper is also significant as it addresses the problems of solid boundaries (i.e the mountain side) and SPH.

More recently research has suggested that the kernel should adapt to the deforming material not only in size (as in adaptive-h schemes), but also in shape. The moving-least-squares method, (Dilts, 1999) adapts the kernel to give better edge definition. But this is taken further by Ted Belytschko, and his collaborations with Rabczuk, Belytschko and Xioa (2004) who keep the same particles attached to the kernel for the entire length of the simulation, a so called Lagrangian kernel. It is believed that a kernel based about special co-ordinates, as traditional (Eulerian) kernels are, do not effectively combine with the Lagrangian SPH method which follows material points, this mismatch causes issues such as the tensile instability. The kernel may also become very distorted, so is not as suitable for simulating extreme deformations.

1.5. Rival Techniques

The work in this thesis has attempted to extend the list of problems in solid mechanics that SPH can handle, but there are competing methods, most are based around the Finite Element Methodology (FEM). Fortino and Bilotta, (2004) summarises previous efforts to predict crack growth and uses the latest energy methods to perform a 2D crack growth simulation using '*Partition of Unity*' FEM to prevent remeshing. However, the crack growth in this example only follows a straight path. It is papers (Belytschko & Black, 1999), (Stolarska et al., 2001) and (Ventura et al., 2003) that describe the evolution of directional crack prediction with eXtended-FEM and the 'Vector Level Set Method' (based on the Partition of Unity Idea). Although, this method is not yet flexible enough to support crack branching. Other techniques are available which attempt to combine a computationally intensive completely meshless method (such as Rao and Rahman, 2001) the element-free Galerkin Method, surrounded by regular FEM. However the coupling of the two regions still causes difficulties at the boundary. Finally, a new combinational method which attempts to overcome this boundary problem is the Material Point Method. Crack growth has been introduced by Guo and Nairn (2004) allowing the underlying grid to be split in a similar way to the Partition of Unity scheme. The Material Point Method is different from other grid based solutions because only the velocity field is updated via the underlying mesh, giving the ability to better handle solid boundaries.

While these methods exist few have attempted to add plasticity, as in Hammouda et al. (2004) and/or interfaces in heterogeneous media (Joyce et al. 2003) and (Jiang et al. 2003). SPH on the other hand has been shown to work with these features, at the

moment independently, but the simplicity with which SPH can be extended to include new factors allows the coupling of plasticity and composites in multi-dimensions. Dynamic 3D simulations are computationally intensive but again SPH is naturally scalable to multiprocessor super-computer systems. In addition, it is the near optimal application for cluster systems which have been shown to be many times more cost effective than traditional super computers (Synder, 2003). Using the interprocessor communication language MPI, (Jimmack & Touheed, n/d), parallel versions of SPH with fluids (Kowalenko, 2006) and complex load balancing schemes (Mandell et al. 1996) have been demonstrated. The Los Alamos National Laboratory have a version of SPH called SPHinx which has been used for 3D solid material models in the design of ceramic armours. This paper also reviews the damage model, which is used to statistically model fracture so that each SPH particle has its strength reduced on a ratio to how damaging it is. The effectiveness in high resolution runs can be seen in Mandell et al.(1996).

This demonstrates the possibilities of SPH in many different fields, but it still has unique properties that when harnessed can achieve where other modelling techniques can not.

Smooth Particle Hydrodynamics



2.1 Introduction

Smooth Particle Hydrodynamics (SPH) was originally developed by Gingold and Monaghan (1977) to model astrophysical phenomenon such as galaxy collisions, solar accretion discs and planetary formation. Later work has enabled its use in fluid mechanics, and more recently modelling elastic behaviour in solids by Gray, Monaghan and Swift (2000).

One of the first *mesh-free* methods to be developed, SPH became a driving force behind the search for alternative techniques to FEM. Originally designed for hydrodynamic flows, instead of a background mesh, a smoothing kernel is used to moderate interactions between particles that discretize the area of interest.

In common with the majority of mesh-free approaches SPH allows large particle displacements to take place without reference to any underlying mesh or grid structure to calculate properties. The initial distribution of particles may be based on

a regular Cartesian grid, or any other co-ordinate system as prescribed by the problem. In an effort to distinguish an array of particles from a regular grid or mesh found in other techniques, in this thesis it is suggested the term a *map* of SPH particles is used.

2.2 The SPH Formulation

SPH is able to incorporate new physics by addition of and modification of the governing equations laid out below. In this way the original hydrodynamic code has been added to and adapted to new problems such as elastic solids.

2.2.1. The Kernel Approximation

Any function can be represented exactly by

$$f(x) = \int f(x_a) \delta(x - x_a) dx \quad (2.1)$$

where $\delta(x - x_a)$ represents the Dirac delta function, a point action that has zero width (infinitely compact) but with an area equal to unity. This way the continuous sum at point x_a is exactly represented.

SPH utilises a smoothing kernel to model particle interactions which has finite compactness, $W(r)$ with a normalized area (2.3) & (2.4) to replace $\delta(x - x_a)$. A kernel with *compact support* has a small range, outside of which is it zero. The width of the kernel is measured by its h -value, and commonly evaluated between 0 and $2h$.

$$f(x) = \int_0^{2h} f(x_a)W(r)dr \quad (2.2)$$

where $r = x - x_a$ in one-dimension. The kernel is subject to

$$\int_A W(r)rdr = 1 \quad (2.3)$$

Or, for a typical 2D radially symmetric kernel,

$$2\pi \int_0^{\infty} W(r)rdr = 1 \quad (2.4)$$

Traditionally the kernel is defined as a *cubic spline*, as defined (along with alternative kernels) in Capuzzo-Dolcetta and Lisio (2000) by

$$W(r, h) = C \begin{cases} 1 - \frac{3}{2}q^2 + \frac{3}{4}q^3, & 0 \leq q \leq 1 \\ \frac{1}{4}(2-q)^3, & 1 \leq q \leq 2 \\ 0. & q \geq 2 \end{cases} \quad (2.5)$$

where

$$q = r_{ab}/h \quad (2.6)$$

r_{ab} is the distance between particles a and b and h represents the kernel range parameter.

A normalization constant, C , is required to meet requirement (2.3) that area/volume generated by the kernel should equal unity

$$C = \left[\frac{2}{3}h^{-1}, \frac{10}{(7\pi)}h^{-2}, \frac{1}{\pi}h^{-3} \right] \text{ in } [1D, 2D, 3D] \quad (2.7)$$

The function is shown normalised in fig. 2.1

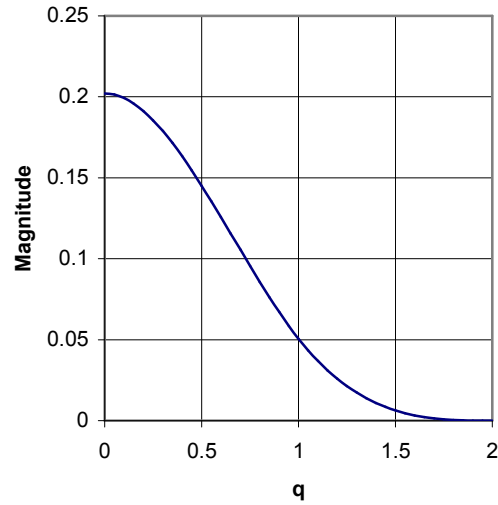


Fig. 2.1 A radial slice along the 2D form of the cubic spline kernel defined by (2.5) and normalized by the 2D form in (2.7)

This absolute value of the smoothing function is rarely used in SPH codes, except for the basic density evaluation and by XSPH velocity smoothing. Instead it is the gradient of the kernel that is used to determine the evolution of time dependent terms.

The kernel 1st derivative, as a function of position, is written as

$$\nabla_a W_{ab} = \frac{dW(r)}{dr} \Big|_{r=r_{ab}} \left(\frac{\partial r}{\partial x_a}, \frac{\partial r}{\partial y_a}, \frac{\partial r}{\partial z_a} \right) \quad (2.8)$$

where

$$\frac{\partial r}{\partial x_a} = \frac{(x_b - x_a)}{r_{ab}} \dots \quad (2.9)$$

Or in the more generalized form,

$$\frac{dW}{dr}(r, h) = \frac{C}{h} \begin{cases} -3q + \frac{9}{4}q^2 & 0 \leq q \leq 1 \\ -\frac{3}{4}(2-q)^2 & 1 \leq q \leq 2 \\ 0 & q \geq 2 \end{cases} \quad (2.10)$$

The derivative of the kernel function for the 2D case is illustrated in Fig. 2.2.

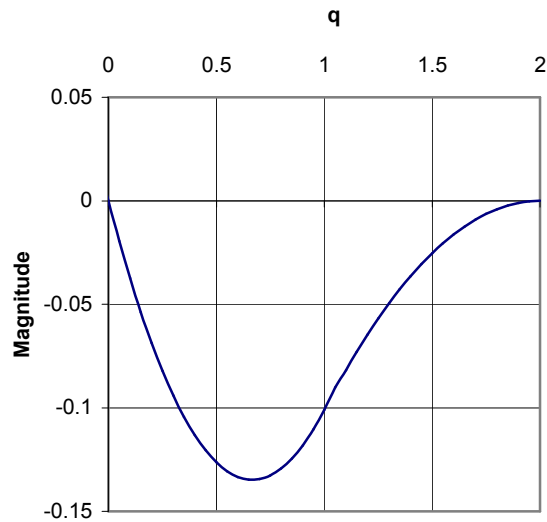


Fig.2.2. Normalized 1st spatial derivative of the cubic spline kernel defined by (2.10) and normalized by the 2D form of (2.7)

2.2.2. Utilization of the kernel

In the SPH formulism, a physical property can be represented starting from the Dirac function in (2.1), and introducing ρ the density about x_a , such that

$$f(x) = \int_0^{\infty} \frac{f(x_a)}{\rho} \delta(x - x_a) \rho dx \quad (2.11)$$

Replacing $\delta(x - x_a)$ with the kernel approximation, $W(r, h)$ the solution is no longer exact, but depends on the choice of kernel.

$$f(x) \approx \int_0^{2h} \frac{f(x_a)}{\rho} W(r, h) \rho dr \quad (2.12)$$

Changing from the continuous definition to the discrete array of SPH particles, sum over all neighbouring particles within $2h$ of x_a . The mass associated with each neighbour is generated from the mass element $\rho dr = m_b$ such that now

$$f(x) \approx \sum_b \frac{m_b}{\rho_b} f(x_b) W(r, h) \quad (2.13)$$

The selection of h introduces a characteristic length scale which may reproduce an unphysical response to a simulation. The value of h determines the number of particles that the *kernel* interacts with. In Monaghan (1997), h is given the constant value 1.5, which represents a 3 particle radius. Although global support ($h \sim$ size of simulation) or variable- h schemes have been investigated, a local constant h offers a practical and efficient computation.

For the constitutive laws, spatial derivatives are required and SPH interpolation can be used to estimate values through an array of disordered points. *SPH Interpolation* of velocity change gives, where standard tensor suffix notation is often replaced by superfix to avoid misunderstanding,

$$\left(\frac{dv^i}{dx^j} \right)_a = - \sum_b \frac{m_b}{\rho_b} (v_a^i - v_b^i) \frac{\partial W_{ab}}{\partial x^j} \quad (2.14)$$

where v_a^i is the velocity of particle a in the i th direction, etc.

2.3. Continuity Equation

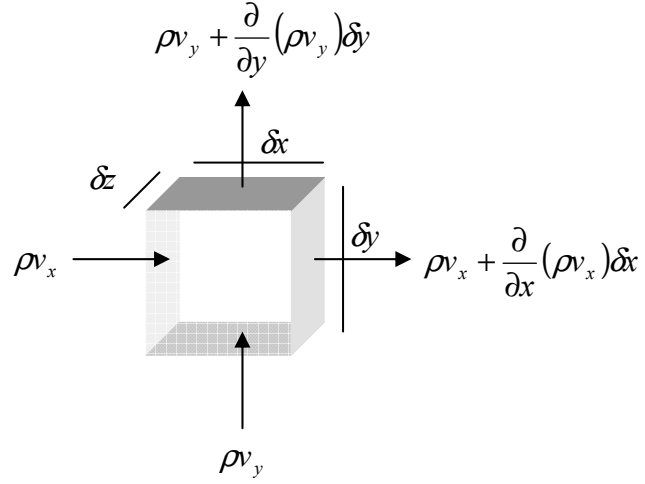


Fig.2.3. Diagram of a single mass element and associated fluxes.

For a compressible medium, the difference between the mass entering the element and the mass leaving the system must be associated with a change in its density.

In differential form the continuity equation becomes,

$$\frac{\partial \rho}{\partial t} + \rho \left(\frac{\partial v_x}{\partial x} + \frac{\partial v_y}{\partial y} \right) = 0 \quad (2.15)$$

Applying the kernel approximation to (2.15) and rearranging gives

$$\dot{\rho} = - \int_V \rho v_{j,j} W(r) dV \quad (2.16)$$

where $\dot{\rho}$ denotes differentiation with respect to time and Ω_a is the kernel volume associated with particle a . For simplicity, further manipulation is carried out for the 1D case. With a kernel range between $2h$ and $-2h$, (2.16) becomes

$$\dot{\rho} = - \int_{-2h}^{2h} \rho v_x W(x) dx \quad (2.17)$$

Integrating by parts gives

$$\dot{\rho}_a = -\left[\rho v_x W(x)\right]_{-2h}^{2h} + \int_{-2h}^{2h} \rho v_x \frac{dW(x)}{dx} dx \quad (2.18)$$

By definition of the kernel with compact support, $W(\pm 2h) = 0$ so the first term in

(2.18) cancels out leaving

$$\dot{\rho}_a = \int_{-2h}^{2h} \rho v_x \frac{dW(x)}{dx} dx \quad (2.19)$$

Discrete formulation summing over all nearest neighbours, b and mass

element $m_b = \rho dx$,

$$\dot{\rho}_a \approx \sum_b m_b \left(v_a \frac{\partial W}{\partial x_a} + v_b \frac{\partial W}{\partial x_b} \right) \quad (2.20)$$

where the v_a term has been artificially introduced in order to ensure that the divergence vanishes for a uniform velocity distribution. The gradient of a well defined kernel is anti-symmetric, so $\nabla_a W_{ab} = -\nabla_a W_{ba}$. Therefore the SPH continuity equation is

$$\dot{\rho}_a \approx \sum_b m_b (v_a - v_b) \frac{\partial W}{\partial x_b}. \quad (2.21)$$

The instantaneous density around particle a , can also be calculated by summing over the neighbouring particles such that

$$\rho_a = \sum_b m_b W_{ab} \quad (2.22)$$

However this process introduces boundary errors as the *kernel* is ill defined where particle are not evenly distributed throughout the *kernel*. Therefore, the Continuity Equation (2.21) is the preferred option as it keeps track of particle movements rather than wholesale recalculation of (2.22) which may introduce boundary errors.

2.4. Equation of State for a linear elastic solid

In three-dimensions, the state of an isotropic, homogenous material that satisfies

Hooke's Law, with Young's Modulus, E , can be represented by a strain tensor (ϵ_{ij})

and a stress tensor (σ_{ij}) which are related by

$$\begin{bmatrix} \epsilon_{11} \\ \epsilon_{22} \\ \epsilon_{33} \\ 2\epsilon_{23} \\ 2\epsilon_{31} \\ 2\epsilon_{12} \end{bmatrix} = \frac{1}{E} \begin{bmatrix} 1 & -\nu & -\nu & 0 & 0 & 0 \\ -\nu & 1 & -\nu & 0 & 0 & 0 \\ -\nu & -\nu & 1 & 0 & 0 & 0 \\ 0 & 0 & 0 & 2(1+\nu) & 0 & 0 \\ 0 & 0 & 0 & 0 & 2(1+\nu) & 0 \\ 0 & 0 & 0 & 0 & 0 & 2(1+\nu) \end{bmatrix} \begin{bmatrix} \sigma_{11} \\ \sigma_{22} \\ \sigma_{33} \\ \sigma_{23} \\ \sigma_{31} \\ \sigma_{12} \end{bmatrix} \quad (2.23)$$

where ν is Poisson's ratio. This can be simplified by using Suffix notation to

$$\epsilon_{ij} = \frac{(1+\nu)}{E} \sigma_{ij} - \frac{\nu}{E} \delta_{ij} \sigma_{kk} \quad (2.24)$$

where δ_{ij} represents the Kronecker delta function, for which

$$\delta_{ij} = \begin{cases} 1 & \text{if } i = j \\ 0 & \text{if } i \neq j \end{cases} \quad (2.25)$$

Similarly, a 3D Stress can be represented as,

$$\sigma_{ij} = 2\mu\epsilon_{ij} + \lambda\delta_{ij}\epsilon_{kk} \quad (2.26)$$

where Lamé's first parameter is given by

$$\lambda = \frac{2\nu}{(1-2\nu)} \mu \quad (2.27)$$

and Lamé's second parameter (or shear modulus) is

$$\mu = \frac{E}{2(1+\nu)} \quad (2.28)$$

The Stress Tensor is broken into two parts; the Hydrostatic Stress (P) and the deviatoric stress (S), such that

$$\sigma_{ij} = P\delta_{ij} + S_{ij} \quad (2.29)$$

Hydrostatic Pressure can be written as

$$P = -\frac{1}{3}\sigma_{kk}, \quad (2.30)$$

so the deviatoric stress is therefore

$$S_{ij} = \sigma_{ij} - \frac{1}{3}\sigma_{kk}\delta_{ij}. \quad (2.31)$$

where σ_{kk} represents only the diagonal parts (trace) of the stress tensor, so has no shape changing properties.

Implementing the stress relation (2.26) for σ_{kk} , and dividing through by 3,

$$\frac{\sigma_{kk}}{3} = \left(\frac{2\mu + 3\lambda}{3}\right)\epsilon_{kk} \quad (2.32)$$

and similarly for the strain relation (2.24) for ϵ_{kk} ,

$$\epsilon_{kk} = \left(\frac{(1+\nu)}{E} - \frac{3\nu}{E}\right)\sigma_{kk} \quad (2.33)$$

one finds that

$$\sigma_{kk} = \frac{E}{(1-2\nu)}\epsilon_{kk}. \quad (2.34)$$

or

$$K\epsilon_{kk} = \frac{1}{3}\sigma_{kk} \quad (2.35)$$

where

$$K = \frac{E}{3(1-2\nu)} \quad (2.36)$$

is known as the bulk modulus.

Rewriting the deviatoric stress (2.31) in terms of the bulk modulus and Lamé's parameters (2.27) yields

$$S_{ij} = 2\mu\varepsilon_{ij} + \lambda\delta_{ij}\varepsilon_{kk} - K\varepsilon_{kk}\delta_{ij} \quad (2.37)$$

$$= 2\mu\varepsilon_{ij} + (\lambda - K)\delta_{ij}\varepsilon_{kk} \quad (2.38)$$

where $(\lambda - K) = \lambda\left(\frac{2}{3}\mu + \lambda\right) = -\frac{2\mu}{3}$

Finally, the deviatoric stress can be written as

$$S_{ij} = 2\mu\left(\varepsilon_{ij} - \frac{1}{3}\delta_{ij}\varepsilon_{kk}\right) \quad (2.39)$$

and consequently the rate of change in the deviatoric stress is given by

$$\dot{S}_{ij} = 2\mu\left(\dot{\varepsilon}_{ij} - \frac{1}{3}\delta_{ij}\dot{\varepsilon}_{kk}\right) \quad (2.40)$$

However, SPH uses a Lagrangian Frame of Reference, to enable it to be used for large deformation analysis. In this case, the algorithm follows the path of particles as they deform and rotate.

A tensor, T (in x, y, z) will transform into new coordinates, tensor \hat{T} (in x', y', z')

following

$$\hat{T} = R T R^T \quad (2.41)$$

where R is a rotation matrix. The rate of change of tensor, \hat{T} is given by

$$\dot{\hat{T}} = R \dot{T} R^T + \dot{R} T R^T + R T \dot{R}^T \quad (2.42)$$

For small changes, $R \approx I$, (the Identity Matrix) and \dot{R} becomes the rotation tensor

$$\Omega_{ij} = \frac{1}{2}\left(\frac{\partial v_i}{\partial x_j} - \frac{\partial v_j}{\partial x_i}\right) \quad (2.43)$$

Applied to the deviatoric stress tensor

$$\begin{aligned}\hat{S} &= \dot{S} + \Omega S + S \Omega^T \\ &= \dot{S} + \Omega S - S \Omega\end{aligned}\tag{2.44}$$

where the second line takes advantage of the asymmetric nature of the rotation matrix, i.e. $\Omega^T = -\Omega$.

Using the definition of the deviatoric stress, S , as given by (2.40) and (2.44), the rate of change in deviatoric stress in the Lagrangian frame of reference is

$$\frac{dS_{ij}}{dt} = \underbrace{2\mu\left(\dot{\epsilon}_{ij} - \frac{1}{3}\delta_{ij}\dot{\epsilon}_{kk}\right)}_{\text{StressTerm}} + \underbrace{\Omega_{ik}S_{kj} - S_{ik}\Omega_{kj}}_{\text{RotationTerms}}\tag{2.45}$$

where

$$S_{ij} = \sigma_{ij} - \frac{1}{3}\sigma_{kk}\delta_{ij}\tag{2.46}$$

and the strain rate tensor

$$\dot{\epsilon}_{ij} = \frac{1}{2}\left(\frac{\partial v_i}{\partial x_j} + \frac{\partial v_j}{\partial x_i}\right)\tag{2.47}$$

2.5. Acceleration Equation

The momentum generated by a system can be defined in terms of the Lagrangian of all the particles in the system,

$$L = \int (\text{Total Energy}) dV = \int \left(\frac{1}{2}v_b^2 - u_b\right)\tag{2.48}$$

where $\frac{1}{2}v_b^2$ is the kinetic energy of particle b and u_b is its internal energy.

Discretized by SPH this becomes

$$L = \sum_b m_b \left(\frac{1}{2}(v_b)^2 - u_b\right)\tag{2.49}$$

The Euler-Lagrange Equation states,

$$\frac{d}{dt} \left(\frac{\partial L}{\partial v_a} \right) - \frac{\partial L}{\partial r_a} = 0 \quad (2.50)$$

In SPH

$$\left(\frac{\partial L}{\partial v_a} \right) = \sum_a m_a v_b \quad (2.51)$$

and

$$\frac{\partial L}{\partial r_a} = \sum_b m_b \frac{\partial u_b}{\partial r_a} \quad (2.52)$$

Rewriting the change in internal energy in terms of the change in densities

$$\frac{\partial u_b}{\partial r_a} = \frac{\partial u_b}{\partial \rho_b} \frac{\partial \rho_b}{\partial r_a} \quad (2.53)$$

The 1st law of thermodynamics allows the following assumptions to be made

$$\left. \frac{\partial u_b}{\partial \rho_b} \right|_s = \frac{P_b}{\rho_b^2} \quad (2.54)$$

The spatial derivative of the SPH density function, $\rho_a = \sum_b m_b W_{ab}$, is

$$\frac{\partial \rho_b}{\partial r_a} = \sum_c m_c \nabla_a W_{bc} (\delta_{ba} - \delta_{ca}) \quad (2.55)$$

Substituting (2.52), (2.53) and (2.55), the following relation is obtained,

$$\frac{\partial L}{\partial r_a} = \sum_b m_b \frac{P_b}{\rho_b^2} \sum_c m_c \nabla_a W_{ba} (\delta_{ba} - \delta_{ca}) \quad (2.56)$$

As the gradient of a well defined kernel is anti-symmetric, $\nabla_a W_{ac} = -\nabla_a W_{ca}$ the

function can be simplified to be

$$\frac{\partial L}{\partial r_a} = m_a \sum_b m_b \left(\frac{P_a}{\rho_a^2} + \frac{P_b}{\rho_b^2} \right) \nabla_a W_{ab} \quad (2.57)$$

Hence acceleration of any particle, b can be defined by,

$$\frac{dv_a}{dt} = -\sum_b m_b \left(\frac{P_a}{\rho_a^2} + \frac{P_b}{\rho_b^2} \right) \nabla_a W_{ab} \quad (2.58)$$

The actual SPH form of the Acceleration equation (Monaghan, 1999) is derived from this discretized form of Newton's second law of motion. It is the sum of the forces acting upon a single point

$$\frac{dv_a^i}{dt} = \sum_b m_b \left(\frac{\sigma_a^{ij}}{\rho_a^2} + \frac{\sigma_b^{ij}}{\rho_b^2} + \Pi_{ab} \delta^{ij} \right) \frac{dW_{ab}}{dx_a^j} + g^i \quad (2.59)$$

The acceleration of particle a is found by summing over the neighbouring particles b , inside the kernel range. The σ_a and σ_b terms operate to ensure pair-wise symmetry, thus ensuring conservation of momentum. The artificial viscosity term, $\Pi_{ab} \delta^{ij}$, is introduced to cope with shock waves which propagate when rapid changes in velocity are made. It applies when $i=j$ (i.e. it is only valid for non-shear terms) and is given by

$$\Pi_{ab} = -\alpha \frac{h \mathbf{v}_{ab} \cdot \mathbf{r}_{ab}}{\rho_{ab} |\mathbf{r}_{ab}|^2} \left(c_{ab} - 2 \frac{h \mathbf{v}_{ab} \cdot \mathbf{r}_{ab}}{|\mathbf{r}_{ab}|^2} \right) \quad (2.60)$$

given velocity vectors, $\mathbf{v}_{ab} = (\mathbf{v}_a - \mathbf{v}_b)$ and position $\mathbf{r}_{ab} = (\mathbf{r}_a - \mathbf{r}_b)$, and density and speed of sound are averaged $c_{ab} = \frac{1}{2}(c_a + c_b)$ and $\rho_{ab} = \frac{1}{2}(\rho_a + \rho_b)$ between the a and b particles. This is a standard hydrodynamic viscosity term. The parameter α can be tuned to give a stronger response (Monaghan, 1999). Originally developed and refined for Raman shock tube problems, often misunderstood to reduce shocks it's actually designed to smooth out shock fronts so that they can be detected by the smoothing kernel.

Together, the SPH formulation for the modeling of a linear elastic solid is given by the continuity equation (2.21), the material constitutive law (2.45) and the acceleration equation (2.59). The implementation of these equations into a meshfree simulation is considered in the next chapter.

SPH with Elasticity

3

3.1 Introduction

In order to establish a firm basis for using SPH in solid mechanics, this chapter investigates a series of benchmark simulations in order to explore the functionality of the model in key areas. It is important to appreciate that SPH is designed to be a dynamic modelling technique and results are just a snapshot, a series of a quasi-static frames. This makes the sampling rate and sensible averaging techniques important tools which must be used to obtain results comparable to other models and analytical solutions. However, initially the model is benchmarked in section 3.2 against known equilibrium solutions in the quasi-static limit. In this case the accuracy of the two-dimensional stress field about a circular hole in a finite plate under tensile loading is investigated.

One such averaging technique which is often imbedded into the SPH code base is the extended SPH (XSPH) velocity smoothing function, introduced by one of the creators of the SPH method (see Monaghan, 1999 for details). This method attempts to improve the velocity field approximation by generating a group velocity from surrounding particles; its effectiveness is explored in Sections 3.3. One of the problems XSPH is specifically designed to help with concerns the interaction of separate bodies. By preventing large scale particle penetrations between impacting bodies, materials remain separate rather than strongly bonding together. This type of impact is explored in this section.

The conservation properties of linear and angular momentum are also investigated sections 3.3.2 and 3.3.3 via the interaction between two solid elastic balls or cylinders. Larger elastic deformations are considered in section 3.4 to show how the issue known as the tensile instability occurs and how this problem can be corrected.

3.2. Quasi-static analysis of stress in a plate containing a circular hole

The stress in an infinite plate with a circular hole under uniaxial loading predicts that the stress should be three times greater at the edge of a circular hole than that remote from the hole. The equations of elasticity outlined in Chapter 2 have been implemented in to a 2D SPH code. Using approximately 2400 particles and setup as in Fig. 3.1, using size of plate $Y=X=50$ particles and the radius of hole $R=10$ particle spacings. The top and bottom displacements of the plate were controlled to apply a tensile strain. The stress σ_y is shown in Fig. 3.2 after sufficient time for the stress field converge to a stable steady state (red is a high tensile stress and green is the

applied stress). Elasticity theory predicts that the stress profile $\sigma_y(x,0)$ along a horizontal cross-section through the centre of the hole is given by Ashby & Jones (1992)

$$\sigma_y(x,0) = \frac{\sigma_\infty}{2} \left(2 + \left(\frac{R}{x} \right)^2 + 3 \left(\frac{R}{x} \right)^4 \right) \quad (3.1)$$

where R is the radius of the hole and σ_∞ is the stress far from the hole, for an infinite plate. The plot in Fig. 3.3 gives a quantitative comparison between the stresses obtained from the SPH code and the theoretical prediction in equation (3.1).

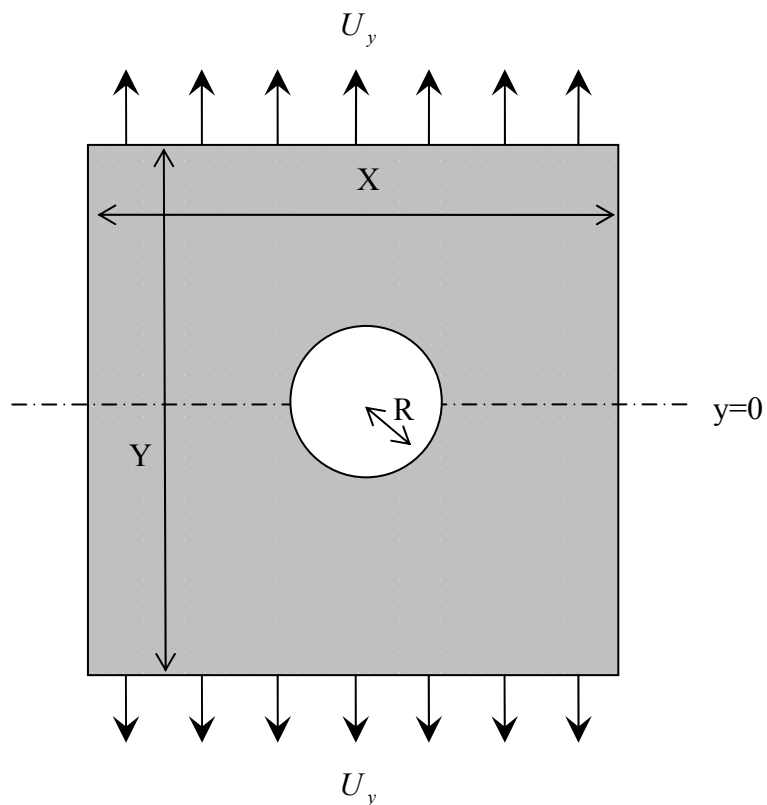


Fig.3.1. Schematic of finite plate dimensions $X = Y$, with circular hole, radius R, at its centre. Subject to uni-axial loading of F_y on the upper and lower surface. With $X \gg R$ the model is similar to that of on infinite plate.

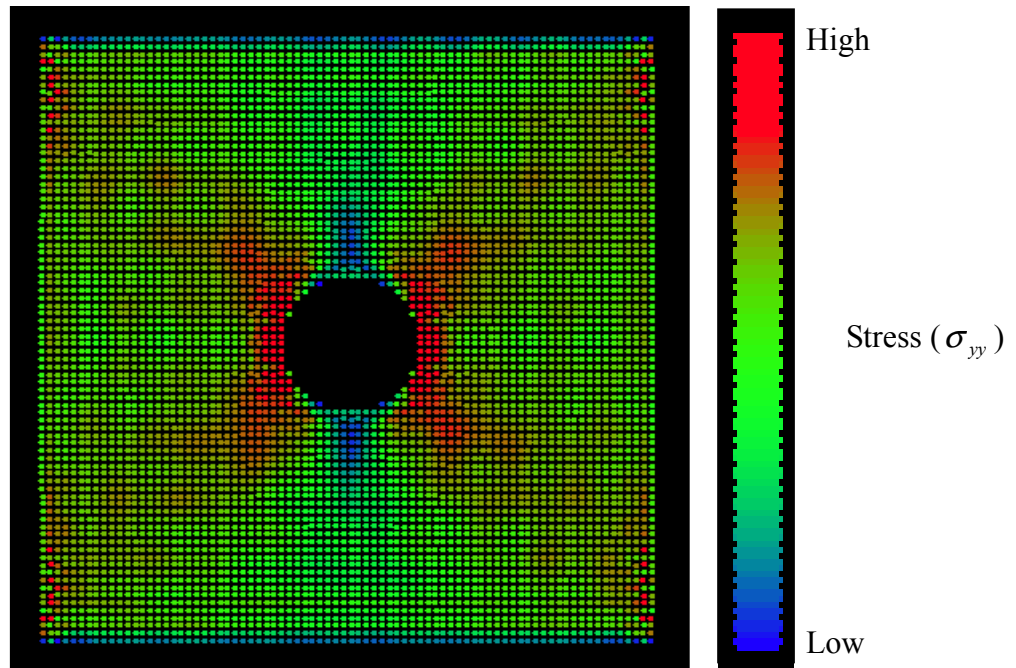


Fig.3.2. Converged stress field σ_{yy} where red is a high tensile stress and green represents the applied stress.

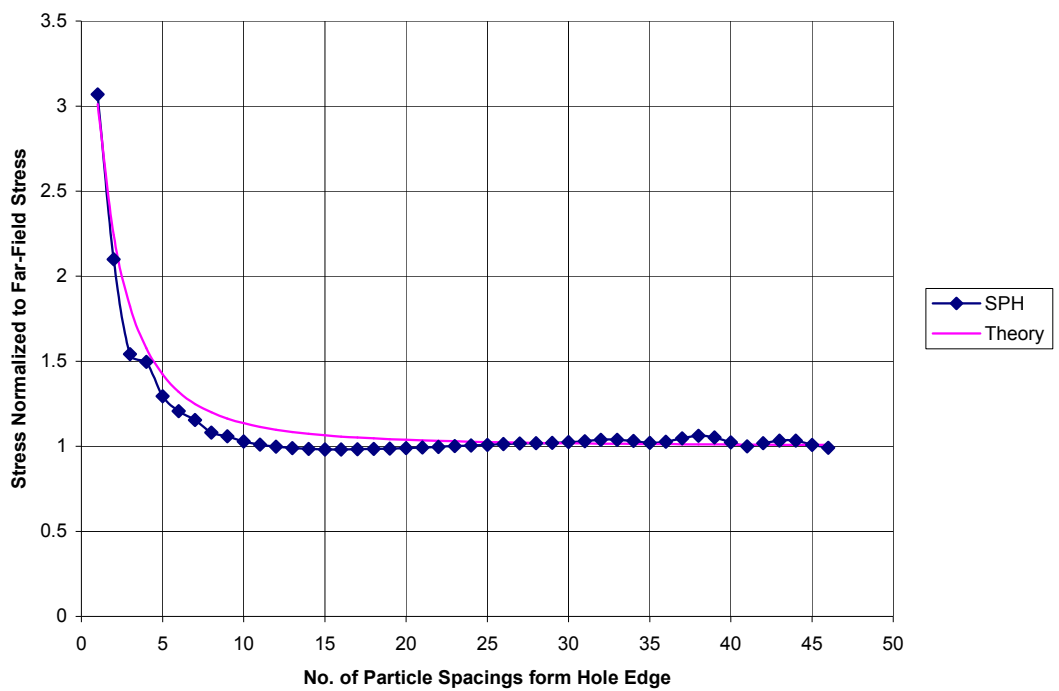


Fig.3.3. Cross section of plate with a circular hole, showing SPH particle stress and the theoretical prediction of $\sigma_y(x,0)$ from (3.1)

It is worth noting that this simulation is dynamic and is finite rather than infinite. Therefore the proximity of the boundary is not quite far enough away from the hole not to have some influence on the stress profile. Also particle stresses have been averaged over the last 10 iterations, and it is necessary to wait until shock waves have dissipated. High stresses can be seen in the four corners due to the nature of the constraints at the boundary.

3.3. Elastic Collisions and XSPH

An early addition to the SPH technique the velocity update step can be replaced with a more stable XSPH alternative which is more suited to problems involving solid body interactions (Monaghan, 1999). It essentially averages the velocity of surrounding particles and uses this group velocity to maintain stability,

$$\hat{\mathbf{v}}_a = \mathbf{v}_a + \tilde{\mathcal{E}} \sum_b \frac{m_b}{\rho_{ab}} (\mathbf{v}_b - \mathbf{v}_a) W_{ab} \quad (3.2)$$

where the density average, $\rho_{ab} = \frac{1}{2}(\rho_a + \rho_b)$, and $\tilde{\mathcal{E}}$ is a dimensionless constant, Monaghan (1999) suggests $\tilde{\mathcal{E}} = 0.5$, which represents the magnitude of the influence that neighbouring b particles have over the group velocity.

3.3.1. Interactions with a solid wall

SPH is more often used to study impact dynamics (Mandell, Wingate & Schwalbe, 1996) as large changes in geometry and highly dynamic events are generally handled extremely well. The most basic model of a ball bouncing off a rigid surface shows

how SPH compares with alternative models.

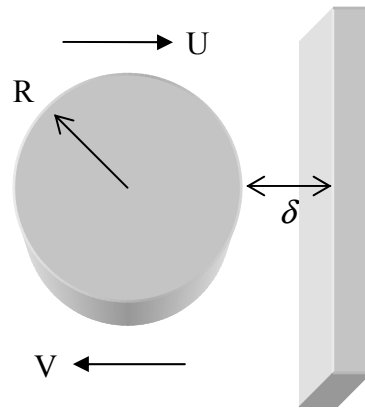


Fig.3.4. Schematic of ball, radius R , bouncing from a fixed wall, at distance δ , with U representing the initial and V the final velocities.

Simulation of the elastic collision in Fig.3.4 are plotted in Fig.3.5. with XSPH on ($\tilde{\epsilon} = 0.5$) and XSPH off (effectively $\tilde{\epsilon} = 0.0$).

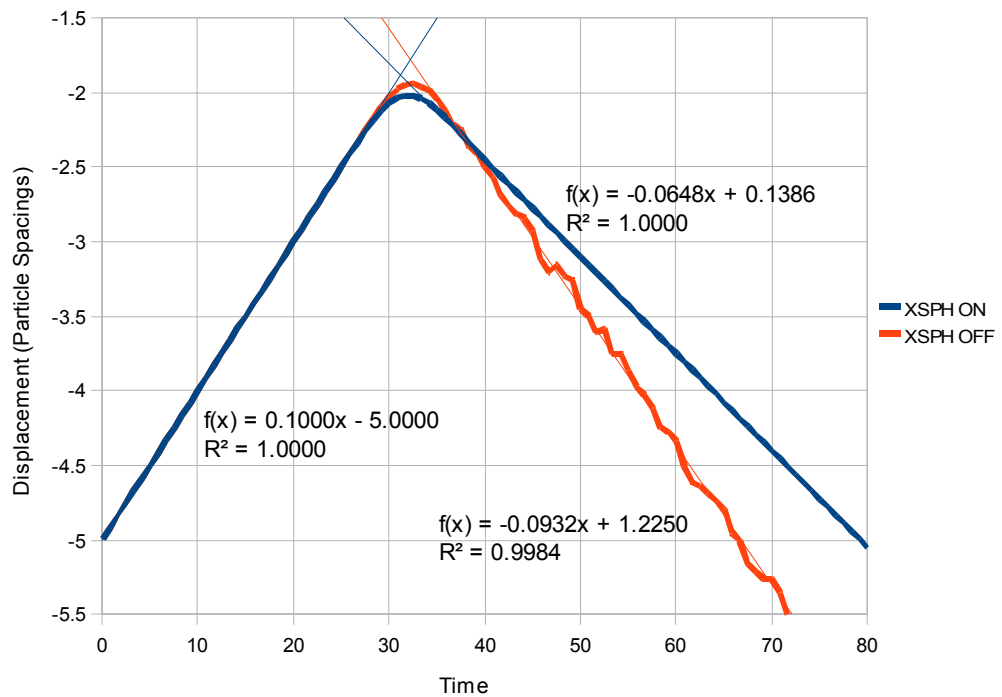


Fig.3.5. Pre and post impact displacements for rigid wall collision, with and without XSPH velocity smoothing

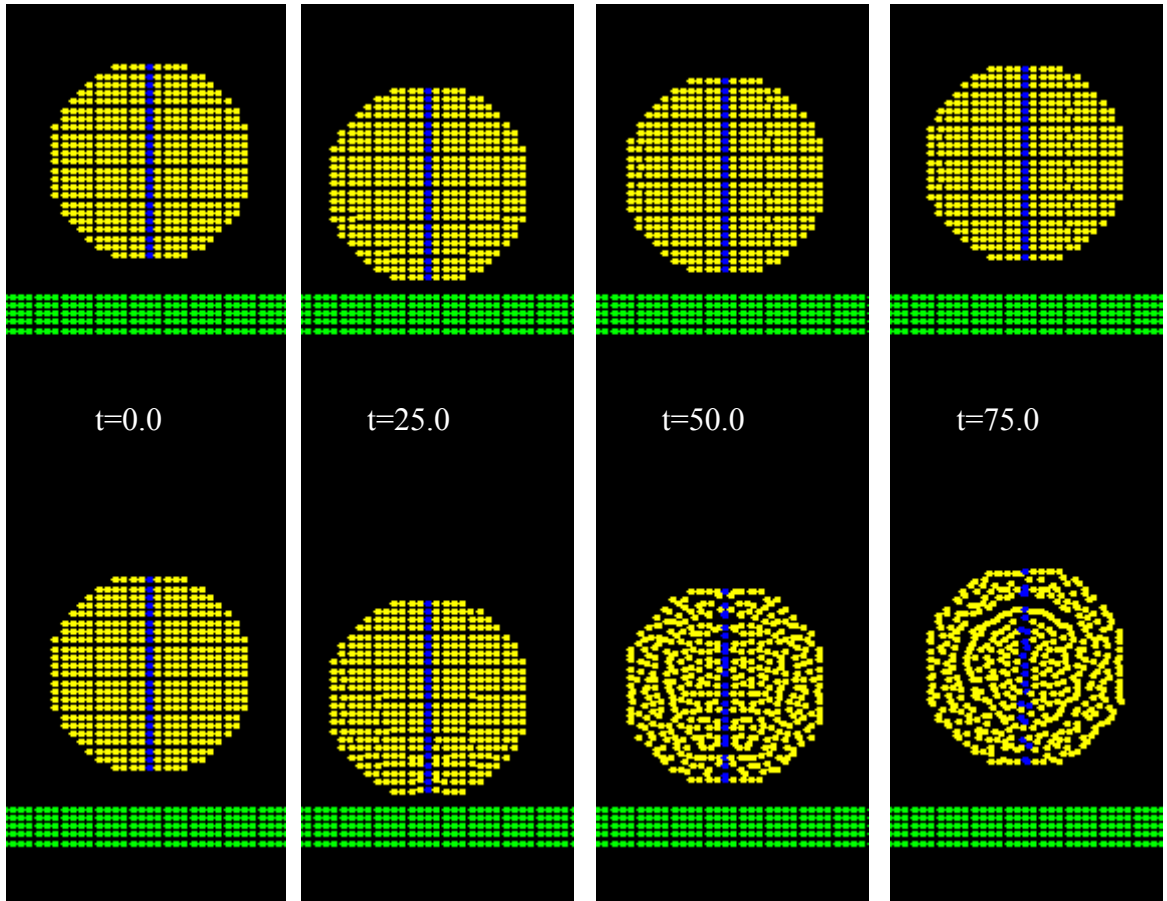


Fig.3.6. Snapshots of SPH particle map during elastic collision with a rigid wall.

Velocity smoothing XSPH is absent in the lower set of images.

As Fig. 3.6 clearly shows on the upper simulations the presence of XSPH clearly offers less disorder to the particle map post collision. The cost of the extra stability of XSPH is that, especially when interacting with fixed boundary conditions, a loss of energy conservation can occur due to excess averaging. Tweaking the XSPH parameter allows the combination of stability and conservation properties, for this simulation a value of $\tilde{\epsilon} = 0.1$ appears to offer the best compromise.

3.3.2. Conservation of Linear Momentum

The conservation of linear momentum should occur naturally due to the equal and opposite interaction between a and b particles. This formulation naturally occurs when deriving the elastic interactions from the Euler-Lagrange method outlined in Section 2.5.

To test whether this remains true under real simulation conditions, two cylinders are set to collide using 2D SPH code representing each cylinder as a circle with initial conditions described in Fig.3.7.

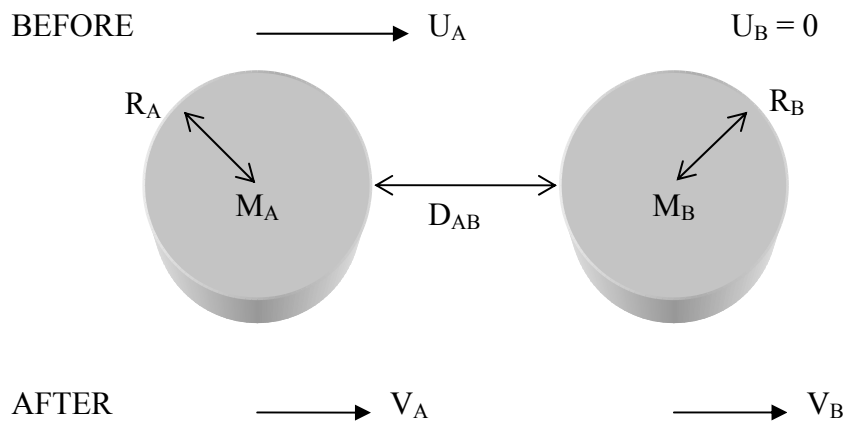


Fig.3.7. Colliding cylinders A and B where M_A and M_B represents the total mass of particles in cylinders A and B, each with radius R , initial prescribed velocities U and post impact velocities V and D_{AB} =Shortest distance the between cylinder A and B.

The first set of simulations varies the mass of SPH particles in the circle B, so that

the ratio $\frac{M_A}{M_B} = \left[\frac{10}{1}, \frac{10}{2}, \frac{10}{3}, \frac{10}{4}, \frac{10}{5}, \frac{10}{6} \right]$, for simulations [1,2,3,4,5,6]. Other

parameters are $R_A = R_B = 12$, $U_A = 1\%$ the speed of sound, c and $U_B = 0.0$

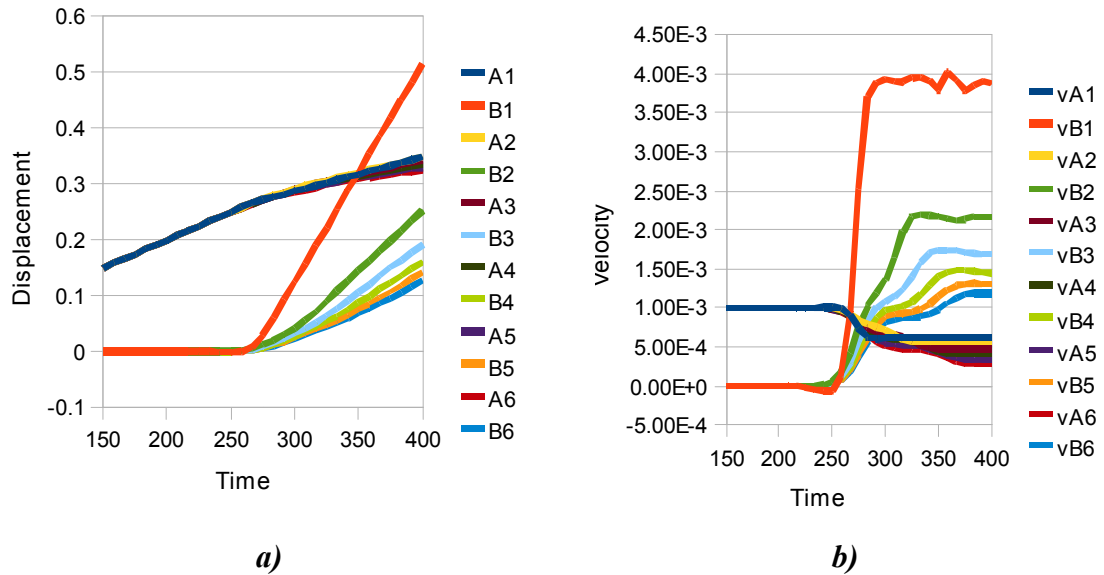


Fig.3.8.a) The displacement (measured in particle spacings) and
 b) velocity (in spacings/timestep) of two colliding elastic bodies A and B ,
 through a set of six simulations of varying mass ratio but
 constant incident velocity of $U_A = 0.01c$

An average sampling of the velocity profile in Fig. 3.8b is necessary as shown by the velocity of the particle on the contact surface of cylinder A and B for all simulations. Even with XSPH velocity smoothing some of the energy of the impact is converted into internal energy of the cylinder, as mentioned in the derivation in Section 2.5., causing particle vibrations which at lower velocities can be a sizable percentage of the group velocity.

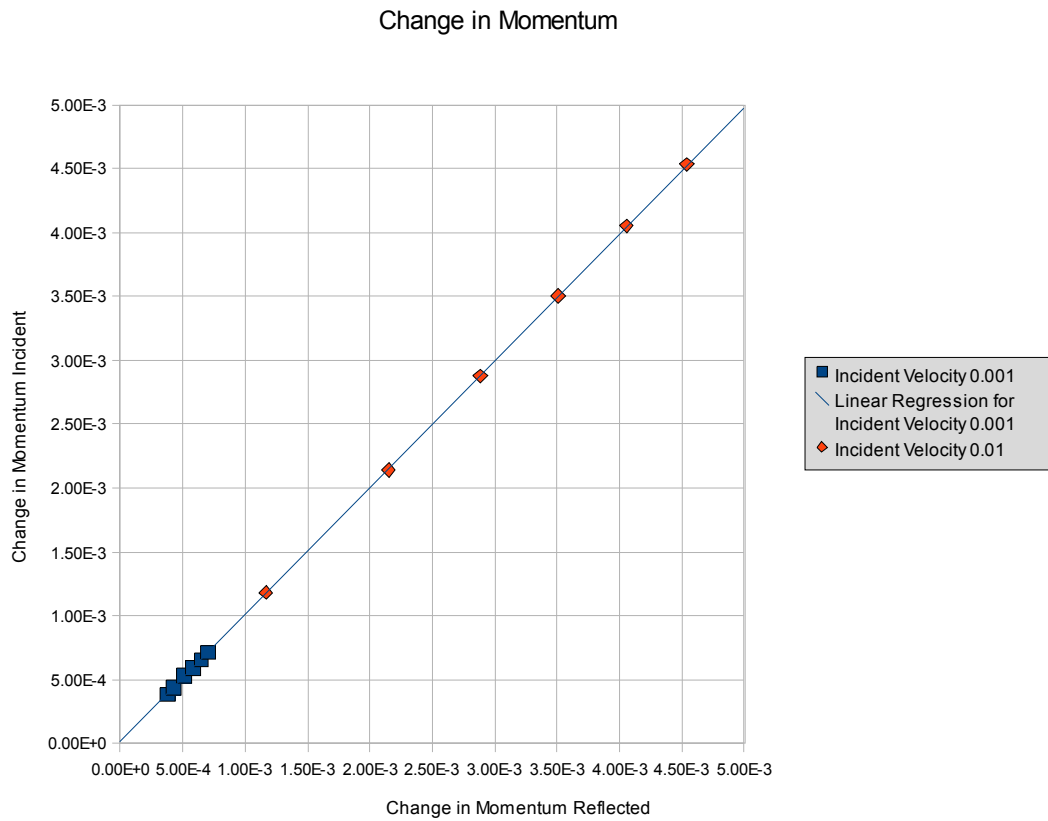


Fig.3.9.The total incident and reflected momentum for elastic collisions at speeds of 1% and 0.1% the speed of sound.

A comparison with the lower initial velocities of $U_A=0.001c$ is shown in Fig 3.9, the close match with expectations shows that in the over a range of relatively high speed collisions, SPH conserves linear momentum.

With velocities approaching $U_A=0.0001c$, and $M_A/M_B=10$ a different picture begins to occur. Fig. 3.10 shows how under these conditions the internal energy is reaching the same magnitude as the rebound velocity; resulting in a break down of cohesion between the particles. As the bond between the particles in cylinder A are just as strong as the bonds between the particles interactions from cylinder A to cylinder B , the kernel has no preferential treatment and the cylinders are ripped apart. This ‘pull back’ effect is investigated later in Section 5.2.1 and resolved in Chapter 4.

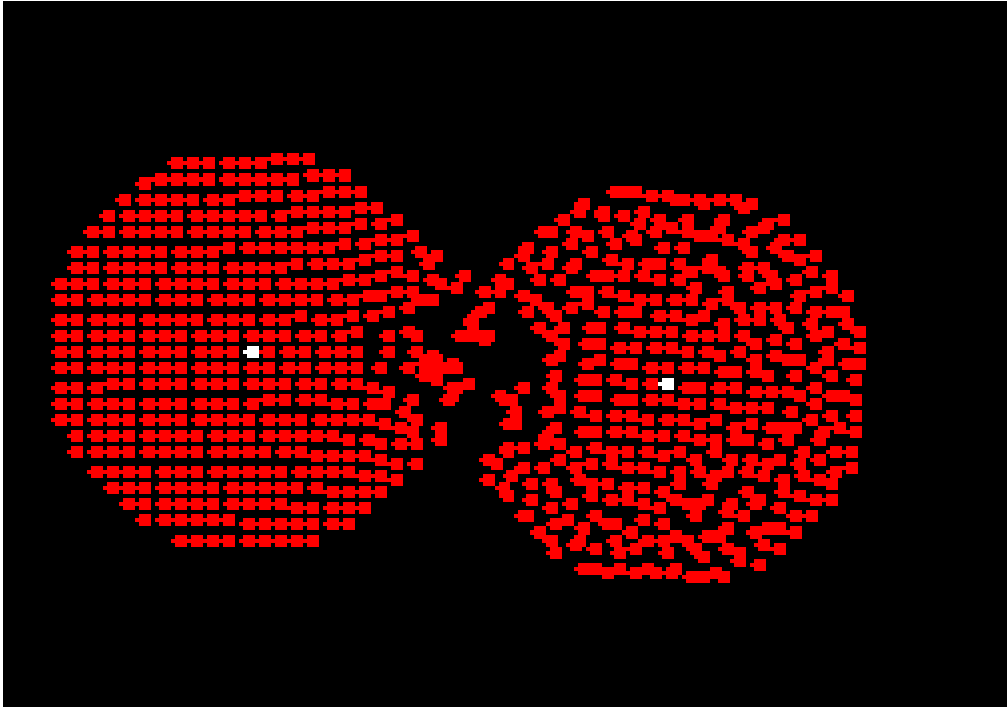


Fig.3.10. Break down of particle map in “low” velocity impact
of 0.01% the speed of sound

3.4. Conservation of Angular Momentum

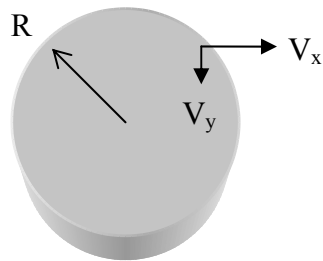


Fig.3.11. Schematic of a rotating cylinder, radius R ,
and velocity components (V_x, V_y)

Using the standard 2D SPH code with the cylinder represented by 437 particles arranged in a circle using Cartesian coordinates. Every particle is given an initial velocity depending on its (x,y) coordinate, to initiate circle motion,

$$\mathbf{v}_a = \frac{1}{10}(-y_a, x_a) \quad (3.3)$$

With the XSPH velocity stabilization routine detailed in section 3.3 the cylinder rapidly comes to a halt, see fig.3.12. The spatial averaging reduces any velocity differences along any radius, required for circular motion, to zero. In this case the group velocity cannot describe circular motion and hence has no angular momentum conservation properties.

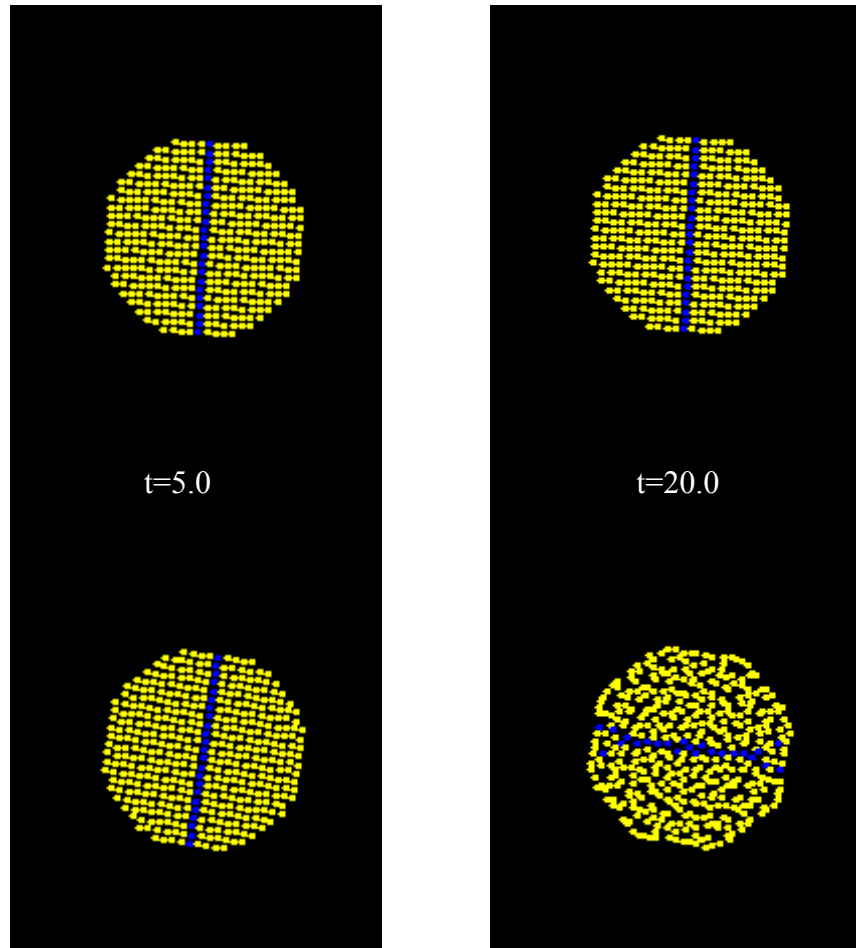


Fig.3.12. Particle map of rotating cylinder with XSPH on (top) and without XSPH (bottom)

Removing the XSPH condition results in some improved circular motion. However, as Fig. 3.13 shows, dissipation soon brings the rotation to a stop before 270 degrees has been completed and considerable particle rearrangement has occurred.

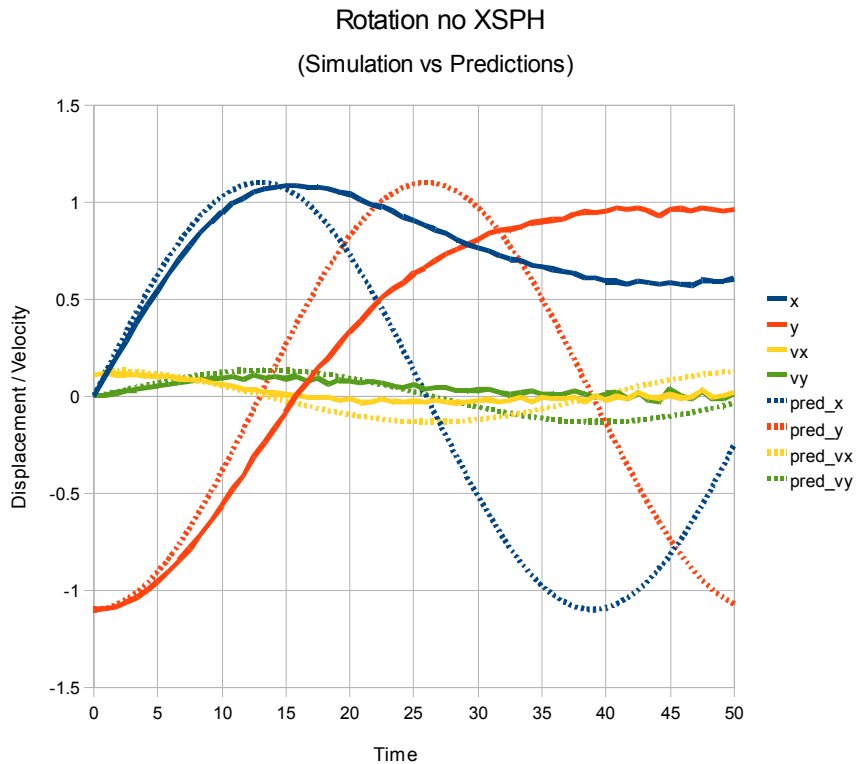


Fig.3.13. Displacement and velocity profiles of a particle situated on the edge of the rotating body and predicted quantities

The first 150 degrees of rotation in this simulation (time<45) can be matched by a velocity dissipation term of the form,

$$\dot{\theta} = (v - \text{dissipation}) r dt \quad (3.4)$$

where $\text{dissipation} = 0.0025t$

As Fig.3.14 shows the match to (3.4), after 150 degrees further dissipation and particle re-arrangement makes further modeling impractical.

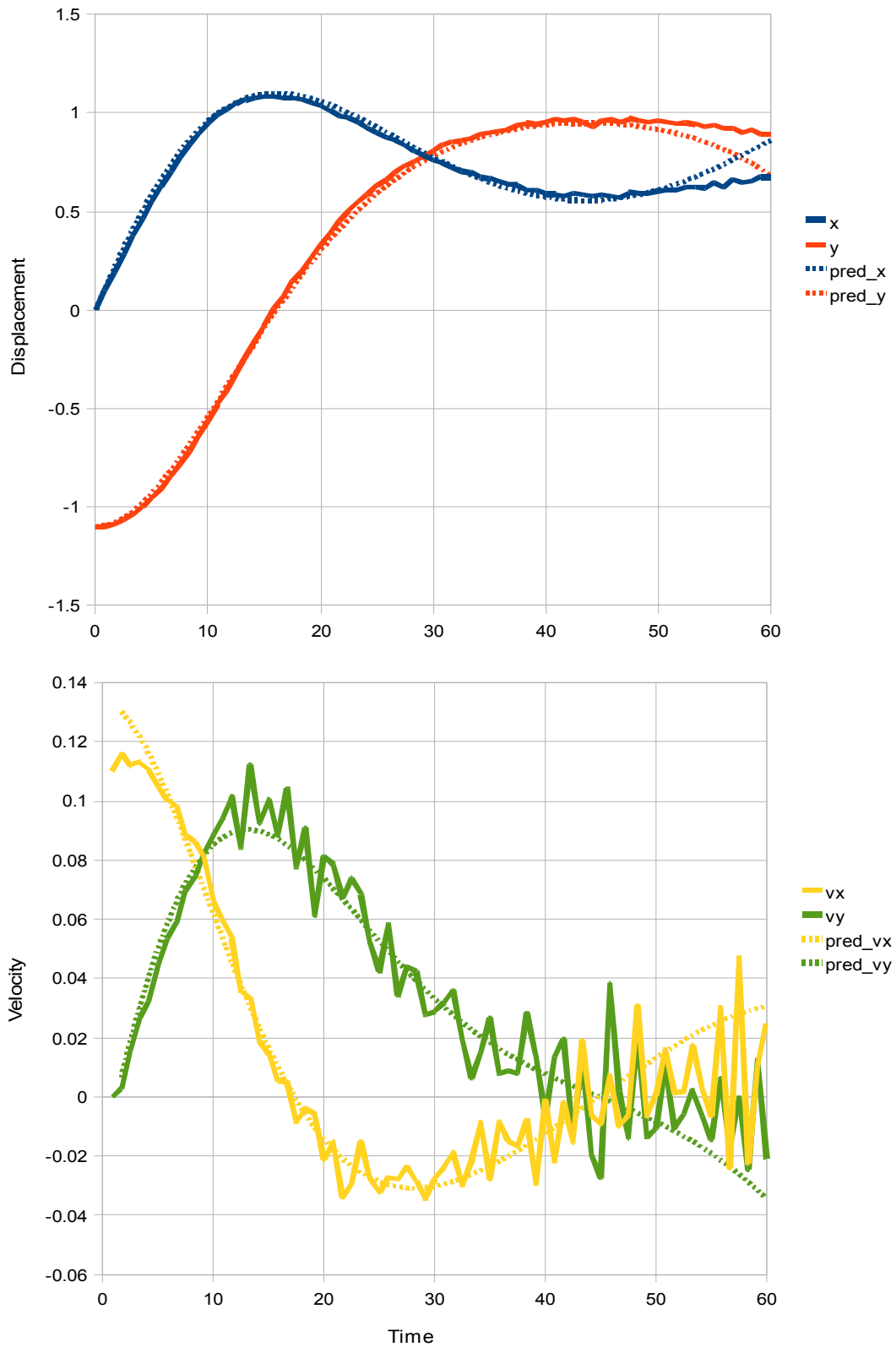


Fig.3.14. Displacements (top) and velocity (bottom) profiles for a damped rotator

3.5. Colliding Rubber Rings and the Tensile Instability Correction

The simulation of perfectly elastic rubber in Monaghan (2001) was used to demonstrate the issue of tensile instabilities in standard SPH codes. Rings of with an external R_o and internal R_i radius are set to collide as in Fig.3.15.

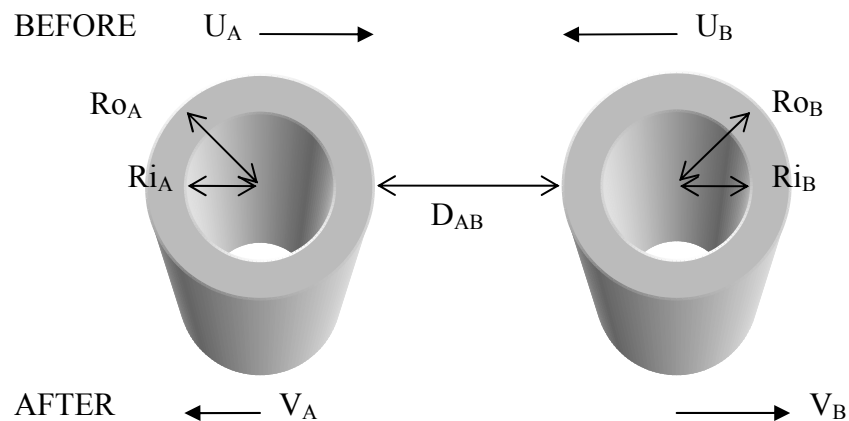


Fig.3.15. The Collision of two thin walled rubber rings.

With the outer radius R_o of 35 and an infra radius R_i 30 particles

The results in fig.3.16 show that SPH particles in tension (or under negative pressure gradient in hydrodynamics) often clump together in unphysical ways. The effect is especially apparent in Solid Materials due to the regular structure of the particle map, although the problem still exists in fluid flows it is harder to spot. Methods for removing/reducing this instability have been developed that change the kernel function, however this impacts on the performance and stability in other areas.

The stress-viscosity terms previously described in section 2.5 by the acceleration equation

$$\left(\frac{\sigma_a^{ij}}{\rho_a^2} + \frac{\sigma_b^{ij}}{\rho_b^2} + \Pi_{ab} \delta^{ij} \right) \quad (3.5)$$

With the addition of a repulsive force this now becomes,

$$\left(\frac{\sigma_a^{ij}}{\rho_a^2} + \frac{\sigma_b^{ij}}{\rho_b^2} + \Pi_{ab} \delta^{ij} + R_{ab}^{ij} f^n \right) \quad (3.6)$$

where $R_{ab}^{ij} = R_a^{ij} + R_b^{ij}$, is only applied for negative (tensile) strains and

$$f = \frac{W(r_{ab})}{W_0} \quad (3.7)$$

modifies the kernel distance between particles and normalize by the kernel over an initial particle spacing. Where n gives a high order (typically 6) giving an extremely strong short ranged force which falls off rapidly.

The result is an extra force that applies only to close particles and gives negligible impact on others. The effect of this tensile instability correction on the rubber rings simulation is shown in Fig.3.16. The unphysical clumping and consequential crack formation is almost entirely removed. Later works have included a modification that adds to the forces only to principle stresses and a complete Lagrangian formulation to further attempt to completely eradicate this instability, see (Liu & Liu, 2010)

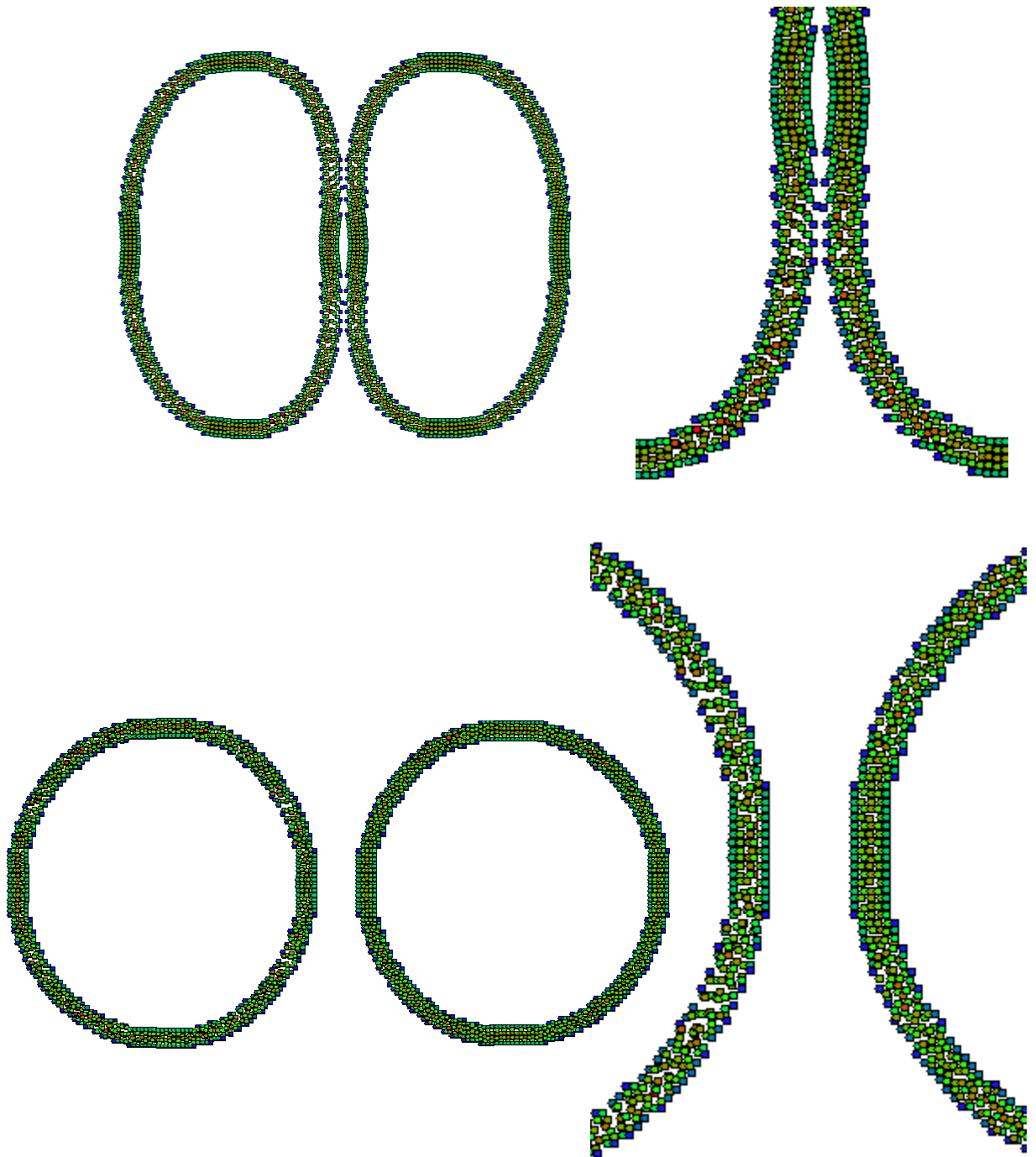


Fig.3.16. Particle clumping on the left-most ring is almost entirely removed by the tensile instability correction on the right-hand ring. The gap opened up during contact (top) are permanent and remain post contact (bottom)

3.6. Summary

The adaptation of SPH to the simulation of elastic dynamics demonstrates some unique obstacles that need to be overcome. Modifications have been presented that minimize or allow best practise when using SPH with solid mechanics applications. Overall simulations involving rotations and conservation of angular momentum are not handled well by standard SPH methods, and are best described as damped by dissipative terms which increase the entropy of the system as a whole.

It is worthy of note that interactions between separate bodies can be modelled for highly dynamic events. But lower velocity impacts result in the considerable merging as the kernel acts attract particles to one another. The effect can be seen in low velocity impacts, as in Fig.3.10 or during indentation tests as simulated in Chapter 5. This process is predominantly based upon kernel geometry rather than the physical properties of the material. It is therefore desirable to remove these phenomena and apply a kernel independent method of generating contacts. The Chapter 4 deals with the development of such a method.

Contact Mechanics

4

4.1. Impact Dynamics

The principles of Smooth Particle Hydrodynamics are ideally suited to situations where deformable structures impact one another. It has been used in military applications to test the deformation and penetrative force of ammunitions through various armours (Mandell, Wingate & Schwalbe, 1996). In these simulations the impact usually causes massive shape changes to both the armour and the ammunition round. Pieces of ammo and/or armour can detach from the main body and cause collateral damage to their surroundings; in fact this sort of behaviour is advantageous as it maximizes the damage caused.

This is an ideal problem for mesh-free simulations as they can model the large deformations and break-up of solid bodies into many smaller fragments, tracking the trajectories of many fragments and giving an idea of the extent of damage. As such a

fair amount of work has been conducted into high velocity impacts, not only in military applications but also with problems such as meteor strikes and other astrophysical phenomena. SPH requires some modifications to handle high velocity impact correctly, as demonstrated in Chen, Pan and Wu (1997) where the impact of hyper velocity elastic rings is considered.

Problems of colliding bodies involving less kinetic energy may have less of an impact visually, but are of huge importance in a wide range of engineering applications. The smaller deformations involved have meant that rival grid based methods have been used to simulate such interactions and hence less research has gone into low velocity impacts using SPH. This can be partially attributed to the difficulties defining a rigid edge to the ill-defined surface of an SPH particle. But also the approximations of properties along this surface lead to inaccuracies that are masked in higher impact velocities, and subsequent non-linear behaviour.

A standard benchmark to simulate these low-velocity impacts is an elastic (and plastic) ball bouncing off a rigid surface. This is something SPH simulations have struggled with for low velocity impacts (see Section 3.3.1), but can easily be reproduced using alternative techniques and analytical solutions. This gives an opportunity to benchmark improvements to the SPH method and directly compare to simple analytical and simulated results. By obtaining a method using SPH that accurately matches real world behaviour in these simple cases, more complex problems such as ball bouncing off deformable surfaces with varying elasto-plastic behaviour can be modelled with little additional effort.

4.2. The Standard SPH Approach

As already demonstrated in the standard SPH method can deal with elastic behaviour and the conservation of linear momentum. However, issues still exist due to the way SPH particles interact with one another through the Kernel, namely

- i) The range of the SPH kernel, usually defined as $h = 1.5$ (or three particle spacings) in a standard gaussian kernel (see Section 2.1), naturally generates a non-physical edge to a body, this 'fuzzy surface' problem can be made considerably worse if adaptive h kernels are not sensibly employed.

- ii) The location of the surface to a body is not only controlled by the kernel, rather than user defined values, but the surface is not well defined as it slowly decreases from the particle closest to the edge out to the maximum kernel distance. The rate of decay depends on the shape of the kernel (see Section 2.2.1). One method for attempting to improve the definition of a boundary shapes the kernel depending on the local geometry (Dilts, 1999). However the constant recalculation of the kernel is computationally intensive, only yields marginally improved results in real world tests and does not solve other issues associated with low velocity impacts so is not pursued any further here.

- iii) Inaccuracies in the properties of discrete SPH particles that lay close to the edge create further issues. Interpolating values is not as accurate as

by its very nature a surface has fewer particles with which to compare values to. As SPH particles interact through the stress field, and as stated above the stress state on fuzzy surface is poorly defined, non-physical interactions can occur, e.g. the “pullback” effect Sections 4.3.5 and 5.2.1.

- iv) In its standard form SPH particles have no differentiation from each other, and so particles once in contact will bind with one another and require energy to separate, creating a ‘stickiness’ between all particles inside the kernel range. This adhesive nature can only be overcome by separating the particles to outside the kernel range so they no longer interact. This behaviour leads to kernel controlled damage, as seen in Section 5.3.1, rather than a physical material response.
- v) SPH is a dynamic modelling technique, simulations can produce quasi-static responses but shock waves and dynamic effects will sometimes result in differences to static body predictions. The artificial viscosity parameter (Section 2.5) goes some way to provide a consistent approach to resolving shocks, but for static body problems SPH suffers from its dynamic heritage.

Even taking into account these factors SPH has been shown in Section 3.3 to be able to conserve linear momentum in the ball bouncing model with some accuracy. However, it is apparent at lower velocities the ball the simulations become less accurate (see Fig.3.10) and the intertwining of particles and “pull-back” effect is something that any contact algorithm must overcome.

4.3. Penetration Algorithm

It is apparent that a better method is required to allow surfaces to interact in SPH simulations without the problems associated with the kernel and issues highlighted so far. The first step is to add a mechanism to separate particles in one body from another to prevent the standard SPH interaction when two dissimilar bodies interact through the kernel. This can be achieved by giving each particle an additional property, called 'particle type', which identifies body it belongs to.

Early proof of concept simulations by this author used particle type to generate alternative interactions between different particle types by altering the strength of interaction. A hard precipitate, particle type-*b*, could be embedded in a substrate of particle type-*a*. Interaction between particle type-*a* and a similar type-*a* particle (an *a-a* interaction) had a certain strength, while *b-b* interactions were stronger. Finally *a-b* interactions were the weakest, effectively giving a weak interface between different particle types. Although these early simulation showed it was possible to deflect large cracks (see section 5.3.1, better defined as ripping particles far enough apart to prevent further interaction) the kernel was still the controlling factor with all the pros and cons associated.

It is equally plausible to turn off the kernel interaction between different particle types completely. So that only similar type particles interact, and non-similar will pass completely through each other. This technique is useful for running multiple simulations in the same space and time, but without worrying about interactions between different simulations. For example multiple initial velocities of ball

impacting against a rigid surface can all be run in a single simulation, saving the need to batch and run a large number of smaller simulations, by giving each ball a separate type and skipping any interactions between dissimilar type particles.

With the kernel switched off for dissimilar particle types it is now possible to define a new method for interacting particles without the inherent problems of the kernel size and interactions across surfaces becoming an issue. However the versatility of the kernel interactions can be maintained to allow objects to deform freely under stresses without the need to recompute geometries.

4.3.1. Identifying Surfaces

As already discussed SPH particles have a diffuse or fuzzy surface (akin to fuzzy logic neither on nor off but somewhere in between). Relying purely on overlapping kernels to produce a contact algorithm results in very soft contacts over a kernel distance. Fig.4.1 shows how the magnitude of a series of overlapping kernels declines as it goes beyond the edge of a sample.

Exactly where on such a slope a surface is defined will be subjective. But techniques such as those suggested by Rodriguez-Paz and Bonet (2003) have adapted the kernel to produce a better defined edge, but at the expense of computational complexity, akin to alternative re-meshing approaches with deformable geometries.

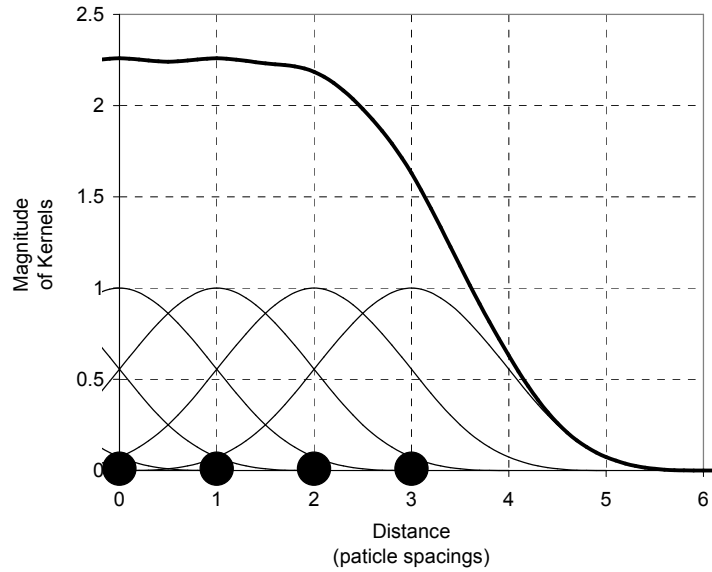


Fig.4.1. Density evaluation from overlapping kernels
leaving a uncertain or ‘fuzzy’ surface

A far less complex approach is to define a surface as a circle of arbitrary radius from each particle, now if two such interaction zones overlap, particles can be said to be in contact. While this approach, commonly known as particle to particle contact, is easily computed, and certainly fits well with SPH methodology, it doesn't lead to a particularly uniform surface, giving rise to uncertainty as to when particles will cross depending on local geometries, as demonstrated in Fig.4.2

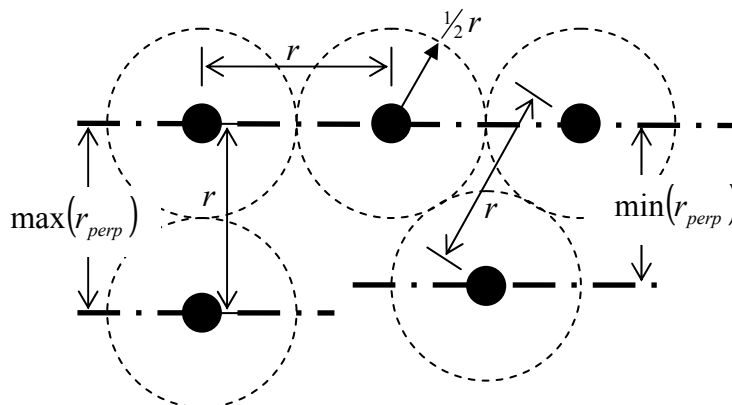


Fig.4.2. Two different geometry configurations with different surface evaluations

An alternative is to implement a particle to surface contact, allowing regular geometries to interact when they reach a set perpendicular distance no matter how the two particle geometries are transversely displaced. The interaction zone is now a square of user-defined length (twice a single particle spacing is used here), and when a particle of different type enters this zone they can be considered to be in contact.

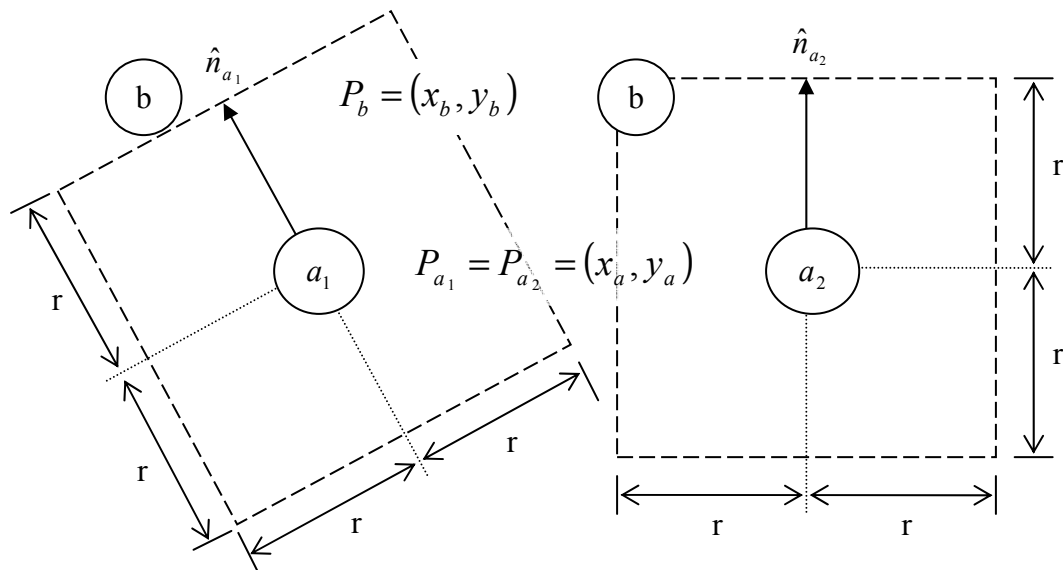


Fig.4.3. Two examples of particle in a square configurations differing only by direction of normal vector, (left) no contact and (right) contact.

To be able to track any geometry changes the square interaction zone must rotate with the surface, and in order to achieve this, the normal vector of each particle along a surface must be defined. This in itself is no trivial matter when dealing with deformable surfaces, and is dealt with in the following section.

A procedure to define which particles lay on the surface of a body will reduce computational time spent on generating normals. However, this can not be achieved by simply defining surface particles during the creation of geometries, as surfaces may be generated or removed during deformations. Instead the following procedure

is recommended; during nearest neighbour analysis a track of how many particles are within a fixed kernel range is stored. A particle is defined as laying on a surface when the number of particles of the same type falls below a set percentage (100% defined as a fully surrounded inertia particle), see Fig.4.4. Note this method can be used to define corner particles if it is necessary for these to be treated differently, to standard surface particles. Particle type is an important consideration here as two bodies of different type can still have the surfaces identified, even if they begin the simulation in close proximity.

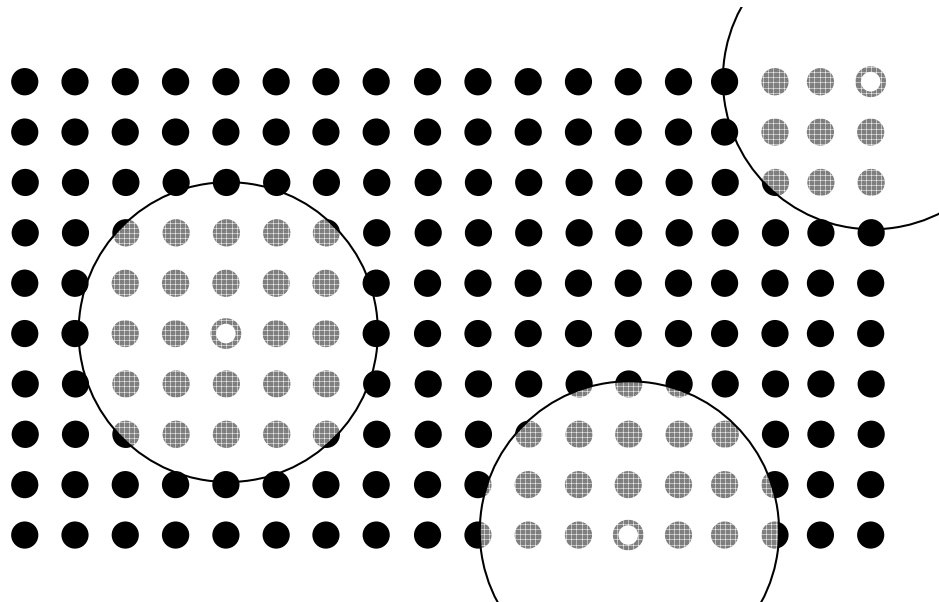


Fig.4.4. Three particle designated as (from left to right) inertia particle, surface particle and corner particle based on the number of neighbours

Due to the small size of the sample kernel and the discrete nature of the particles in this work, for 2D simulations any particle with 75% of the maximum number of neighbours or below is considered a surface (50% or below can be considered a corner)

4.3.2. Creation of Normal Vectors

During the initial creation of the particle map it is easy to define the normal vectors of a flat surface, or any regular geometric shape. It is however necessary to keep track of these normal vectors during large scale deformations that can take place in SPH simulations. It is sometimes beneficial to be able to predefine normal vectors during the initial geometry set-up. For example using standard Cartesian coordinates to define a circle out of a discrete array of points yields a jagged surface with ill defined normals. With some initial geometries the correct normals are easy to calculate, such as extending outwards from the centre of the circle.

It was first hoped that each normal could be rotated from a set of (initially perfectly) defined normals as the simulation developed. However SPH particles are free to rotate about their own axis under the influence of stresses, as in any Lagrange based scheme, so it is not easy to correctly track the rate of change of the normal vectors. It is therefore apparent that a different technique is required to generate and maintain the normal vectors from an initial configuration and as surfaces deform.

Knowledge of the location of all surface particles, can be used to determine the normal vector for every surface to surface particle pairing inside a set range. (The kernel range is an obvious choice as the nearest neighbour analysis has already been performed.) The average of all these surface pairings should give a reasonable estimate of the surface normal. However, the relatively small sample set will lead to inaccuracies, especially when small scale deformations take place. Also the sign of the vectors magnitude is not defined, and has to be calculated by determining which

end of the vector is outward pointing (i.e. which end is furthest away from all (not just surface) neighbouring particles).

A solution more in keeping with the SPH methodology sums the vector between all SPH particles of similar type inside the kernel range. The vectors can also be weighted by the kernel, giving more prominence to closer particles. This weighted averaging approach is similar to that used in Yang and Feng (2004), where other methods are also applied to further improve normal estimation primarily for CAD applications. The advantages to this kernel method are that it widens the sample set of data compared with an all surface approach, and also naturally determines the direction of the normal vector, \hat{n}

$$\hat{n}_a = \sum_b \frac{(x_a - x_b)}{r_{ab}} W_{ab} \quad (4.1)$$

where x_a and x_b represent the position vector of a and its neighbouring b particles at a distance r_{ab} from each other, with a standard normalized kernel of W_{ab} will produce the unit normal vector of a . Results indicate that the best method tested uses the kernel weighted averaging approach which excludes particles that also lay on the surface. This is due to the fact that these particles can have a (near) reflex angle that can skew results in favour if not cancelled out by an equally spaced particle on the opposite side.

4.3.3. Improved Surface Evaluation

With every surface particle assigned the required normal vector, any particle of a different type entering within the interaction zone can be considered in contact. The interaction zone defined as the square centred on the surface particle aligned along

the normal vector, in these simulations the half length of the side is equal to one particle spacing, see Fig.4.3. Therefore, to be in this zone (and hence considered in contact) a particle of dissimilar type must be within one particle spacing along the direction of the normal vector AND within one particle spacing to the tangential vector.

If a series of surface particles and associated interaction zones are drawn, Fig.4.5 it is possible to see a slight aberration in the surface which could yield unexpected results. In this figure it can be seen that the particle to the left and right of the corner particle will interact before the edge particles will engage. Although this an extreme example similar artefacts can appear on only slightly deformed edges.

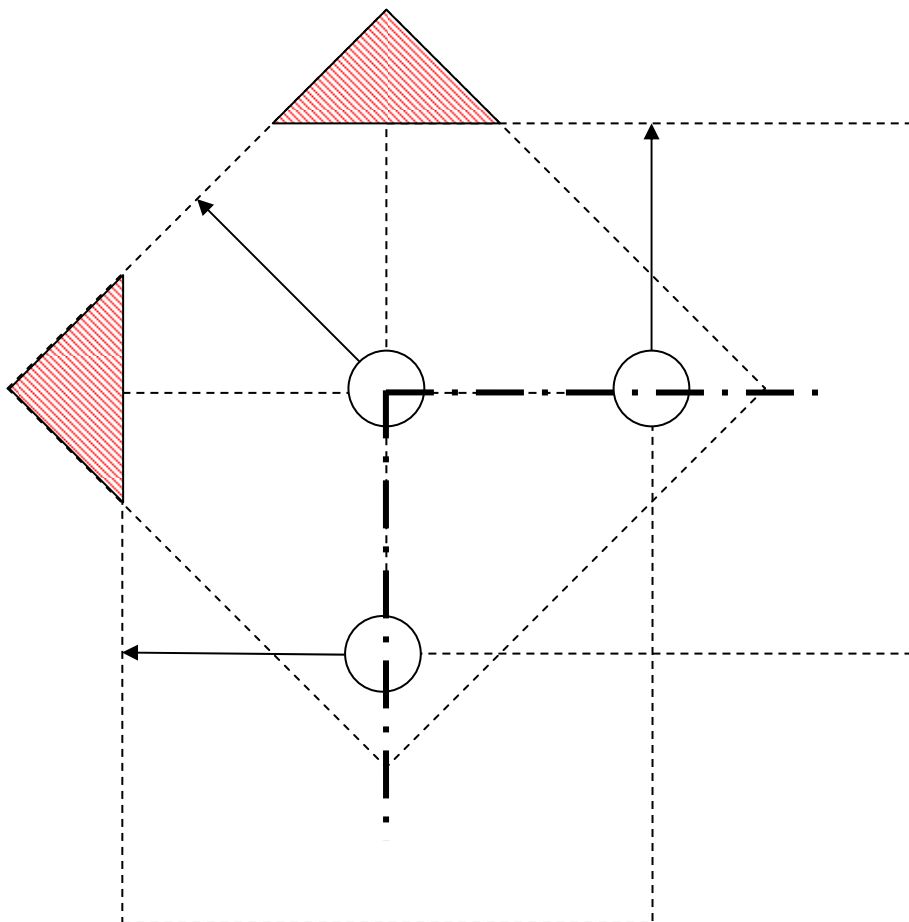


Fig.4.5. Spurious arrangement of interaction zones on corner particles

A potential solution is to assign multiple normals to the single particle. These normal vectors are shared between all neighbouring particles in kernel range. Contact is only made when inside all of the interaction zones associated with that particle. In Fig.4.5, the two red areas will no longer cause an interaction under this scheme. Occasionally the issue at corners or along irregular or jagged geometries can still lead to odd behaviour, especially when attempting sliding contacts (see Section 4.4).

4.3.4. Penalty Force

The final step in this contact algorithm is to apply a force on any particles previously identified as being in contact. This force should be directed along the surface normal vector and equal and opposite (Section 2.5) to conserve linear momentum, (Section 3.3.2)

$$F_{pen} = \begin{cases} -\left(\frac{R}{r_{perp}} + 1\right) \cdot \hat{n} & \text{when } R > r_{perp} \\ 0 & \text{when } R < r_{perp} \end{cases} \quad (4.2)$$

where R is the desired radius of impact and r_{perp} is the perpendicular distance between particles in contact. Even this simple formulation is shown to be effective, as demonstrated in the next section. For a more specialized penalty force see Seo, Min and Lee (2008)

4.3.5. Simulations

The simulations of a ball bouncing from a fixed wall is revisited here, particle maps are shown in Fig.4.6 and results are compared to the standard SPH model in Fig.4.7

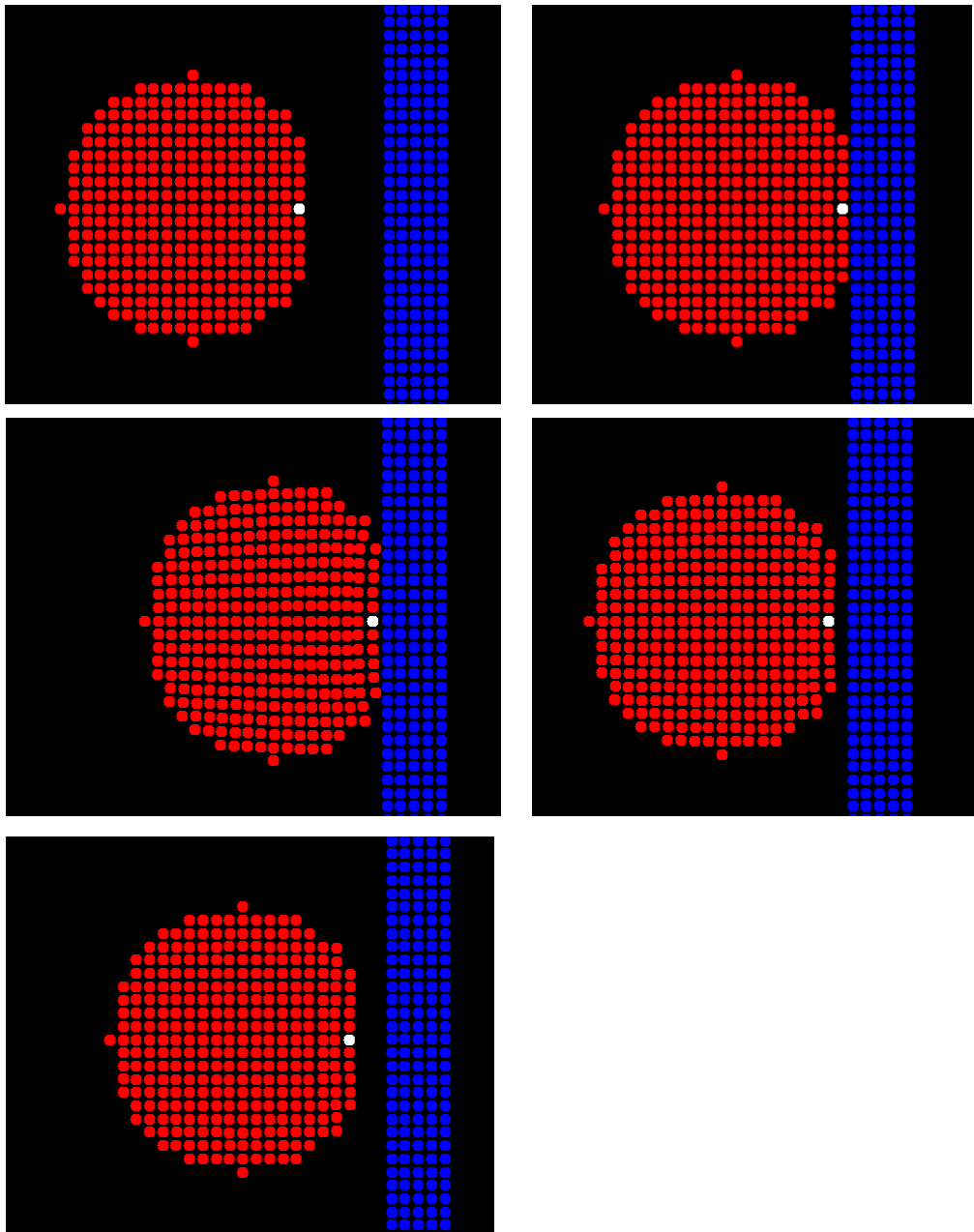


Fig.4.6. Ball bouncing from a fixed wall using the contact algorithm,
the position of highlighted particle is plotted in Fig.4.7.

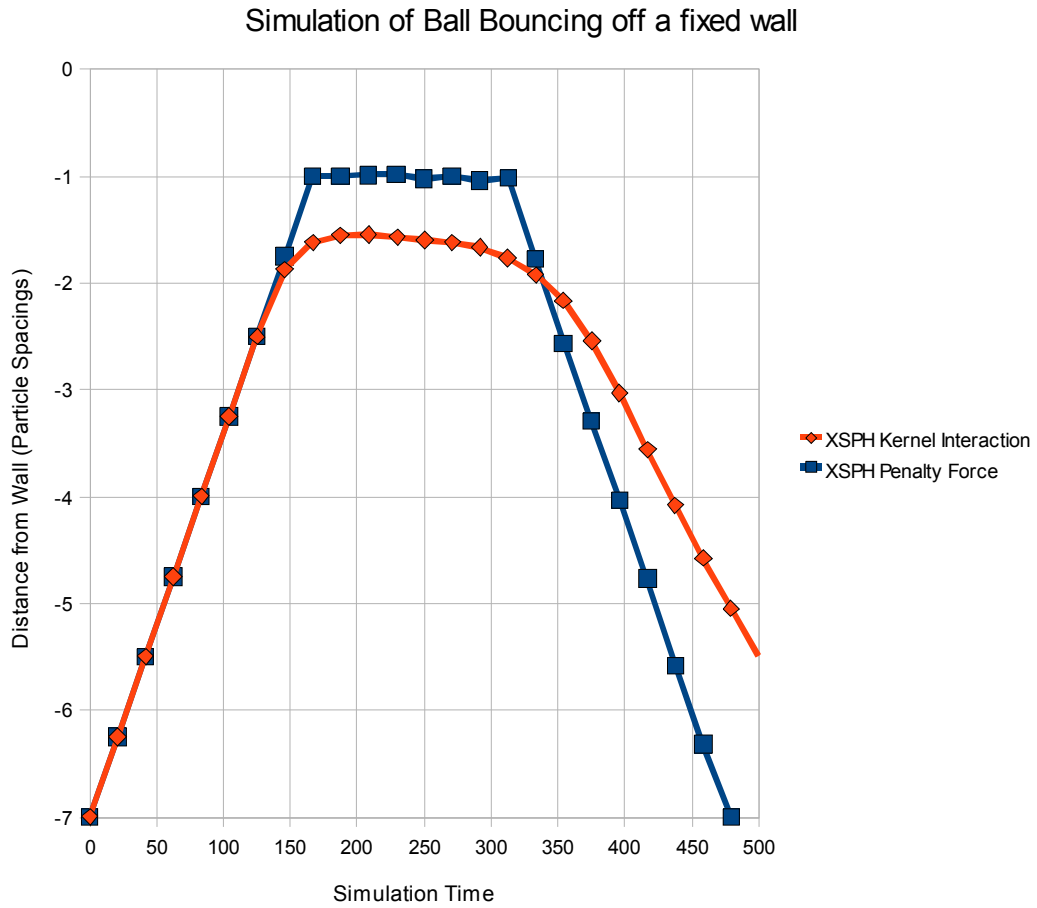


Fig. 4.7. Comparison between contact and kernel intentions

The difference between the kernel interaction and contact algorithm is shown in Fig. 4.7, it shows several improvements to the standard SPH approach. The most obvious is the improved delineation of the surface which can now be user defined rather than determined by the kernel size. The removal of the ‘fuzzy’ surface shows up where the kernel begins to interact 3 particle spacings from the fixed surface gradually coming to a halt and turning round. The particle interactions cause the velocity to slow on rebound as the energy to break the bonds is removed from the system. This pull-back effect is completely absent with the contact algorithm.

4.4. Friction

With a contact algorithm in place which applies forces only along normal vectors the kernel is no longer the controlling force in boundary interactions. This improvement relieves most of the problems associated with SPH at surfaces. There is no longer a fuzzy surface as all uncertainty about where a diffuse boundary begins and ends is controlled by an interaction parameter. Pull-back of surface particles no longer occurs as there is no attraction between particles on different surfaces, which required a sizeable force to remove a particle from the kernels interaction zone.

There is now no artificially generated friction, so particles are free to slide over one another, as long as the velocity vector is parallel to the normal vector. This is a huge improvement in SPH's ability to handle surface interactions as previously new bonds were continuously made and broken as the two surfaces slide over one another. The force required to break these bonds depends on material properties (shear modulus) and kernel interaction parameters (such as shape, h -size). In all cases the pseudo friction force generated was huge and practically prevented any sliding contacts from taking place.

Two approaches are available to physically model friction with SPH simulators; a traction based method which modifies the transmission of stress states across a boundary, and the classical mechanics approach which applies a force countering the direction of motion. Although the traction based method is more in keeping with the SPH methodology of transmitting stress states from one particle to another. It does require good estimates of the stress field near the surface, something that SPH

struggles with due to lack of interpolation near edges. It also struggles with highly deformed surfaces where only a handful of particles from each surface may actually be involved in the interaction.

The later ‘classical’ method extends the penalty force method by adding a friction force proportional to the penalty force. The direction of the friction force vector acts in the opposite direction to any tangential velocity difference between the two particles. Each particle pair interaction across a boundary is considered to be the equivalent of two mass elements rubbing past one another.

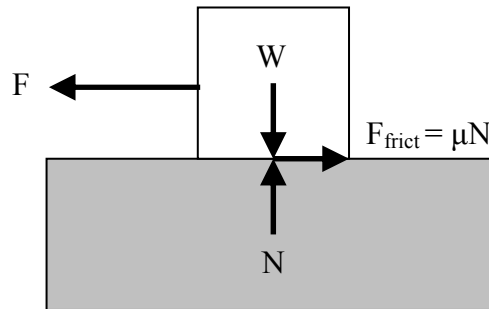


Fig. 4.8. A finite weight, W and associated normal force, N is required for the friction, F_{frict} to resist any accelerative forces, F .

The friction generated opposing to the direction of motion is given as

$$F_{\text{friction}} = \mu F_{\text{norm}} \quad (4.3)$$

where the coefficient of friction, μ , can be set by the user to give frictionless contact when $\mu = 0$.

F_{norm} can be conferred from the penetration algorithm with the addition of external body forces to generate a weight.

4.4.1 Simulations of Friction

In an idealized non friction situation when $\mu = 0$, there should be no resistance to motion as two bodies pass over one another. To test this, a series of 2D SPH simulations are setup as in Fig.4.9.

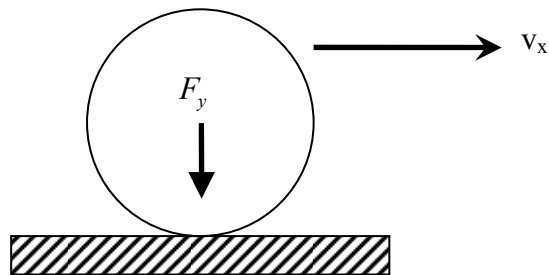


Fig.4.9. Simulation setup of ball sliding along a fixed surface

The displacement of the particle at the lowest centre of the ball is tracked, and plotted in Fig.4.11. Particles in the surface are fixed, but particles in the ball are free to move but experience a body force F_y giving the ball some weight and an initial velocity, v_x moving the ball along the surface.

As can be seen from a snapshot in Fig.4.10 and Fig.4.11, increasing the coefficient of friction results in the ball skipping across the fixed surface. The effect is more pronounced for higher coefficients of friction.

Although this is an improvement to the kernel only ball, K top left, which rapidly stops altogether, the excessive noise and shape change gives rise to less than optimal results.

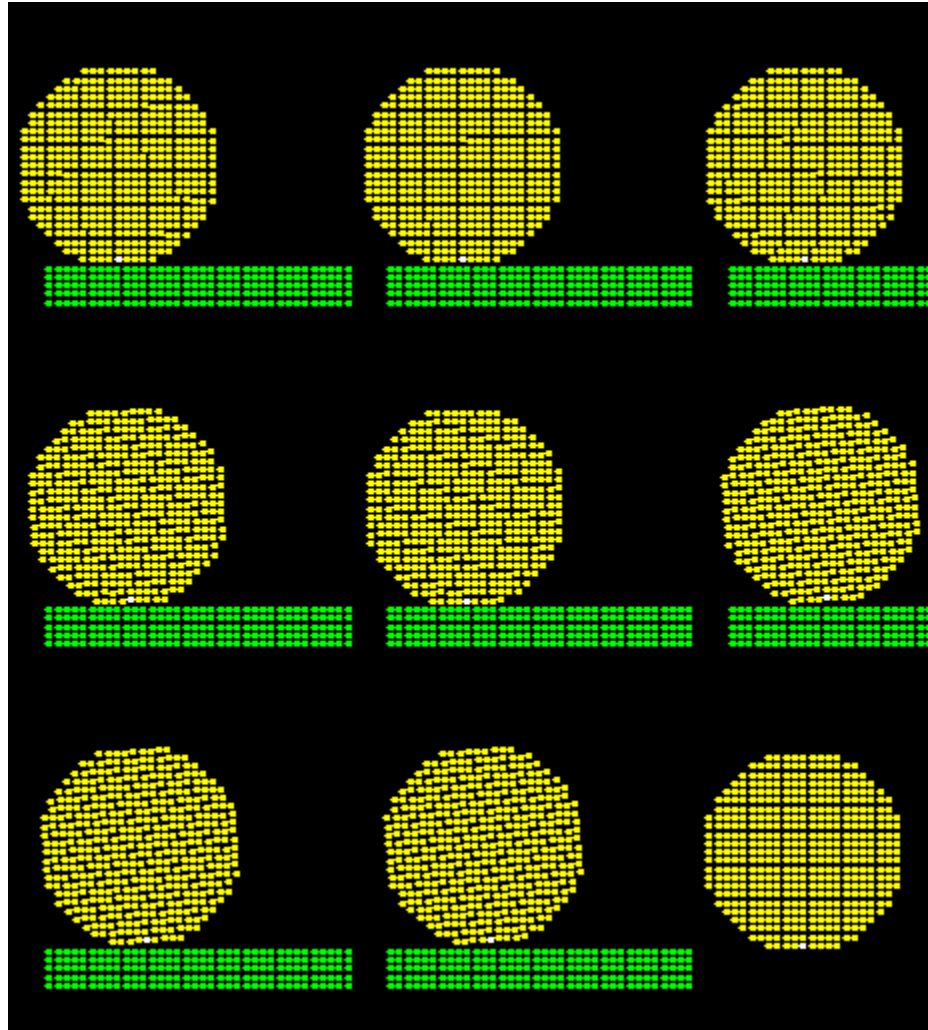


Fig.4.10.The coefficient of friction varies form left to right, top to bottom:

Kernel only interaction, 0.0, 0.2, 0.4, 0.6, 0.8, 1.0, 1.2

and No surface interactions.

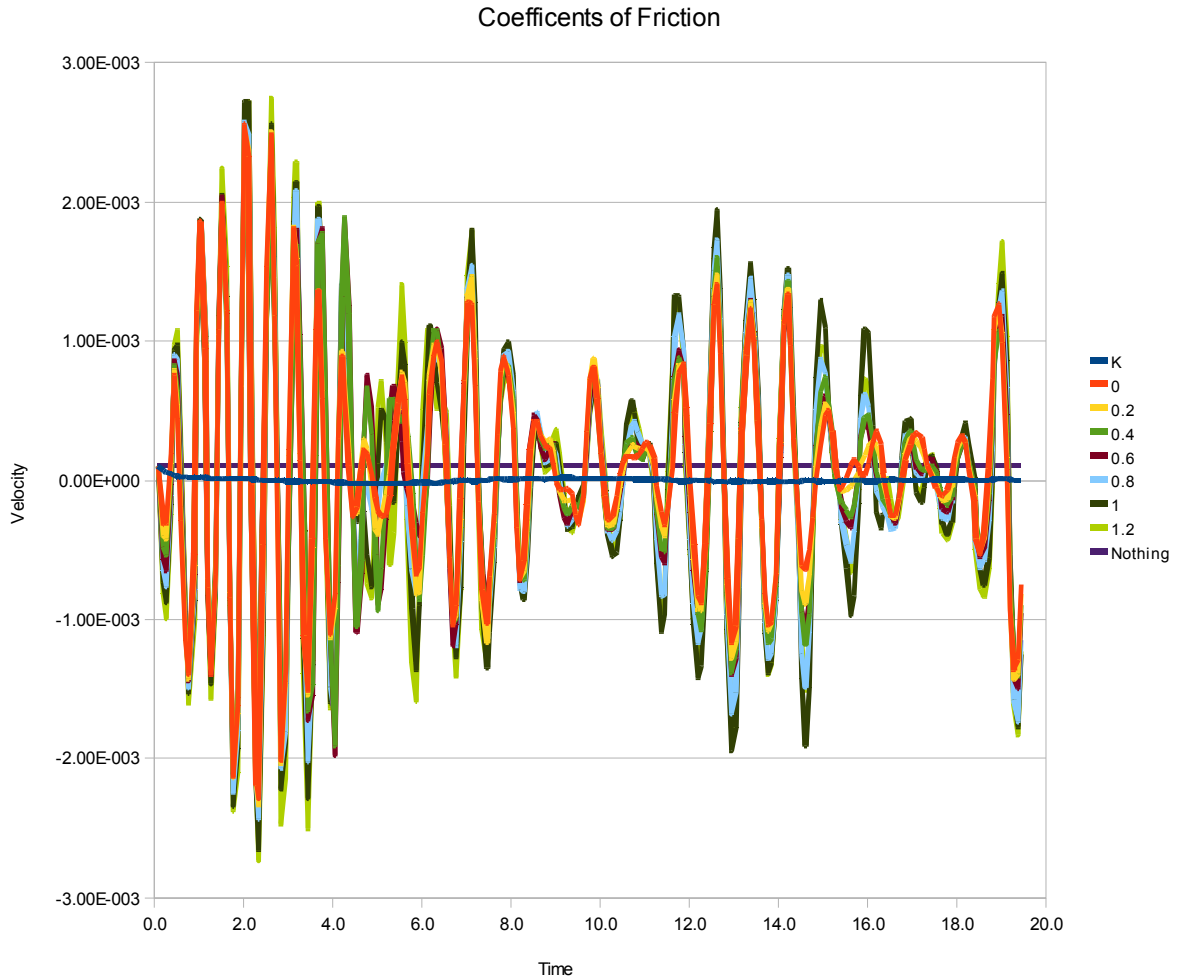


Fig.4.11.Velocity profiles for various coefficients of friction

As can be seen from Fig. 4.11 the noise is extremely high, and generally increases with larger coefficients of friction, but averaging over a long enough time period, gives the relationship in Fig. 4.12

Fig.4.12 shows that even with zero friction there is still some resistance to motion due to the shape changing force between the ball and the surface. The general trend of lowering velocity for increasing coefficients of friction matches expectations even if the excess noise makes any evaluation at a given time impossible.

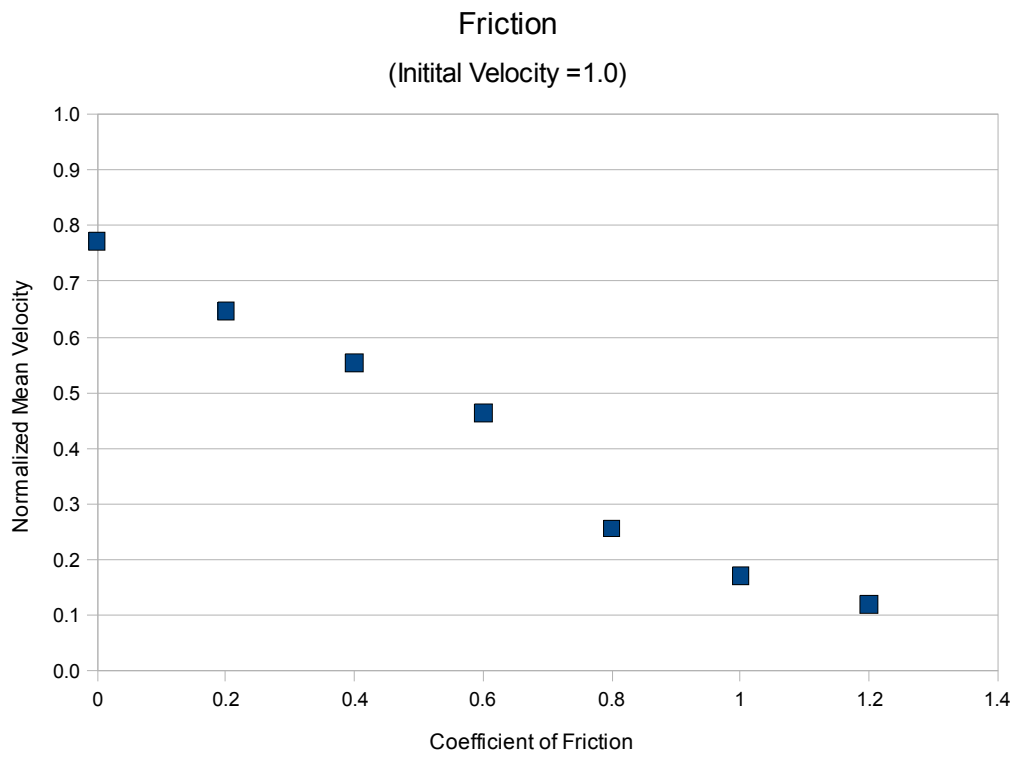


Fig.4.12. Long term average velocity dispersion rates resulting from the simulations of sliding contact with various coefficients of friction.

4.4.2. Rolling contact

A noticeable omission throughout the simulations is the lack of ball rolling that would be expected under friction. It has already been shown that XSPH is at least partially responsible for the lack of conservation of angular momentum. Removing the velocity smoothing that XSPH brings will increase noise still further, but as shown below does allow at least limited rolling contact to take place, Fig.4.13 shows a frictionless $\mu = 0$ interaction, while it still takes a very large coefficient of friction at $\mu = 0.6$ to initiate ball rolling, Fig.4.14.

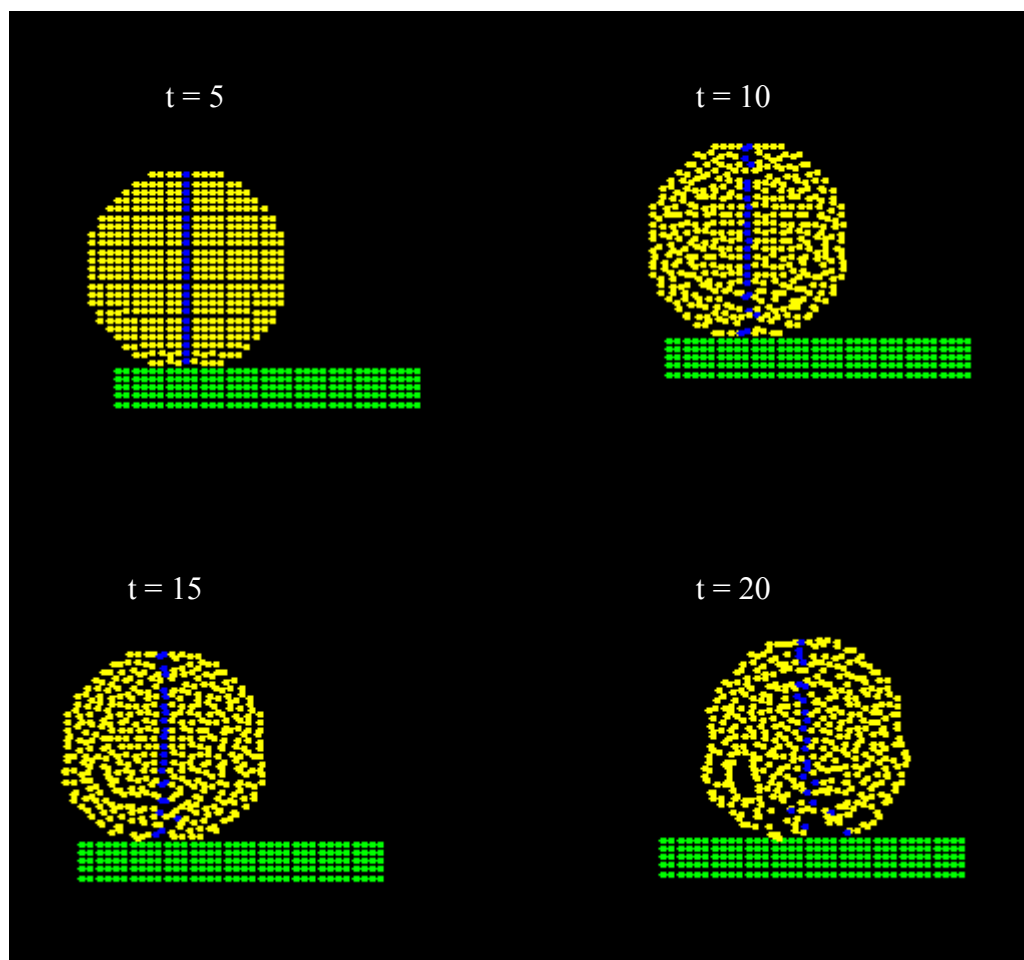


Fig.4.13. Simulation of contact-SPH ball sliding along a ‘frictionless’ surface without the presence of XSPH velocity smoothing.

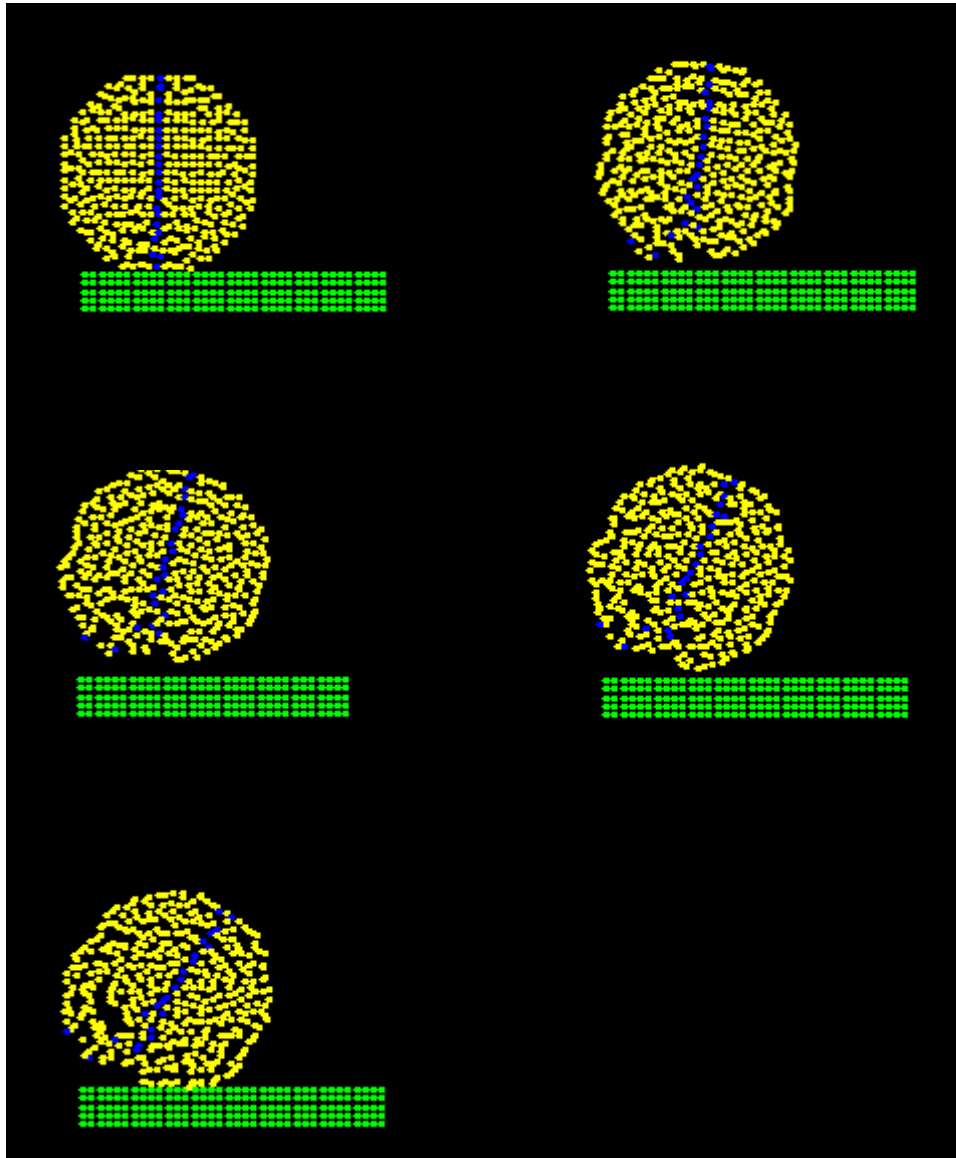


Fig.4.14. Contact-SPH ball rolling along a high friction surface (without XSPH)

4.5. Summary

This contact algorithm has been shown to reproduce select improvements to the problems of SPH when handling interactions across boundaries. It removes many of the unwanted side effects of the kernel interactions without sacrificing the mesh-free approach.

Non-linear Materials

5

5.1. Introduction

In this chapter, the basic solid SPH model of linear elasticity is extended to consider whether it is possible whether the method can be effectively used to model materials with a non-linear material constitutive response. Firstly, we look at elasto-plastic materials, in which the maximum stress is limited to a specific value and permanent deformation of the structure can results. This is analyzed within the context of the indentation and removal of a spherical indenter into a fixed substrate. Secondly, material failure by brittle crack growth is considered. Beyond a certain strain, a particle is considered to become damaged and its ability to sustain further strain is reduced until complete failure is possible. This model is investigated using the example of a failure of a plate containing an initial flaw. In each case, the material constitutive model is described and its limitations discussed within the context of the results.

5.2. Elasto-plasticity

Plastic deformation is the permanent deformation of a body mediated by the movement of dislocations within the crystal lattice. It can be introduced into SPH simulations at the continuum level by the introduction of an appropriate yield criterion. Gray and Monaghan (2004) considered the Von Mises yield condition for an elastic-perfectly plastic material. This common yield condition is widely applicable to ductile materials and uses the second deviatoric stress invariant J_2 , to determine if a material has begun to yield. It leads to permanent deformation above the yield stress, σ_Y , by reducing the amount of deviatoric stress that can be carried, increasing to the redistribution of stress inside the material to areas under lower stress.

In this model, the deviatoric stress tensor, S_{ij} , in the equation of state (2.39) is multiplied by a reducing factor, l , which is given by

$$l = \text{MIN} \left(\frac{\sigma_Y^2}{3J_2}, 1 \right) \quad (5.1)$$

where the second deviatoric stress invariant, J_2 is

$$J_2 = \frac{1}{6} \left[(\sigma_{11} - \sigma_{22})^2 + (\sigma_{22} - \sigma_{33})^2 + (\sigma_{33} - \sigma_{11})^2 \right] + \sigma_{12}^2 + \sigma_{23}^2 + \sigma_{31}^2 \quad (5.2)$$

Any von Mises stresses below yield stress σ_Y are not affected, as from (5.1) $l = 1$, and the material behaves as it would with the elastic body equation of state. If the von Mises stress exceeds yield then $l < 1$ and so the maximum von Mises stress on a particle cannot exceed yield. This model is readily implemented into the SPH code. It is now investigated within the context of an indentation test.

5.2.1. Indentation of an elasto-plastic substrate

A two-dimensional SPH simulation is constructed, as illustrated in Fig. 5.1. The substrate consists of a large rectangular block of particles, constrained in the vertical direction at its base. An indenter formed from SPH particles is forced downwards into the substrate under displacement control. It is then removed. The indentation velocity is small in relation to the speed of sound within the materials, such that the simulation can be considered to be quasi-static. The two bodies are identified as separate materials, such that they only interact through the action of the contact penalty forces introduced in the previous section.

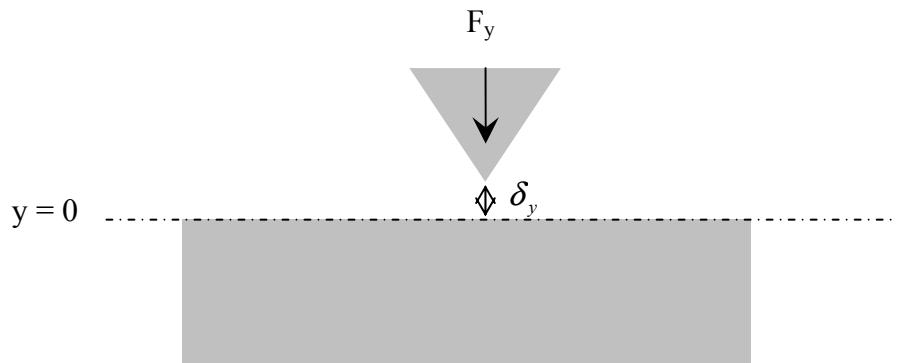


Fig .5.1. A schematic representation of the indentation simulation.

Firstly, the loading/unloading sequence is applied to a fully elastic substrate. The load-displacement curve is shown in Fig. 5.2. As expected the force increases non-linearly with the indentation depth due to the increase in the contact area between the spherical indenter and the substrate. The unloading curve is almost exactly coincidental with the loading curve, as expected for a fully elastic system. In contrast, Fig. 5.3 shows the results of applying the loading /unloading sequence to an elasto-plastic substrate. Here we have taken the yield stress to be $\sigma_y = 0.001E$ which

is a typical ratio for most metals. In this case, the large penetration enforced on the elastic substrate is not possible due to the early onset of plastic yielding. The non-linear geometry of the indenter does not have such an effect on the change in the indentation force in this case, due to the yielding and stress redistribution in the material beneath the indenter. Upon unloading, the difference between the loading and unloading paths is clear, and indicates that irreversible plastic deformation has taken place. The difference between the areas under the loading and unloading curves is the plastic work done during the deformation. The apparent slight increase in work done during unloading in the linear elastic case, Fig. 5.2, can be attributed to particle rearrangement and consequent changes to the internal energy of the system.

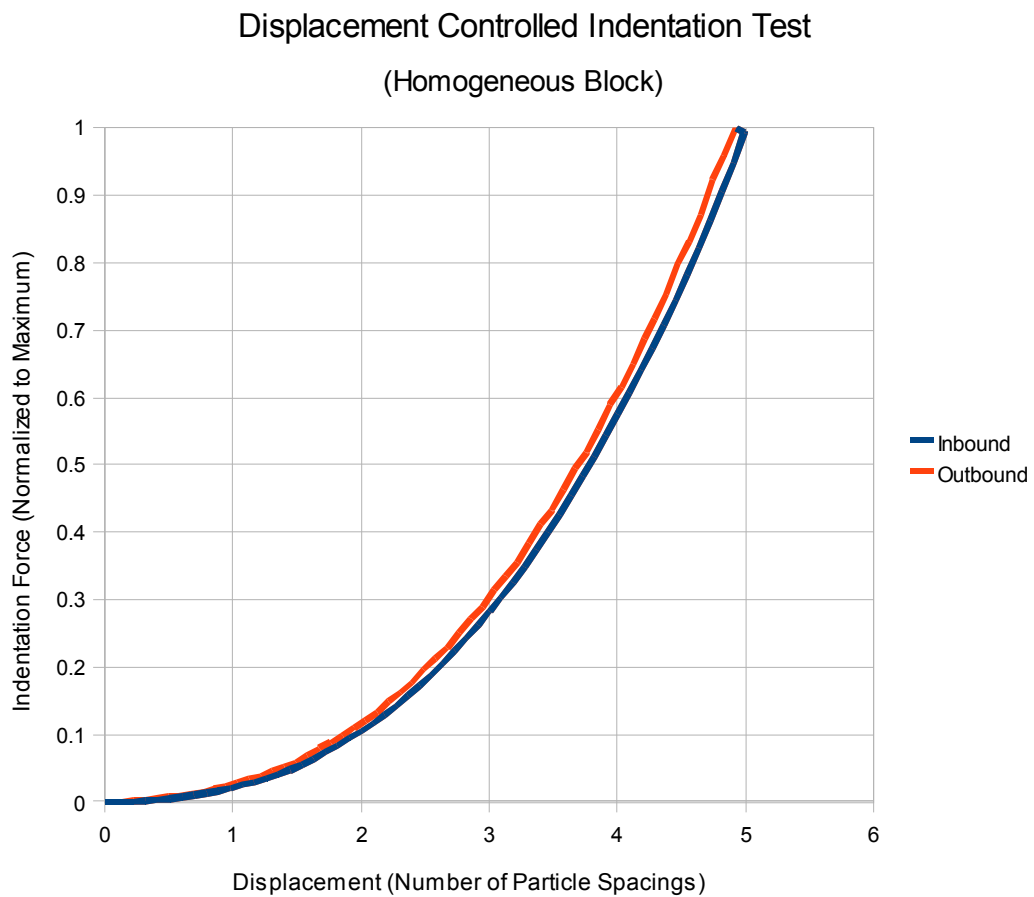


Fig.5.2: The load-displacement curve for the indentation of a elastic substrate.

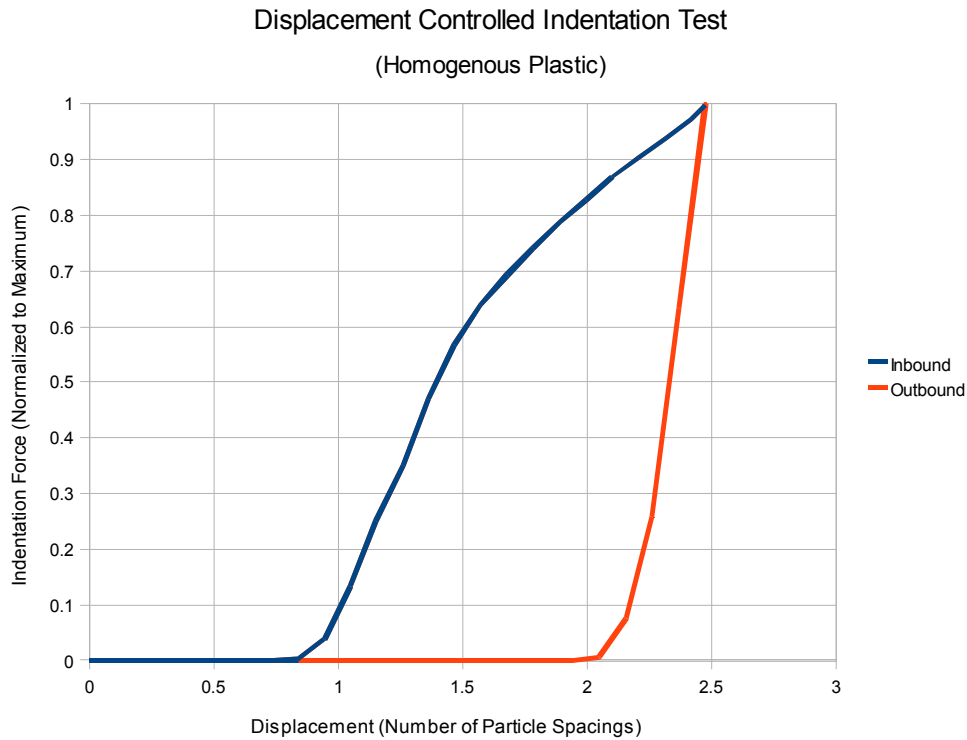


Fig.5.3. The load-displacement curve for the indentation of an elasto-plastic substrate.

The contact algorithm is found to work effectively in both the elastic and elasto-plastic cases, with no residual interaction between the bodies upon separation. The surface profiles of the substrate at different points in the two cases are shown in Fig. 5.5. Fig. 5.5a shows the profile during the early stages of indentation of a fully elastic substrate. Fig. 5.5b shows the similar situation when plasticity is introduced. In this case, plastic pile-up of material around the indenter is clearly visible. For reference, fig. 5.5c shows the case upon unloading of an elastic substrate where no special contact algorithm is employed and the indenter and substrate simply interact as traditional through the kernel. It is clear that the response is unphysical, resulting in a negative indentation force and an upward “suction” force on the substrate.

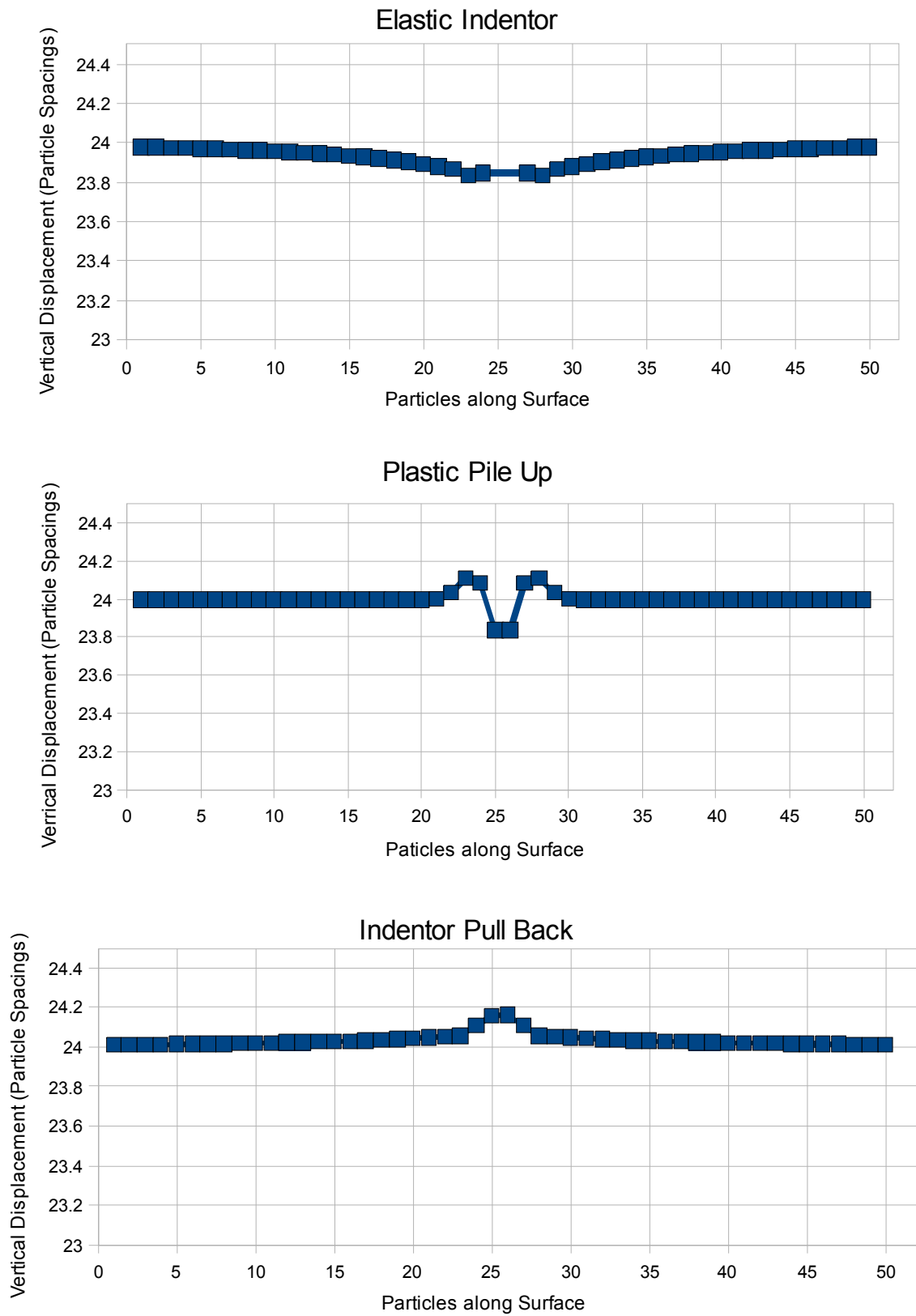


Fig. 5.5 : Surface profiles of the substrate at different points in the loading/unloading sequence for the two cases (a) during elastic indentation, (b) during plastic indentation, and (c) upon unloading without use of a proper contact algorithm.

5.3. Damage mechanics

This section considers the application of a brittle failure model, typical to that used to describe the failure of interfaces or brittle materials. In theory, modeling many aspects of this phenomenon should be a strength of the meshless SPH method, as it naturally allows for regions of a body to separate and undergo large changes in shape and connectivity without the need for boundary tracking and remeshing that hinder the application of conventional mesh-based methods to these types of problems.

5.3.1. Modeling failure through the kernel

The initial approach was to model failure through the natural separation of the body by severe deformation causing particles to effectively stop interacting once they were outside the range of the kernel. In some senses, this is like an atomistic model, in that the particle interaction is defining the failure criteria, rather than any physical process that can be identified at a continuum level. This means that the criteria for failure cannot be readily manipulated to fit a particular material response. However, this method has the benefits of simplicity and its application has been investigated in the context of two cases:

(i) Propagation of a crack around a stiff obstacle

In this case, a crack is initially introduced into a square array of SPH particles by removing some of them to create a notch. A subset of particles is then identified within a diamond shaped region in front of the crack. The elastic modulus of these

particles is increased by a factor of 2. An increasing load normal to the crack face is then gradually applied on the upper and lower boundaries of the body. At a critical load, the crack starts to propagate forwards. Once the crack meets the hard obstacle, it changes direction to avoid it. It propagates along the interface between the particle and the obstacle, as shown in Fig. 5.6, and continues forward once it has past it. As with many SPH simulations, the overall picture of the evolution is generally pleasing, demonstrating a qualitatively physically representative response.

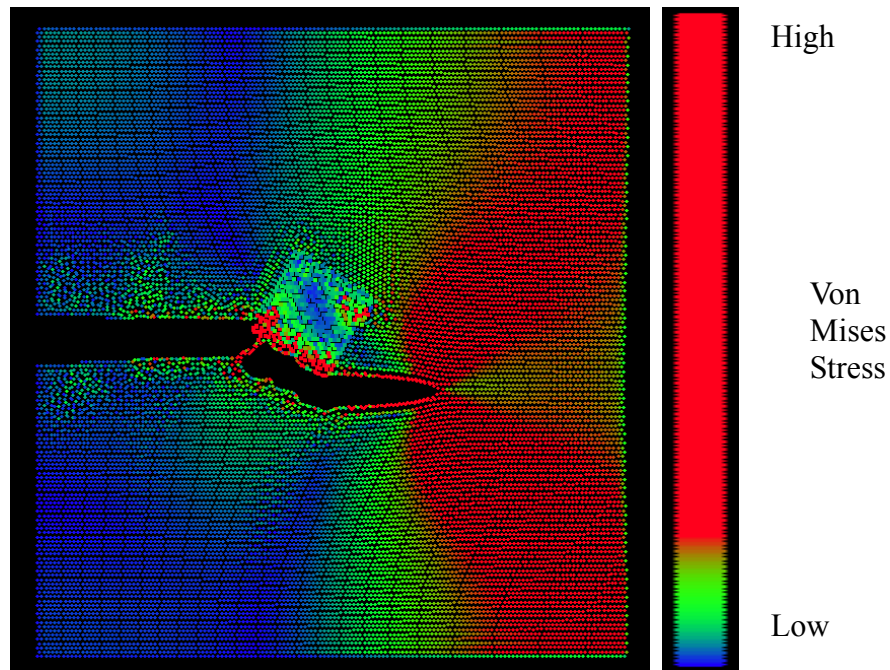


Fig.5.6 : Snapshots in the evolution of a crack around a hard obstacle. The evolution of damage in the body arises from the kernel only.

(ii) Crack propagation through a fibre-reinforced composite

Carbon-fibres can be introduced into a metal matrix in order to increase there resistance to the propagation of cracks. The fibres can halt or deflect the direction of

growth of a crack. In some cases, the crack can be halted by the fibres, but the resulting increase in stress on the other side of the fibre and result in the nucleation of a crack at that point. Hence, by this mechanism, the crack can continue through the body. As the crack leaves continuous fibres behind it, the additional stress on the bridging fibres can cause them to be extracted from the matrix due to slip at the fibre-matrix interface, or by simple brittle failure of the fibres. For the SPH model in this case, the crack is introduced as in the previous model. It is orientated perpendicular to the fibres, which are given an increased elastic modulus by a factor of 2 above that of the matrix. As can be seen from the series of snapshots in Fig. 5.7, the crack is initially halted by the first fibre but then, as the load is increased further, the crack renucleates on the other side and continues to propagate further. As above, the images seem to be physically reasonable.

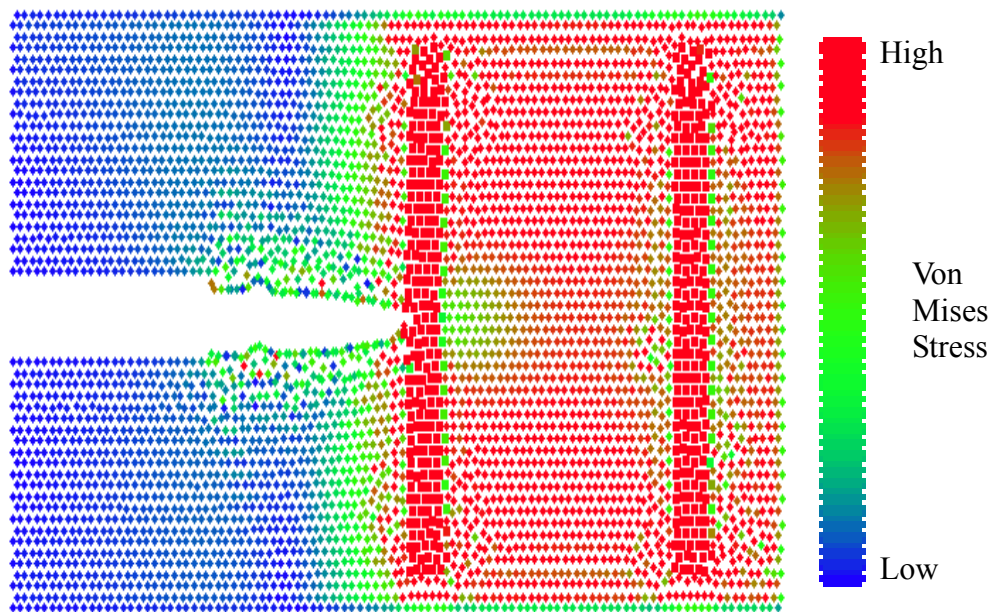


Fig.5.7. Snapshots in the evolution of a crack through a fibre-reinforced composite.

The evolution of damage in the body arises from the kernel only.

Although these images look reasonable, there is one major consideration that cannot be ignored. One of the major disadvantages of SPH is that the shape of the Kernel can affect results. Kernels can be selected for particular properties with custom kernels offering better solid edge/interface detection or increased stability in tensile strain. The Kernel also currently defines the fracture conditions as opposed to any physical mechanics. Here cracks open out until the two surfaces no longer interact with one another as they are outside the kernel range, and complete fracture can be said to have taken place. A true physical model should solve the underlying physical equations without the mesh or meshless representation of the body influencing the results. With this in mind, we proceed to the next sub-section, to consider the application of continuum damage models.

5.3.2. Continuum damage models

In continuum damage models, the state of damage is represented by a Damage parameter., SPH can be modified to include a Damage Parameter in a similar way to the introduction of particle type in composites. Damage is ranked from 0 to 1 with 1 representing complete failure (i.e. the inability to carry any more load) and 0 as unharmed. The shear modulus of damaged particles is then consequently modified in a consistent way. This will be the first new topic to be addressed, and will introduce a more physical fracture toughness parameter for finer control over material constants.

Typically, damage models are used to apply statistical information about a materials fracture behaviour as a bulk material property. Based on the principle that all

materials contain a multitude of hair line cracks which are present due to production and working processes. In order to simplify the situation it is usually assumed these flaws are distributed evenly throughout the material. Under load these cracks enlarge, weakening the material, until at a critical length cause complete failure.

In the case of many computer simulations, individual discrete elements of material are modelled with the bulk material responding as the collection of elements. Adding damage modelling into such a solution requires damaged areas to be gradually weakened by some factor and then removed entirely when they can carry no more load. The Damage Parameter, $0 \geq D \geq 1$, is commonly defined as between 0 (No Damage) and 1 (Full Damage). It can be included in linear elasticity by modification of the local elastic modulus such that

$$E(D) = \begin{cases} (1-D)E & \text{if } \sigma > 0 \\ E & \text{if } \sigma < 0 \end{cases} \quad (5.3)$$

where the loading bearing capacity of the material is only reduced in tension, but it still capable of supporting a normal load in compression. Damaged areas are typically surrounded by regions of weakened material caused by stress concentration, as shown in Fig. 5.8. The areas around the fully damaged zone (crack) carry more load and consequently start to become damaged leading to propagation of the crack.

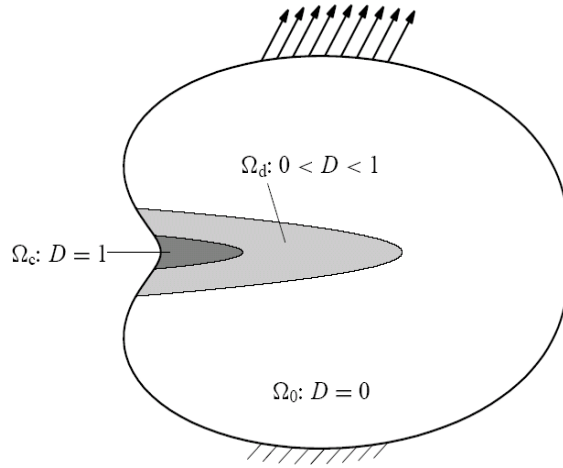


Fig. 5.8: A crack is defined by an area of complete damage ($D=1$).

The areas around the crack carry more load and consequently start to become damaged leading to propagation of the crack.

(from Peerlings,1999)

There are many different methods for defining how the damage parameter evolves, depending on the type of simulation. A simple theoretical model has a linear softening response (after Peerlings, 1999) where the maximum principle strain, ϵ_{MAX} , increases past the initial damage threshold, κ_0 , and reaches maximum damage (complete failure) at the critical strain κ_c . The damage parameter is therefore related to the instantaneous strain state of a particle according to

$$D = \begin{cases} 0 & \text{if } \epsilon_{MAX} < \kappa_0 \\ \left(\frac{\kappa_c}{\epsilon_{MAX}} \right) \left(\frac{\epsilon_{MAX} - \kappa_0}{\kappa_c - \kappa_0} \right) & \text{if } \kappa_0 < \epsilon_{MAX} < \kappa_c \\ 1 & \text{if } \epsilon_{MAX} \geq \kappa_c \end{cases} \quad (5.4)$$

The resulting uniaxial stress-strain response of a damaged particle is therefore as shown in Fig. 5.9.

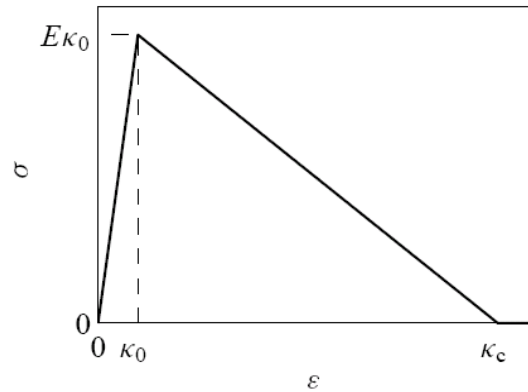


Fig. 5.9: Stress-strain curve for a linear (strain softening) damage model response. (from Peerling, 1999)

This simple damage model has been encoded in the two-dimensional SPH code. Benchmark tests when conditions approximate uniaxial loading have been run. These are now compared and discussed in the context of some of the results in the literature for other damage models.

Gray and Monaghan (2004) favoured initially implementing the random seeding of damage throughout the body. Test results can show flaws developing when a random distribution of weak point lines up, see Fig.5.10. This randomization process, although in many ways mimics the real world, causes problems when spurious failure occurs, as if is not known whether this is due to some random feature or a control factor. Assigning multiple flaws to each particle eliminates some of this defect by limiting damage to the ratio of activated to total flaws per particle. Although this is difficult to compare in a physical sense to microscopic crack formation which has no such limitations.

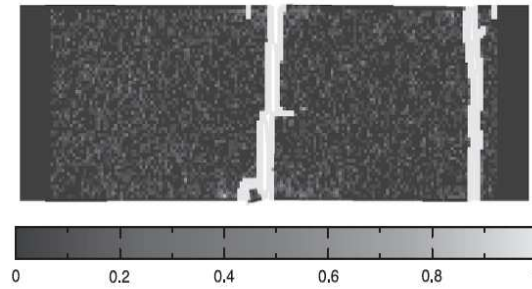


Fig.5.10. Additional fracture path caused partly by a randomly seeded weakness in the SPH particles. (From Gray and Monaghan, 2004)

More worrying is the extreme sensitivity to initial conditions that occurs in the Grady and Kipp (1980) continuum damage model. Simulations carried out for this thesis show that without fine tuning of the parameters unrealistic damage may occur as shown in Fig.5.11. It is important to note that an exact replication of Monaghan results is impossible to achieve due to some errors and omissions from his work, efforts have being made to clarify some of the finer details.

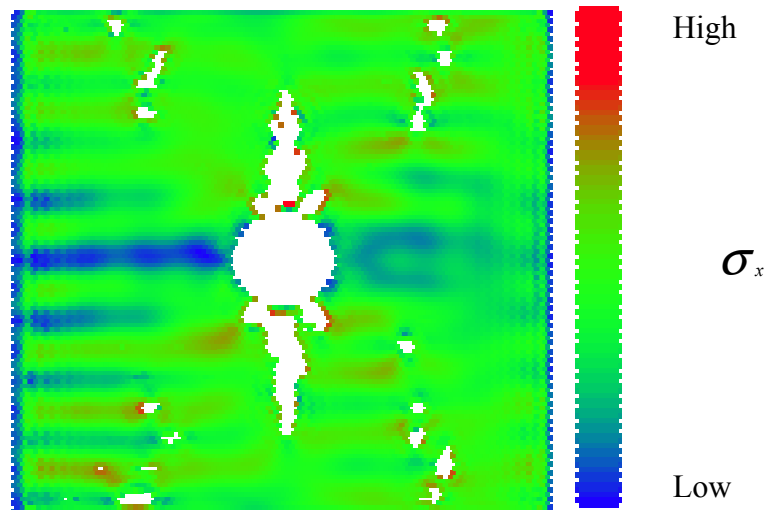


Fig.5.11: Additional Flaws on the diagonals (White area, Damage = 1) developing in an isotropic medium with a central hole. Careful selection of the Grady-Kipp Fracture Parameters is required to remove this effect.

With these limitations in mind, the damage model of (5.4), based on a Peerlings (1999) type approach, has been implemented into the SPH code. With no need for an initial damage distribution to be specified, it removes the random nature of the previous models. Although this does require a seed feature to concentrate stress and damage in an isotropic material. Previous studies of stress concentration about an circular hole have been used to calibrate SPH in Section 3.2. In simple uniaxial load cases the maximum strain can be identified without the computationally costly step of calculating the principle strains, by selecting ϵ_{xx} or ϵ_{yy} . Fig.5.11 show a central region of completely damaged particles ($D = 1$) used to mimic the presence of a hole. The simulation results in the concentration of stress around the hole, leading to high strain and corresponding damage accumulation. Results shown in Fig.5.12 attempt to replicate the results of Monaghan (Gray and Monaghan, 2004) using a bar with a slight waisting to concentrate stress in the central zone. This type of waisting would naturally be expected when plastic effects are introduced, as in the previous section.

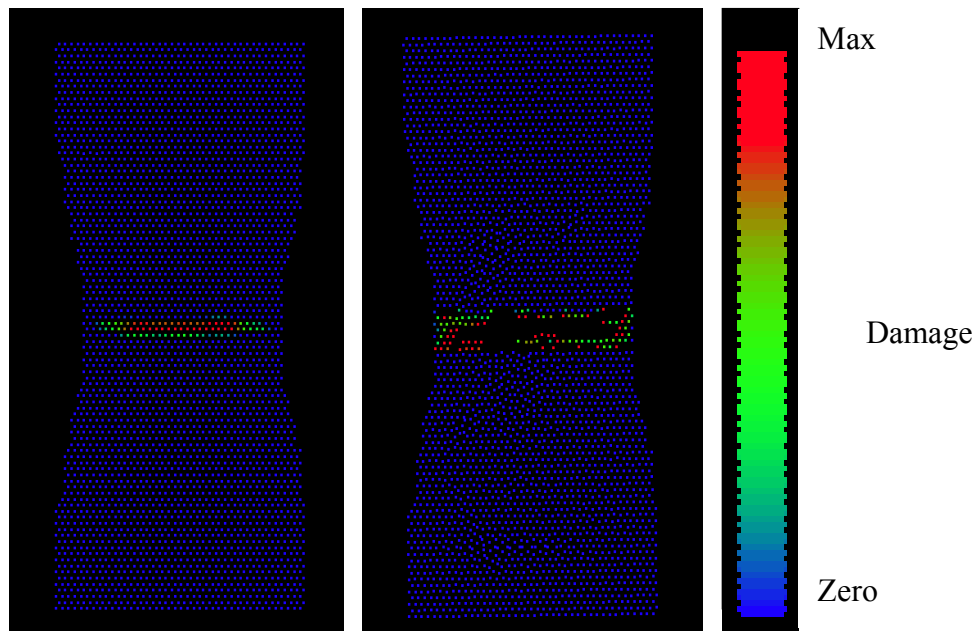


Fig.5.12. Early and Late Damage in a slim waist but isotropic sample.

Note the concentrated damage about the high strain zone

As expected damage accumulates where tensile strains are at their peak. With damaged particles not able to carry as much load they pass the force onto their neighbours causing further stress concentration, and spreading damage.

Although this result is physically reasonable, problems can arise in more dynamic situations, where small regions of damage appear where there is no apparent prolonged stress. These areas of low damage are caused by shock waves propagating in the material causing large instantaneous fluctuations in the strain. These are dampened out by the artificial viscosity term in the SPH force calculation, but too late for them to limit the extent of damage. Practically, it may be more appropriate to introduce a damage evolution rate, \dot{D} , where the damage accumulates over a prescribed time scale and its therefore less sensitive to large but rapid fluctuations in the strain on a particle, which are typically seen in SPH.

5.4. Summary

In conclusion, the incorporation of a damage model into SPH goes some way to remove the kernel dependency of fracture conditions. Fracture is no longer defined as when particles are separated by more than one kernel length. Although the kernel still plays a role in spreading the damage and defining how the shocks spread and further weaken the material. A basic tensile test with simple uni-axial loading has been simulated. Along with a reliable plastic deformation system, non-linear materials can be modelled using SPH.

Buckling

6

6.1. Introduction

In this chapter, the application of SPH in the analysis of buckling phenomena is investigated in the context of the stability of two-dimensional columns. As the position of the surface of a solid is not precisely defined in SPH, it is of interest to determine what the effective thickness of an SPH strut is, in relation to classical buckling theory. Also, as the strain varies linearly across the cross-section of a beam subject to a bending moment, it is important to determine how many SPH particles are required to represent this non-uniform strain field to model the problem with sufficient accuracy. In addition, one of the essential benefits of SPH is the modelling of large deformations, so this will be considered towards the end of the section. Firstly, however, the elementary theory for the determination of the onset of buckling is reviewed for the situations considered in the next sub-section.

6. 2. Classical buckling theory

(a) Fixed-fixed boundary conditions

Consider an elastic bar of length L with the bottom end fixed in all directions, and the upper end fixed in all but the vertical under the action of a vertical compressive load, P , as shown in Fig. 6. 1. A reacting moment, M_0 , develops at the fixed ends post buckling to retain the vertical alignment of the bar at the two ends.

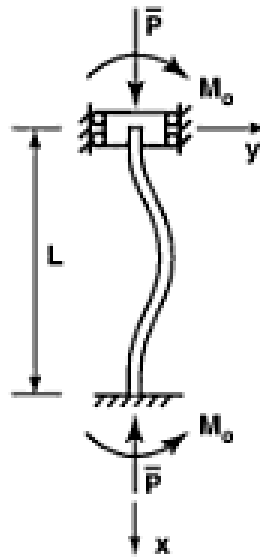


Fig.6.1. Support for a rod under fixed-fixed constraints (from Jones, 2006)

In this case a point along the length of the bar, x , will feel the bending moment,

$$M = Py - M_0 \quad (6.1)$$

where $y(x)$ is the horizontal displacement of the middle of the bar. For a linear elastic material, the bending moment is related to the deformation of the beam by

$$M = EI\kappa \approx -EI \frac{d^2 y}{dx^2} \quad (6.2)$$

where κ is the curvature of the beam, E is the Young's modulus and I is the second moment of area of the beam.

Equation (6.2) is a valid approximation for the curvature for small deformations, which is valid for determining the onset of buckling but not necessarily the subsequent large deformation of the beam under continued loading.

The Euler equation of buckling is hence derived from (6.1) such that

$$\frac{d^2 y}{dx^2} + k^2 y = \frac{M_0}{EI} \quad (6.3)$$

where

$$k^2 = \frac{P}{EI} \quad (6.4)$$

The solution to (6.3) is of the form

$$y = A \sin(kx) + B \cos(kx) + \frac{1}{k^2} \frac{M_0}{EI} \quad (6.5)$$

where A and B are defined by the boundary conditions of the problem.

For the fixed-fixed boundary conditions, at the top of the bar when $x = 0$ then $y = 0$

Substitution into equation (6.3) leads to

$$B = -\frac{1}{k^2} \frac{M_0}{EI} \quad (6.6)$$

Since the top can not rotate then $\left. \frac{dy}{dx} \right|_{x=0} = 0$. Hence (6.5) gives

$$A = 0 \quad (6.7)$$

Now at the base of the bar, when $x = L$, the fixed nature implies $y = 0$, and (6.5)

becomes

$$\cos(kL) = 1 \quad (6.8)$$

(6.8) occurs only when $kL = 2n\pi$, where $n = 0,1,2,\dots$ is a positive integer. This also

satisfies the fixed condition to the bottom of the bar $\left. \frac{dy}{dx} \right|_{x=L} = 0$ which requires that

$\sin(kL) = 0$. The lowest frequency non-trivial solution occurs when $k = \frac{2\pi}{L}$.

Substituting back into (6.4) gives the critical load for the onset of buckling, \bar{P} , to be

$$\bar{P} = 4\pi^2 \frac{EI}{L^2} \quad (6.9)$$

Other solutions occur at $n = 2,3,\dots$ etc. These eigenvalues represent higher modes of buckling, as seen in Fig. 6.2. These higher modes all correspond to higher critical buckling loads so they are not expected to be realised unless unnaturally forced through further constraint (e.g. due to contact with adjacent obstacles) or dynamics effects (it is worth remembering that SPH is essentially a dynamic model which is only expected to reproduce this type of static response in the quasi-static limit). Hence the first eigenvalue (6.9) is considered to be the expected critical buckling load.

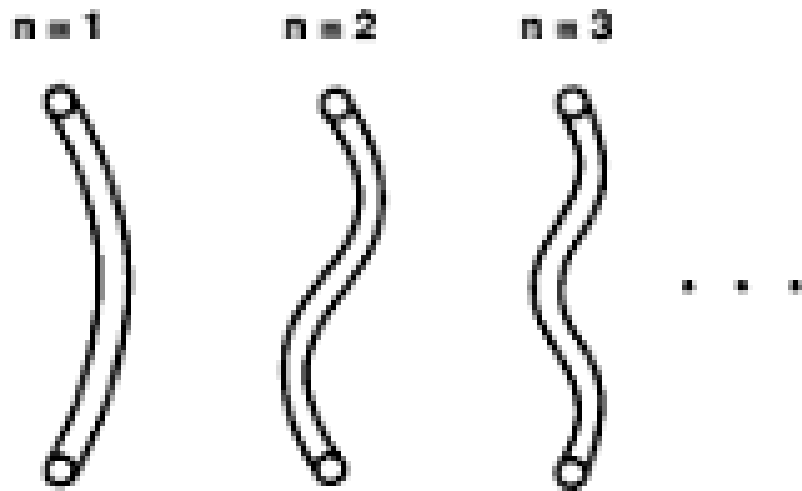


Fig.6.2. Different modes of buckling

(from Jones, 2006)

The shape of the buckled beam is now fully defined by (6.5) and is given by

$$y(x) = B \left[\cos\left(\frac{2\pi x}{L}\right) - 1 \right] \quad (6.10)$$

where the precise amplitude of the buckle, B , is related to the downward vertical displacement of the top of the bar (which is not considered here).

(b) Fixed-free boundary conditions

The analysis of this case is similar to that of the previous fixed-fixed case, and hence will not be derived in such detail. Here a bar has the bottom end fixed in all directions as before, but the upper end is free to move vertically or horizontally, as shown in Fig. 6.3. Hence the applied moment at the top of the bar is zero, and the reacting moment, M_0 , that develops post buckling is at the bottom fixed support.

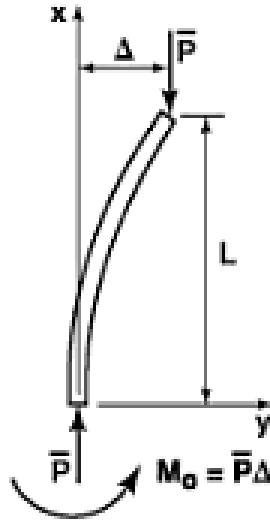


Fig.6.3. Idealized support for a rod with fixed-free constraints

(from Jones, 2006)

In this case the distance along the bar, x , is taken from the bottom of the strut. A point along the length of the bar will experience a moment of the form (6.1) as before.

Given the horizontal displacement at the top of the bar is $y(L) = \Delta$ then the reactive moment in this case is $M_0 = P\Delta$. The Euler buckling equation (6.3) still applies,

with a solution of the form (6.4) and (6.5) as before. The boundary conditions

$y(0) = 0$ and $\left. \frac{dy}{dx} \right|_{x=0} = 0$ at the fixed bottom end remain the same, with only

$y(L) = \Delta$ at the free top end. These conditions yield $A = 0$ again, and

$$\cos(kL) = 0 \quad (6.11)$$

which occurs when $kL = (n + \frac{1}{2})\pi$, where $n = 0, 1, 2, \dots$ is a positive integer. The

lowest frequency non-trivial solution occurs when $n=1$, i.e. $k = \frac{\pi}{2L}$.

Substituting back into (6.4) gives the critical load for the onset of buckling for fixed-free end conditions, \bar{P} , as

$$\bar{P} = \frac{\pi^2}{4} \frac{EI}{L^2} \quad (6.12)$$

This is 16 times smaller than the solution found for a fixed-fixed bar, as the buckling wavelength is four times that of the fixed-fixed case. The corresponding horizontal displacement along the length of the strut is

$$y = \Delta \left[1 - \cos\left(\frac{\pi x}{2L}\right) \right] \quad (6.13)$$

where the buckling amplitude, Δ , is related to the downward displacement to the top of the strut.

6.3. SPH simulation of buckling

The simulations use the two-dimensional SPH code for large deformation linear elasticity. The boundary conditions are implemented through constraining the displacements of some of the end particles in the horizontal and/or vertical directions, as shown in Fig. 6.4. This prevents the use of pinned joints from being studied here, as rotation without translation is not possible. The strut is taken to be L particles long (with unit spacing) and t particles wide.

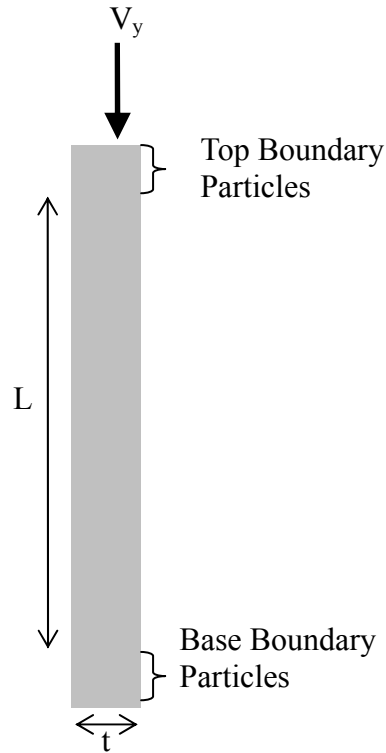


Fig.6.4. Loading conditions for SPH simulations of buckling.

The unsupported length of the rod, L , is shorter than the total length as the top and bottom 3 rows of particles are used to place constraints on the rod and hence are fixed relative to their initial positions. In fixed-fixed configuration the particles at the base of the rod are completely fixed and cannot move in either the horizontal or vertical directions. In order for the compressive load (P) to be applied the top boundary particles are free to move vertically but are horizontally constrained. In the fixed-free configuration the base particles remain as before, but the top particles are not constrained, but are still given the additional external compressive load (P).

A force controlled compressive load is applied to the top boundary particles. The loading rate is slow (less than 0.1% the speed of sound) to leave time for elastic shock waves to travel the length of the rod and communicate the action of the applied load to all the particles in the body. Hence the particles should all be roughly in force equilibrium although necessarily they will still retain some oscillatory (thermal) kinetic energy. The results are in the quasi-static limit and hence should be approximately comparable to the analytical results for the fully static case above.

Theoretically, a mathematically perfect structure is stable to buckling. In order to facilitate the onset of buckling a small distortion is initially placed upon the rod mimicking real life defects present in any material. This is achieved by applying a very low amplitude high frequency sin wave along the rods lateral direction. This perturbation of the order 0.1% of the rods thickness is designed to be pseudo random in nature, and is preferable to a random number generator as it can be easily reproduced. Without such perturbations a perfectly straight rod can withstand many times the normal buckling load in unstable equilibrium, eventually buckling due to the accumulation of numerical errors due to the precision limit of the computer processor.

An example of the typical evolution of an SPH simulation of a strut under buckling is shown in Figs 6.5 for fixed-fixed and fixed-free end conditions. The behaviour appears qualitatively to be physically realistic. However, the quantitative agreement with buckling theory is investigated in the following sub-sections.

(a) Comparison with predictions for the deformed shape of the strut

The first task is to show that SPH simulations have the ability to match the analytical solutions presented above. For a fixed-fixed rod and a fixed-free rod the deformed shape of the rod is recorded when the maximum amplitude equals 1% and 5% of the rods thickness. These results are presented in Figs. 6.5 and 6.6 for a rod of length 80 and thickness 4 particles, along with the theoretical prediction given by (6.10) and (6.13). Displacements are normalized by the length of the rod.

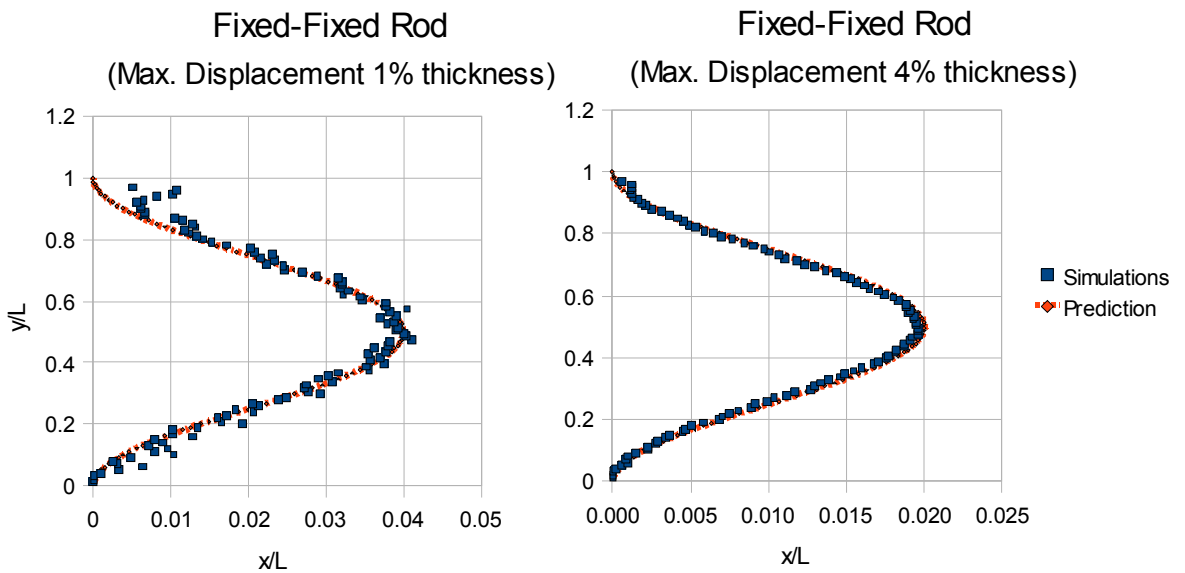


Fig. 6.5. Comparison of simulation and prediction for the buckled shape of a fixed–fixed rod

The fixed-fixed rod shows a close match with the predicted cosine waveform. At low displacements, the simulation is still heavily affected by the noise of shockwaves as they propagate through the system. Once the initial shocks have dissipated in the later case the simulation matches predictions extremely well.

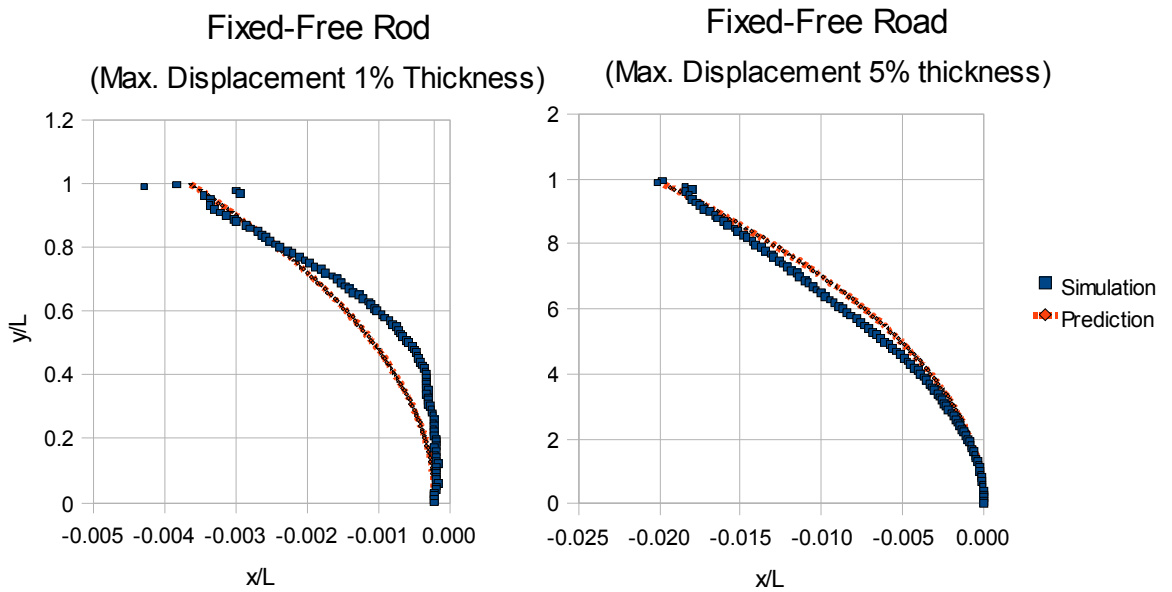


Fig 6.6. Comparison of simulation and prediction for the buckled shape of a fixed-free rod

For the fixed–free rod the lack of constraints on the system make the initial shockwaves more prevalent and results in a larger mismatch to the predicted shape. These shock waves can propagate along the length of the rod and the free end can continue to vibrate for sometime. However, as in the fixed-fixed case, once the system has settled down in the later stages, the comparison is very reasonable. Hence we can conclude that, in this respect, the SPH simulations are giving reasonable results for small deformations just after the onset of buckling.

However, most simulation methods are able to match the predicted results for these small deformations. For larger displacements buckling becomes a highly non-linear phenomenon. Analytical solutions have to give way to more complex numerical approximations (see Jones, 2006). It is in these circumstances that the advantages of the dynamic SPH formulation are expected to be most prevalent. Fig. 6.7a shows the results for the shape of an SPH fixed-free rod which has undergone very large

deformations to induce a 90° rotation of the free end. This is compared with the predictions of the non-linear theory in Fig. 6.7b. The comparison is very reasonable and suggest that the SPH model is performing correctly in this limiting situation.

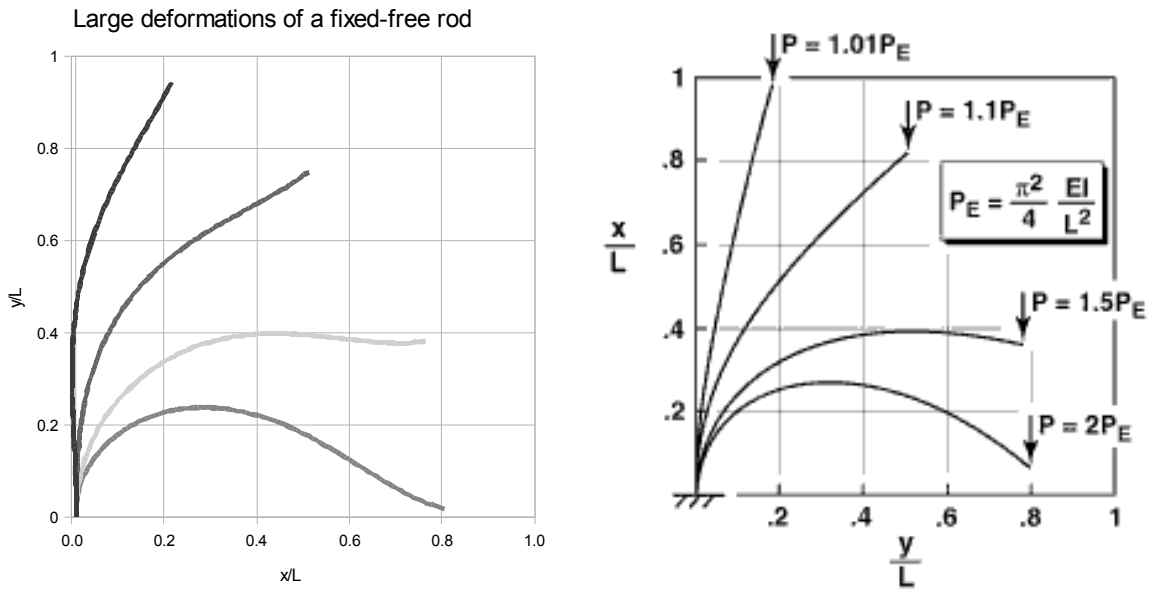


Fig.6.7. The buckled shape of a fixed-free rod undergoing large deformations

(a) SPH simulation, (b) non-linear buckling theory (from Jones, 2006)

(b) Comparison with the predicted critical buckling load for the strut

Fig. 6.8 shows the horizontal displacement at the end of a fixed-free strut for as a function of the applied downward load for different rod geometries (as indicated). As expected, a reasonably clear buckling point is observed in each case, where the rod experiences an abrupt alteration in its mode of deformation from simple uniaxial compression to bending. The applied load at this critical point can be determined and equated with the critical buckling load from the theory of Section 6.1.

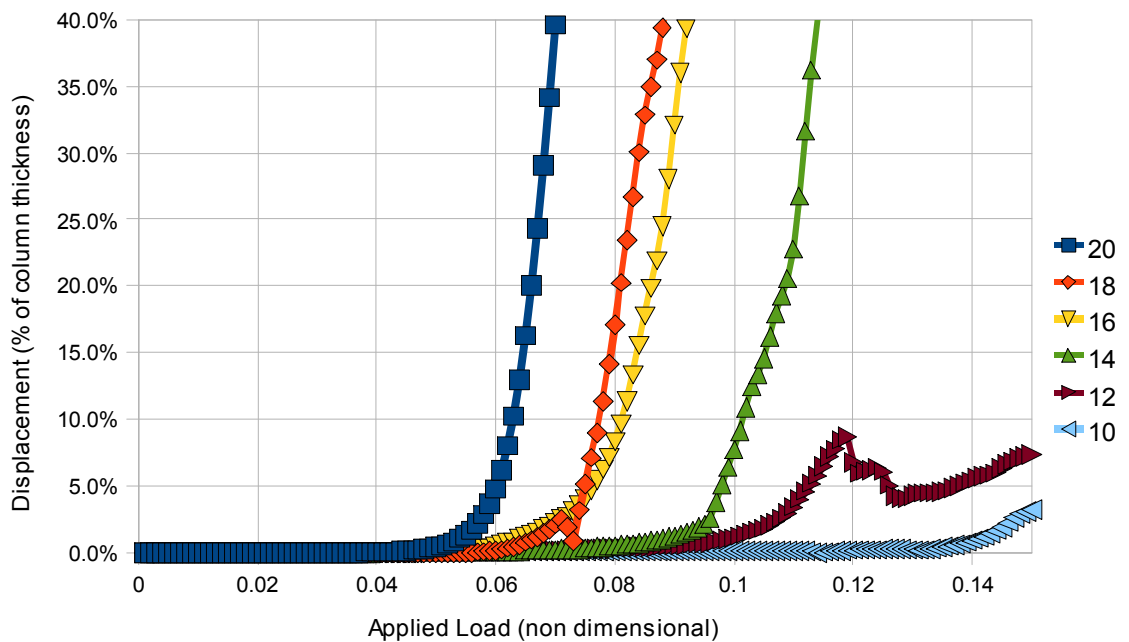


Fig 6.8 : The horizontal displacement as a function of applied load for a fixed-free strut demonstrates the critical load for the onset of buckling.

For a beam of rectangular cross-section, of thickness t and unit depth out of the plane, the cross-sectional area is $A = t$ and the relevant second moment of area is

$I = t^3/12$. If we express the critical buckling loads of (6.9) and (6.12) as a critical

buckling stress σ_{crit} then we can write

$$\sigma_{crit} = \frac{\bar{P}}{A} = \frac{\alpha\pi^2 Et^2}{12L^2} = \frac{\alpha\pi^2 E}{\lambda^2} \quad (6.14)$$

where $\alpha = 4$ for fixed-fixed end conditions and $\alpha = 1/4$ for fixed-free end conditions.

Clearly, if this critical buckling stress is greater than the yield stress of a material then the material will most likely fail due to other means. Hence the assumptions associated with Euler columns require rods to be considerably longer than thick. The slenderness ratio, λ , given by

$$\lambda = L / r \tag{6.15}$$

where $r = t / 2\sqrt{3}$ in this context is the smallest radius of gyration of the column cross-section and L the unsupported length of the column. The radius of gyration is a representation of the distance that the cross-sectional area, A, is from the bending moment. Hence different shapes, such as an I-beam can dramatically increase the critical buckling load. In relation to the area moment of inertia $I = A \cdot r^2$

In this form (6.14) shows that the slenderness ratio is inverse square proportional to the buckling stress, and this stress will reduce to zero as the slenderness ratio increases towards infinity. The critical buckling loads determined from Fig. 6.8 for fixed-free SPH struts with varying slenderness ratios are shown in fig. 6.9 and compared with the predictions of equation (6.14).

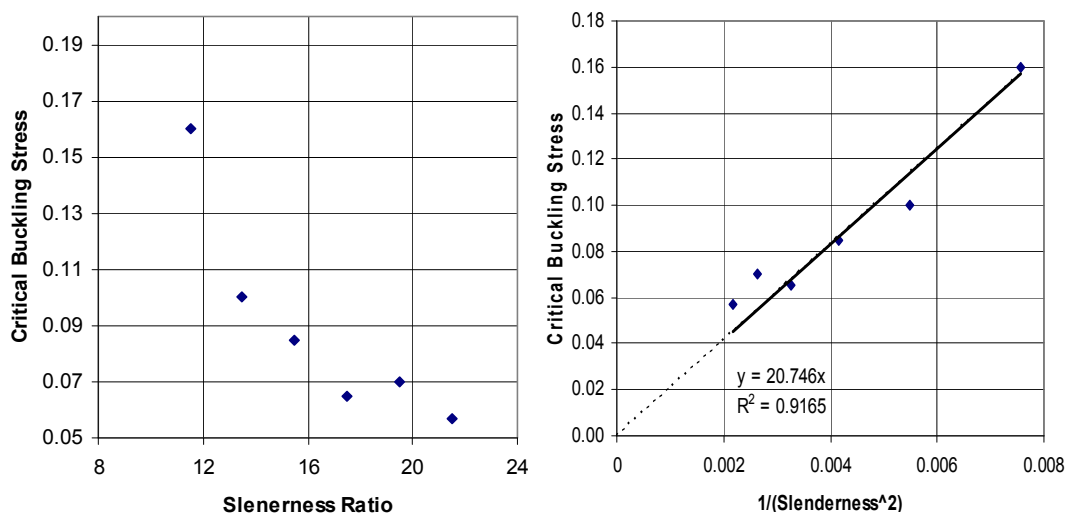


Fig.6.9.a) Critical buckling stress determined from SPH sims as a function of the strut aspect ratio. b) inverse square relationship (right).

The data is not completely smooth, as errors are caused by the noise inherent in the dynamic nature of the simulations and the point of the onset of buckling is not always precisely defined. This makes it difficult to exactly compare buckling loads to the values defined by the Euler analysis, although Fig 6.9b shows that the inverse square relationship is followed reasonably well. As discussed in the introduction to this chapter, the thickness of a rod made from SPH particles is difficult to define. As previously discussed SPH particles do not have strongly defined edges but a diffuse fuzzy surface described by the kernel. However, using the results from Fig. 6.9b it is possible to allocate an effective thickness to the SPH particles. The slope is $\alpha\pi^2 E$ which for unit modulus equates to 29.6. The slope determined from the SPH simulations is 20.746. This indicates that $29.6(t_{eff})^2 = 20.746t^2$, where t_{eff} is the effective thickness of the strut in relation to its bending stiffness (as opposed to its measured thickness in terms of particle number t). Thus $t_{eff} = 0.83t$, such that the effective thickness is actually smaller than the number of particles that constitute its thickness. This is not surprising, as only particles in the very centre of the strut with a full complement of neighbours within the range of the kernel respond according to the expectations of the fully-dense solid. The near surface particles, which constitute almost all the atoms within struts of narrow thickness, do not experience this full interaction and hence contribute less to the bending resistance of the strut than the others. One would expect that the effective thickness would tend towards the actual thickness in the limit of using a very high resolution of particles through the thickness of the strut, as the effect of the surface particles is reduced. However, this would make the SPH algorithm too computationally demanding and is not a reasonable proposition within this context. The observation that the struts respond in a manner that is more typical of a somewhat slimmer strut is useful in anticipating

and modelling the response of more complex structures in later sections.

6.4.Summary

In conclusion, the SPH model has been found to represent a sufficiently accurate means for the simulation of buckling in struts. Although comparison with Euler's buckling theory are not exact, this is not seen to be a limitation. In a physically realistic setting, the actual onset of buckling is very sensitive to the details of the specific rod and boundary conditions, and a reasonable amount of experimental scatter is expected. Given this, the advantageous nature of the SPH algorithm is expected to be suitably beneficial in the study of more complex buckling situations, where more complex interactions and large deformations result. It has been found that the diffuse nature of the SPH surface means that the effective bending thickness of the struts is roughly 17% less than the actual thickness determined from the number of particles. However, remarkably, the deformation in the struts is quite reasonably represented for struts of only a few particles in thickness. It has been shown that there is an dispersion viscosity induced in the simulation when considering the rotation of bodies beyond about 90° (see Section 3.4). As this is the limit of rotation for struts in this context, the large deformation model is expected and found to be valid here.

Thermal Barrier Coatings



7.1 Introduction

Thermal Barrier Coatings (TBC) have become increasingly important for engineering of materials which are required to withstand high temperatures. The most prevalent example is in the aeronautics industry where the turbine blades found in modern jet engines have to withstand extremes of temperature and extremely low failure rates. In order to deliver the increasing demands for fuel efficiency and improved performance, the gas temperatures inside the engine have risen to the point that active cooling of the turbine blades is no longer sufficient to prevent significant levels of hot corrosion and oxidation. Each blade must be able to withstand any damage that could be caused by tiny particulates caught in the gas stream if it is to remain in service for long periods of time.

The modern turbine blade consists of a base metal, frequently a nickel alloy, which is cooled from the inside via a chamber that runs the length of the blade. Even with this active cooling the blade needs protection from the hot combustion gases that flow past the blades. It has been common for the blades to be coated in exotic materials for many years, but in the search to develop better blades that withstand hotter temperatures for longer new multilayer coatings have been employed. These coating systems are able to reduce the temperature reaching the blade substrate by 170°C.

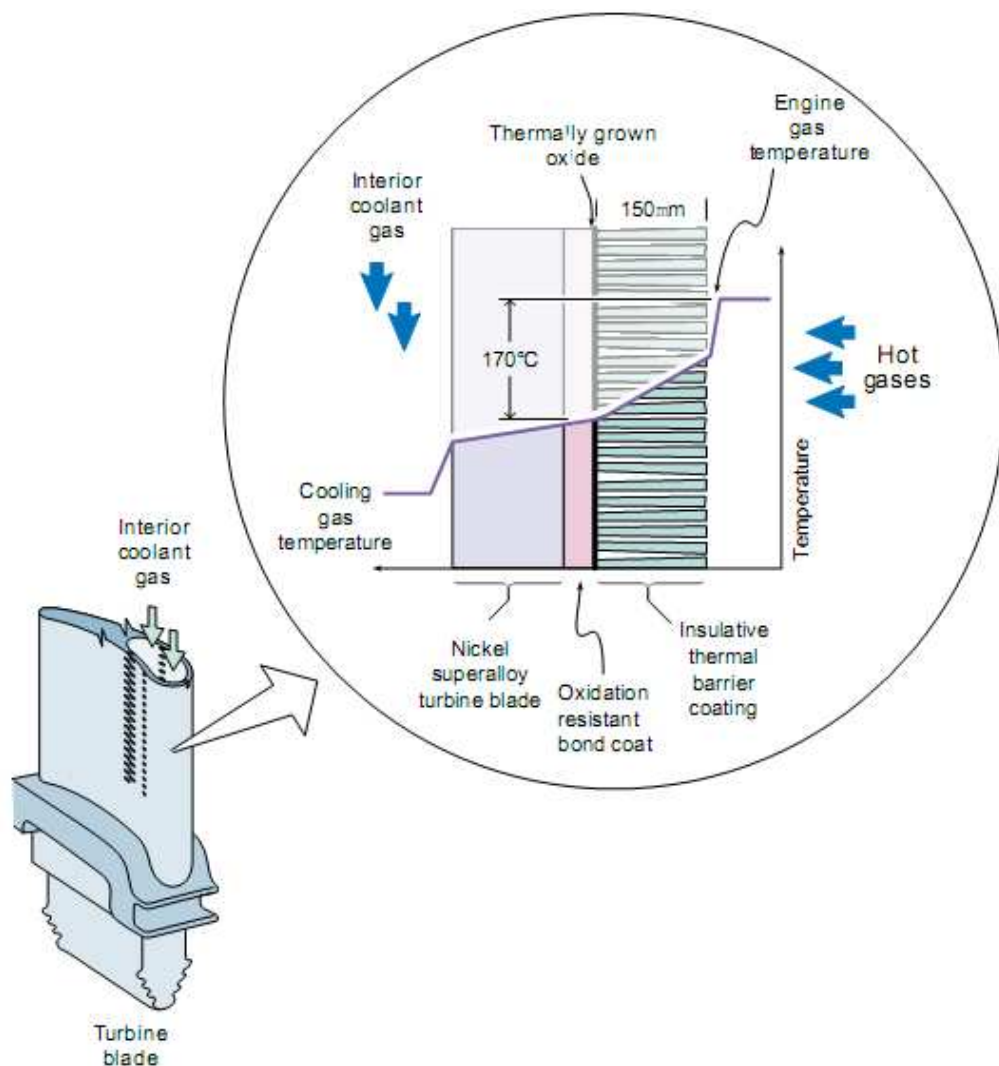


Fig.7.1. Diagram of a thermal barrier coated turbine blade (from Hass, 2000).

The top most layer of the coating system is where the most of the temperature drop occurs. It must be able to cope with this temperature differential without placing adverse mechanical strain upon itself or the underlying layers. Because of this it is preferentially porous allowing a different thermal expansion to the rest of the system. Being the outermost layer it must also be able to withstand the impact of high velocity micro particulates that are present in the hot gas stream.

The current preferred material is a vapour deposited layer of yttria stabilized zirconia. This ceramic offers good insulating properties with a low thermal conductivity, and due to the method of coating deposits itself in a columnar formation, as shown in Fig 7.1, allowing thermal expansion without stressing the rest of the system. The potential issue in the use of this porous microstructure is in its ability to resist damage from foreign objects. In a worse case scenario the columns could break free and begin to further damage the coating.

Each column is not a uniform structure but contains many micro pores along its surface as shown in Fig.7.2. The size, shape and morphology can be controlled to an extent by the electron beam physical vapour deposition process. This allows the coating to be designed to meet thermal and damage resistant criteria, see (Schulz et al.1996) and references therein for further details.

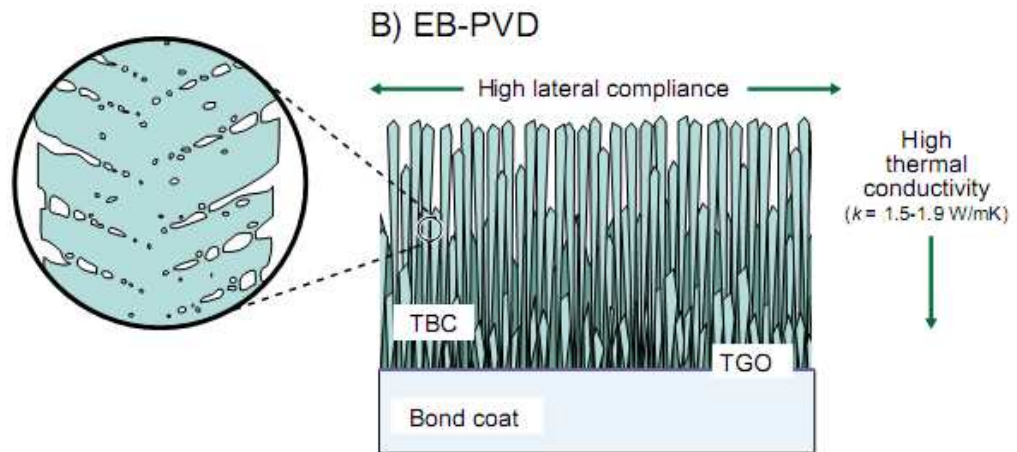


Fig.7.2 : Microstructural details of electron beam physical vapour deposited TBC
(from Hass, 2000)

A typical deformation mode in a TBC columnar structure subject to impact normal to the surface is shown in Fig.7.3. It is clear that the initial response is due to buckling of the column, which interact to roughly form a 45 degree buckling line across the sample reminiscent of a typical shear band type deformation in a homogeneous solid.

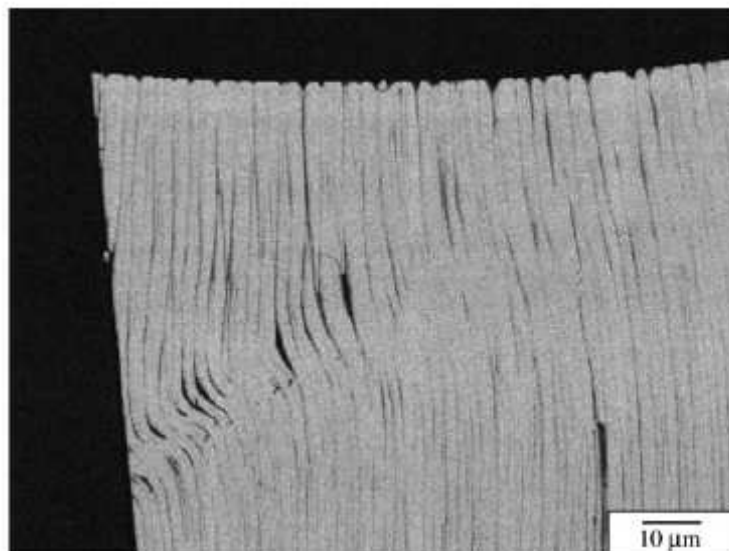


Fig.7.3 : Buckling deformation mode in a TBC structure subject to a normal impact
(Chen, Hutchinson & Evans, 2004)

Analysis of this problem is complex. The TBC columns behave like slender struts which buckle, but under the constraint of the neighbouring columns. They can undergo frictional contact, large deformations, failure and plasticity. It has been shown in Section 5.3 that the SPH algorithm is not readily amenable to the modelling of the growth of a single crack, so the simulations are not taken through to the point of complete failure and break-up of the TBC. However, the other processes are readily incorporated into the SPH simulation using the techniques described in the previous sections. The rest of this chapter is devoted to the description and analysis of SPH simulations of TBCs.

7. 2 SPH simulation of TBCs

Indentation tests of thermal barrier coatings are regularly used to evaluate the hardness and plastic response of TBCs by studying the load-unload characteristics. The same process is simulated using SPH, by generating a series of columns similar to the fixed-free rods simulated in the buckling analysis of the previous chapter. This setup removes the complexities of the substrate and concentrates purely on modelling the column structures. Allowing the columns to buckle and interact with one another via the contact algorithm introduces highly non-linear effects which are difficult to model successfully using conventional methods. The effect of two important system parameters are modelled: the ratio of the size of the gaps between columns relative to the thickness of the columns, and the magnitude of the coefficient of friction between the columns as they slide over one another.

For the purposes of this analysis, the benchmarking code of the previous chapters has been extended from two-dimensions to three-dimensions (3D). A cross-section through the initially regular 3D geometry of the computer simulation is shown in Fig. 7.3. The indenter is taken to have a radius R , the columns have a thickness t , the gaps between the columns is taken to be w . The material parameters are non-dimensionalised such that the Young's modulus is taken to be unity, the Poisson ratio to be 0.3, and μ represents the coefficient of friction between columns. The columns are rigidly constrained at their bases such that the effect of any deformation of the underlying substrate is neglected. The lateral boundaries are assumed to be unconstrained. This gives the TBC additional freedom to deform laterally so the indentation pressure can be assumed to be somewhat lower than that which would occur in a more highly constrained TBC.

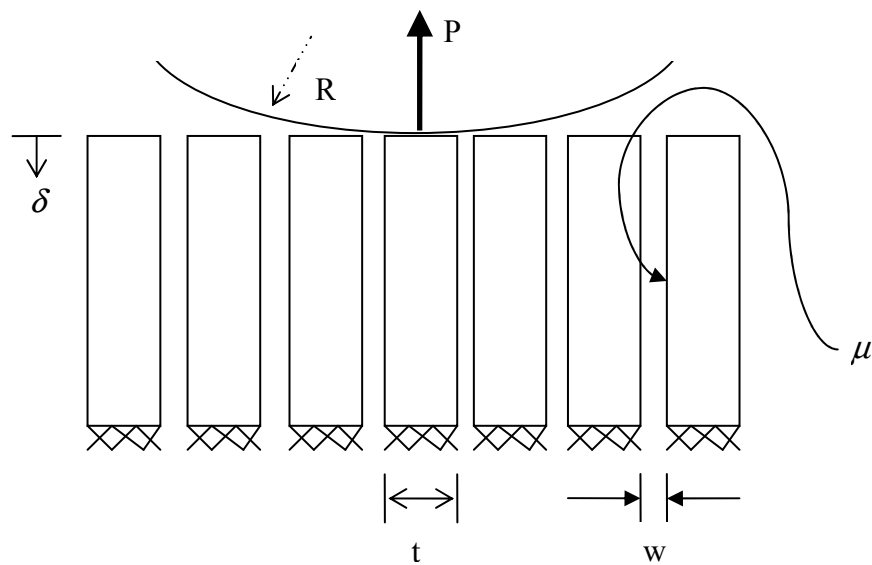
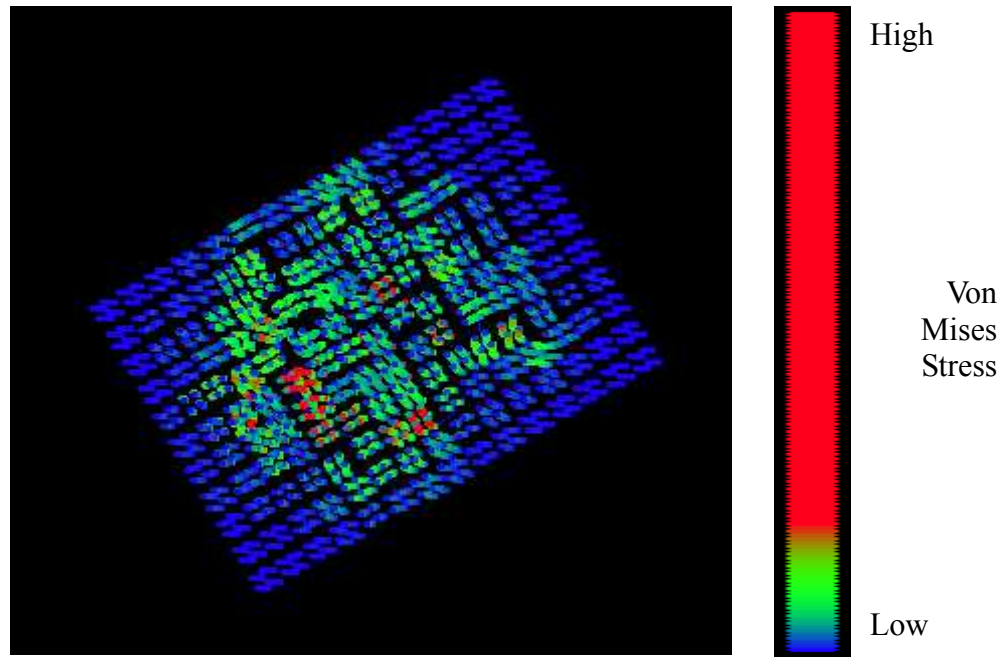


Fig.7.3. geometry of the SPH simulations of TBCs

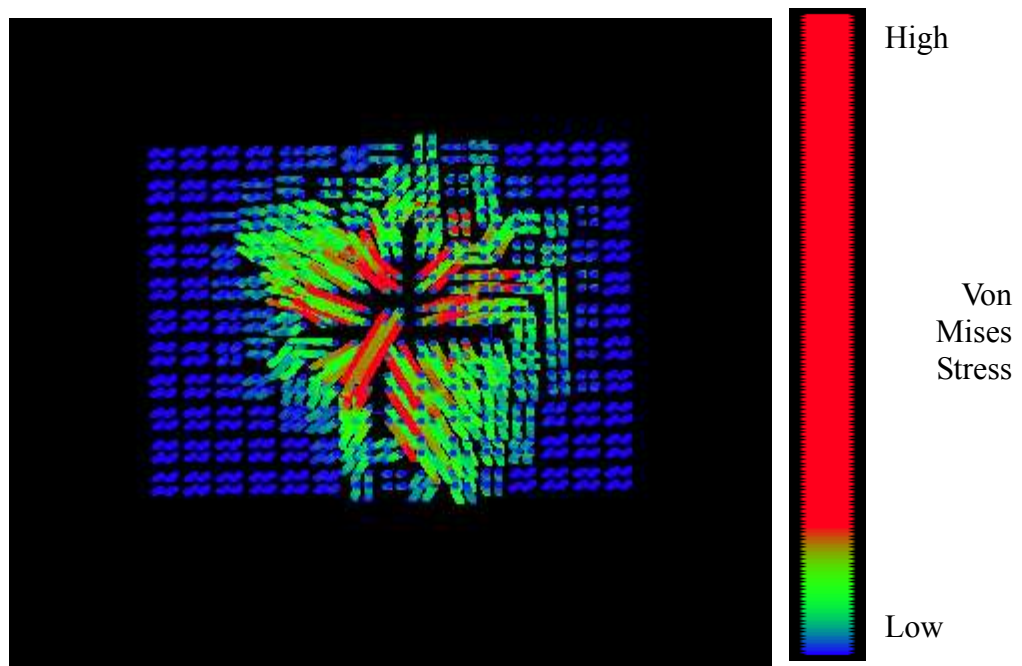
The actual number of columns that can be simulated depends of the computer resources available. In order to speed the process the indenter is chosen to be sphere of radius equal to 10 column widths. In reality for most testing procedures the indenter will be far larger and may make contact with up to 2000 columns in 3D. Even with the relatively low number of columns presented here simulation can still take many CPU hours to complete a full load and unloading cycle. Hence it is accepted that a full simulation of thousands of very long, thin columns, such as those shown in Fig. 7.3, will not be computationally feasible. However, it is expected that, whilst quantitative comparison with experimental results will not be possible, a qualitative insight into the effects of various geometric and material parameters will be obtained.

7.2.1. Deformation mechanism

Some typical snapshot images from a 3D SPH simulation of a TBC subject to a spherical indenter are shown in Fig 7.4. For 3D simulations, visualisation of the results becomes more difficult, although it is still possible to see the interactions between the columns in the plan views, and overall the response of the system looks physically realistic. The effect of the lack of lateral constraint is seen to be not too much of an issue, as even in the later stages of the loading sequence, Fig. 7.4b shows that the deformation of the columns are well contained by the surrounding pieces well beyond the buckling limit of the central columns.

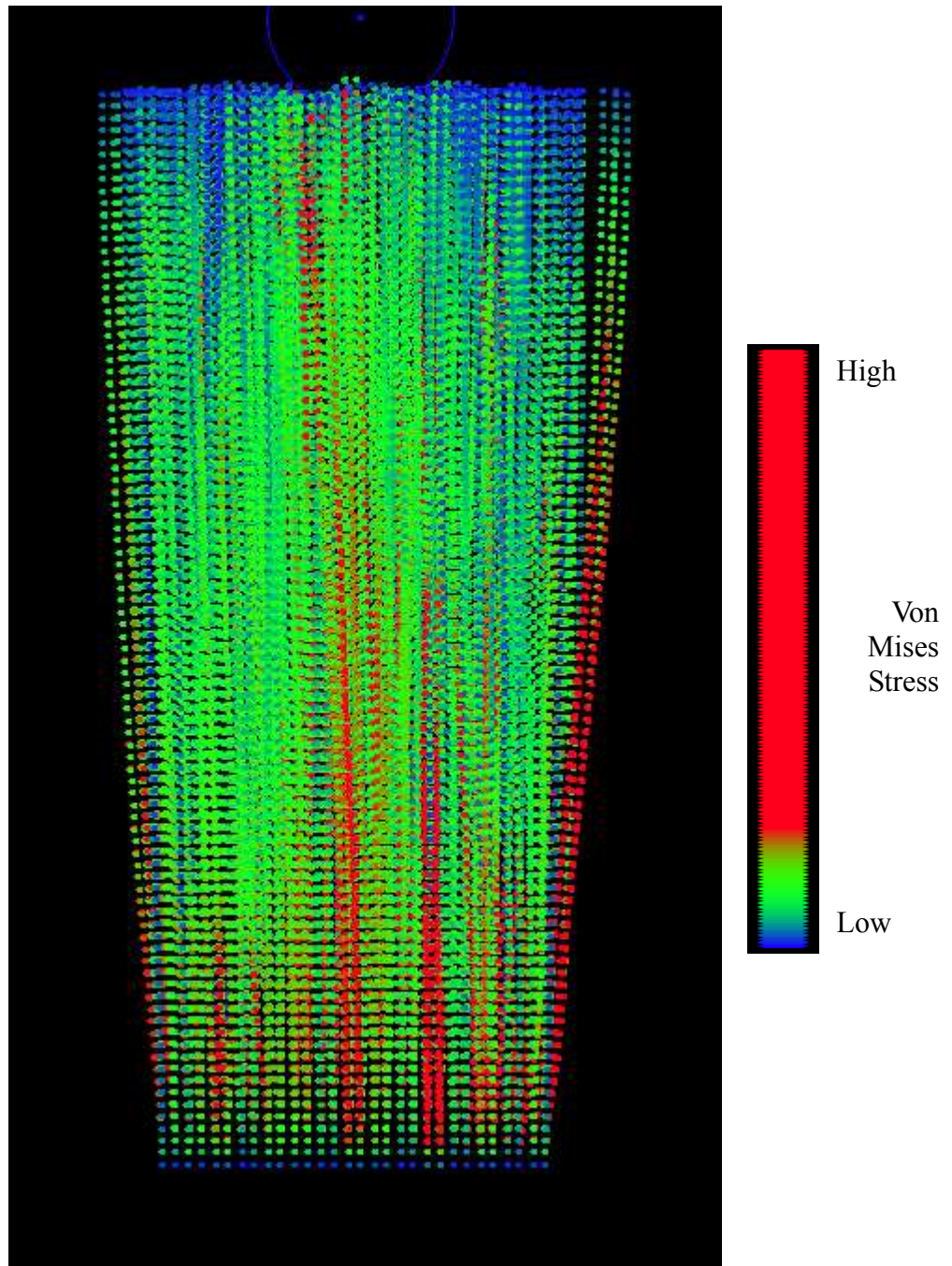


(a)



(b)

Fig. 7.4: snapshots of a 3D SPH simulation of TBCs for a square array of 11x15 struts. (a) plan view of the TBC during early stages of the indentation, (b) plan view of the TBC during maximum penetration of indenter

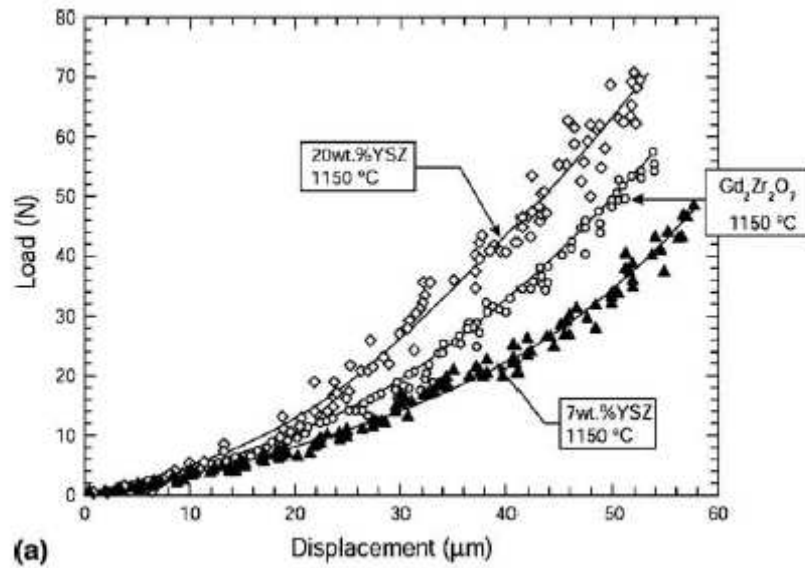


(c)

Fig.7.4, (c) the side view showing all the SPH particles is difficult to interpret in detail but it is clear from the general response that the struts are buckling in a physical manner away from the indentation point at the centre.

7.2.2. Force-displacement curves

Fig. 7.5a shows the loading and unloading force-displacement curve for a displacement controlled spherical indenter upon a sample with a gap ratio of $w/t = 0.01$ and inter-columnar friction coefficient $\mu = 0$. The oscillations apparent in both the loading phase after indentation of 3 particle spacings and throughout the unloading phase is unlike the smooth load-unloading witnessed for homogeneous blocks. These oscillations correspond to the initiation of a sequence of multiple buckling events in the TBC columns. The unloading curve follows the loading curve, indicating that the indentation is purely elastic with no internal dissipation, as expected. The oscillations in the unloading curve are expected to be due to the development of near-resonant vibrations in the interacting columnar structure in the later stages. Overall, the total indentation load is between 50% to 90% less than that witnessed with a solid block. The return to zero indentation force suggests, that the contact algorithm between the indenter and the TBC particles is functioning appropriately.



Displacement Controlled Indentation Test
(Column Structure 1% Gap)

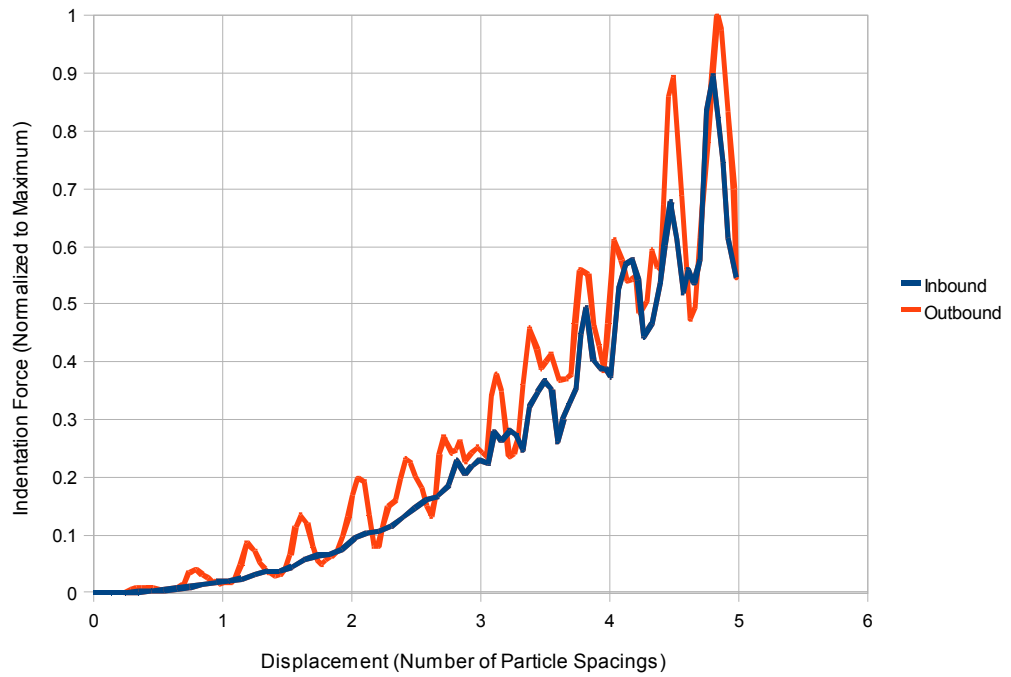


Fig.7.5: Examples of a typical force-displacement curve obtained from (a) experimental results for loading (no unloading) of a number of different commercial TBCs (Chen, Hutchinson and Evans, 2004), and b) SPH simulation of the indentation loading/unloading sequence on a TBC without inter-columnar friction

Fig 7.5b shows three typical loading force-displacement curves for different TBCs (Chen et al. 2004). The shape of the curve is very similar to the SPH simulation result of Fig. 7.5a, except for the lack of large oscillations in the data. This is expected, as the real TBC will contain thousands of columns, and hence the buckling of a single column will not significantly affect the overall indentation force (although there is significant noise in the data of Fig 7.5b which would not be expected for the indentation of a homogenous solid and could therefore be indicative of the initiation of a succession of lesser buckling events). The apparent increase in energy during the unloading process results from similar vibrations rising the internal energy of the system as a whole.

7.2.3. Effect of material and geometric parameters

Further SPH simulations have been conducted to investigate the effect of the TBC geometry and friction. In these cases, the maximum indenter displacement is restricted to 3 particle spacings to reduce errors. Firstly, the effect of changing the gap spacings is investigated for a coefficient of friction of $\mu=0$. The results are plotted in Fig. 7.6. In this case, the maximum indentation load at which the indentation depth reaches one column width is analysed. As the gap ratio increases, the load required drops considerably, reducing the hardness of the TBC system and consequently its ability to resist damage. This is because increasing the gap size reduces the extent of the lateral constraint on the columns.

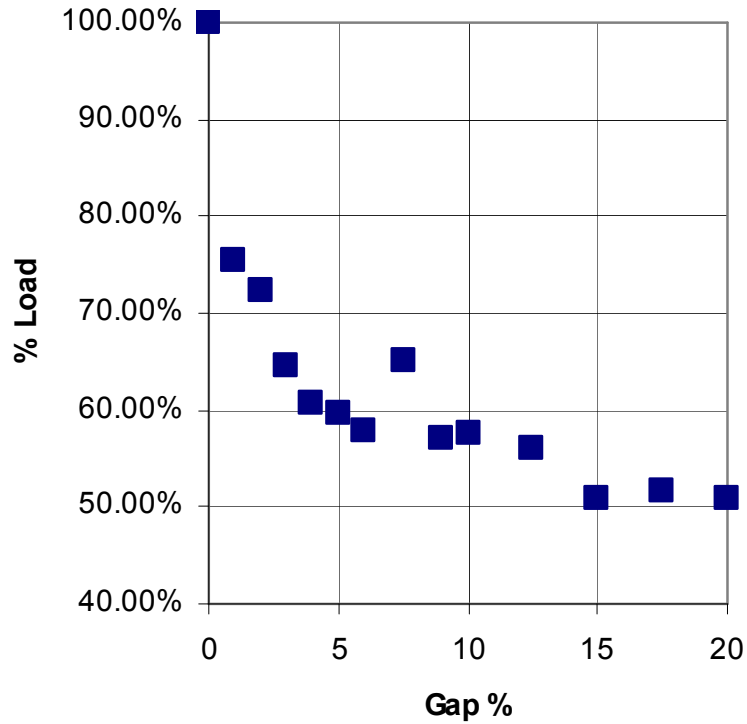


Fig. 7.6: change in the maximum indentation load with gap spacing between the TBC columns.

Introducing inter-columnar friction results in the load-unload situation in Fig. 7.7, for a coefficient of friction of $\mu = 0.2$ and a gap-spacing ratio of 1%. The general feature of the shape of this curve, in comparison to the zero friction case of Fig. 7.5a, is that the oscillations are considerably reduced due to the internal frictional dissipation.

Displacement Controlled Indentation Test

(Column, Gap 1%, Co-Friction 0.2)

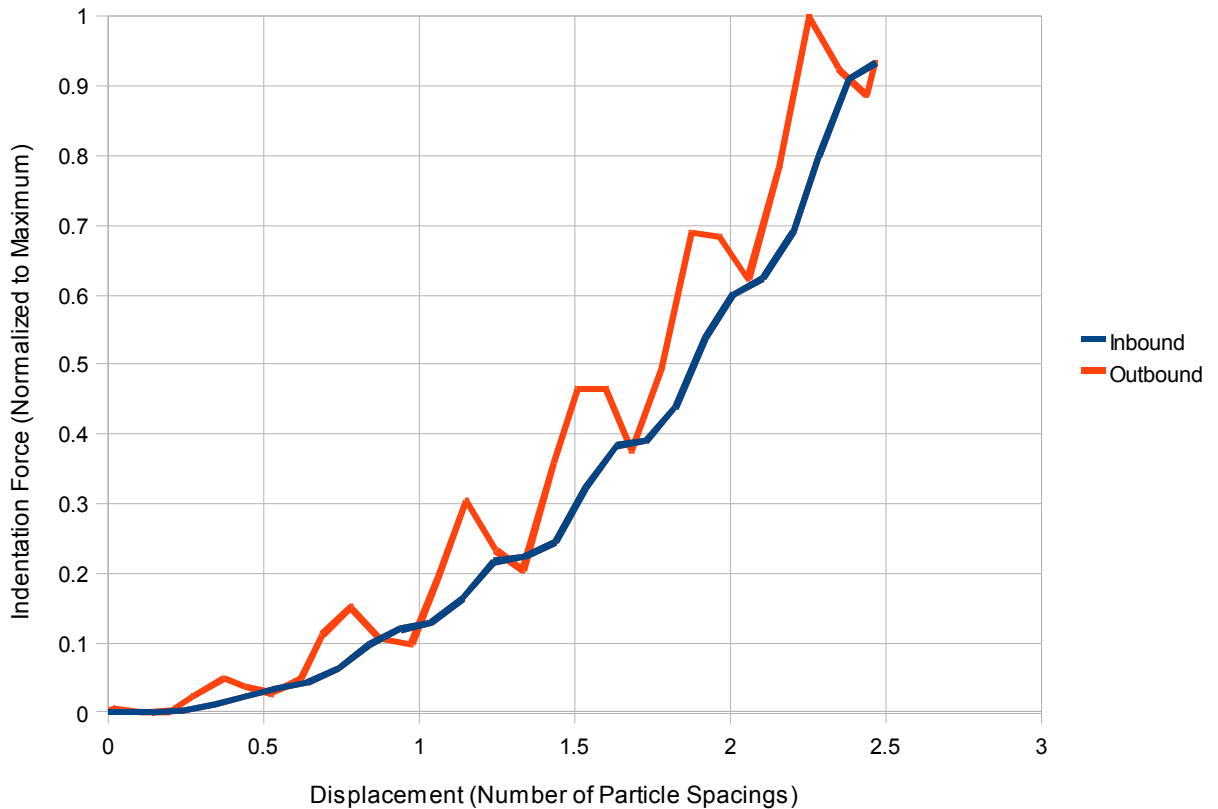


Fig. 7.7: Example of a typical force-displacement curve obtained from a SPH simulation of the indentation loading/unloading sequence on a TBC with an inter-columnar friction coefficient of $\mu = 0.2$.

Fig. 7.8 illustrates how the load required to reach a depth of one column width varies as the coefficient of friction increases. As expected, the indentation load increases with friction, but beyond a certain point noise begins to distort the results and very high coefficients of friction have the effect of sticking the columns together. However, the general trend is clear, especially in the physically realistic friction coefficient regime of $0 < \mu < 0.4$. The response is intuitively correct, as one would expect an increase in frictional dissipation between the columns to increase the resistance of the system to deformation.

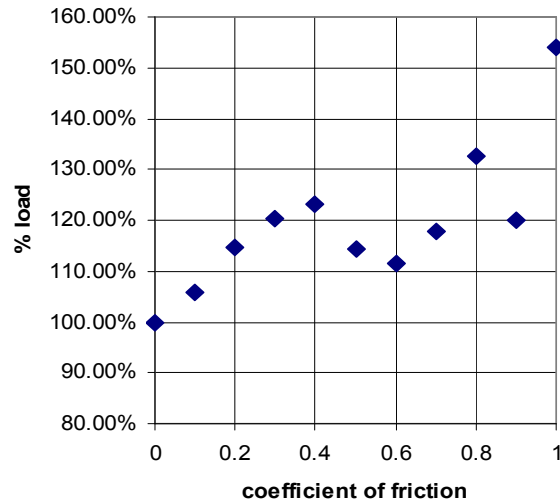


Fig.7.8: Variation in the maximum indentation load on a TBC as a function of the inter-columnar friction coefficient μ .

7.3. Summary

In conclusion, SPH has proven to be a suitable simulation technique for the analysis of this problem. Although restricted by the computational extent and geometry of the system, as with any other simulation method, some useful results have been obtained. The effect of the gap spacing and the inter-columnar friction coefficient have both been shown to be significant factors in determining the hardness of TBCs. Increasing the gap spacing, it has been shown that it is possible to decrease the indentation load by up to 50%. Within the physically realistic range of friction coefficients, the effect of increasing the inter-columnar friction has been demonstrated to increase the indentation load by up to 25%.

Conclusions

8

8.1. General Observations

Working with Smooth Particle Hydrodynamics it is relatively easy to produce results that mimic the real world. As shown in previous chapters, the basic functions of the technique fulfil the basic requirements of the physical model. Linear momentum conservation naturally occurs via the pairing of particles and the symmetry of the kernel. Errors do occur due to the kernel estimation process, most particularly near edges where even linear functions are not precisely matched. Although difficult to obtain exact values, errors tend not to compound and general accuracy remains high.

Making alterations (or adding) to the basic SPH governing equations to improve functionality of the simulations is not quite as simple as it first appears. In order to add physics, such as plasticity Section 5.2 or thermal conductivity a new equation of state (EOS) is required that fits inside the established frame work; pair wise symmetry should be maintained for example. SPH is fairly robust at handling

sensibly defined EOS allowing a hydrodynamic code to simulate a wide variety of fields from the inertia of stars to elastic solids.

8.2. Adaptations

When attempting to modify other areas of SPH, such as the ability to handle interactions across boundaries, it is necessary to compliment the smoothing function. The kernel is the basic unit functional element. Attempt to interact with individual particles without mediating through the kernel is dangerous and opens up the risk of instabilities forming. The properties of a single particle are not well defined within the SPH framework. It is only the interactions by the kernel with fellow neighbouring particles that resolves the physical properties. All physical properties are interpolated over the spatial dimensions of the particles, hence are not exactly represented at the particle location, but are only correct over the kernels dimensions. One is able to use spatial dimensions of the particles to infer new properties. Not necessarily the instantaneous velocity, stress, pressure, etc. represented by that particle; which is only an interpolation of a much larger feature of the simulation.

The XSPH addition is a prime example of where stability can be improved by utilising the entire range of the kernel. XSPH generates a group velocity based upon surrounding particles using this kernel weighted velocity instead of relying purely on the standard velocity interpolation. The improvements to particle stability not only aids the particle map from becoming disordered, it has the knock on effect of making future interpolation results more accurate by maintaining regular particle spacing. XSPH does have some problems associated with it; the relatively large smoothing

length means that the resolution of the velocity field is low and issues and it is at least partially responsible for poor angular momentum conservation.

Design decisions must be made to ensure that SPH simulations meet the requirements of the model. If angular momentum conservation is important then XSPH must be switched off. Similarly parameters such as the Grady-Kipp damage model need to be carefully chosen to ensure accurate results. The contact model represented here is designed to be a generic formulation. Various forms of the penetration algorithm are available for high speed, low speed, large compliance or hard body simulations at the current time it appears trial and error is the only reliable method of selecting the best formulation for situations where the design considerations are not so clear cut.

8.3. Complete Lagrangian Method

More critical is the lack of rigorous angular momentum conservation for rigid body rotations. The Lagrangian nature of SPH means objects are free to deform and individual particles are not restrained from rotating about their own axis. It is suggested by Dilts (1999) that exact solutions to equations of the first order improves conservation of properties. Both linear and higher order completeness can be achieved through adaptations to the kernel. However, the greater the constraints on particles, the more degrees of freedom are lost. With tight control over rotation you lose much of the malleability, and with changes of geometry being the main advantage of mesh-free methods the consequence of high precision is accompanied

by loss of ability to model highly deformable structures.

Recent research, collated together in a paper by Liu and Liu, 2010 has suggested that many of the problems associated with the lack of precision, in particular the tensile instability, are due to the combination of a Lagrangian technique with an Eulerian kernel. In other-words although a set of material co-ordinates are used, the kernel is still based on the spatial geometry, unaffected by material deformation. Adaptive h and corrective kernels do apply underlying material co-ordinates to improve the technique, but a far more radical approach is to link the kernel completely to the material frame of reference, as illustrated in Fig.8.1. This generates a true Lagrangian kernel which is said to better improve SPH as it is now completely Lagrangian.

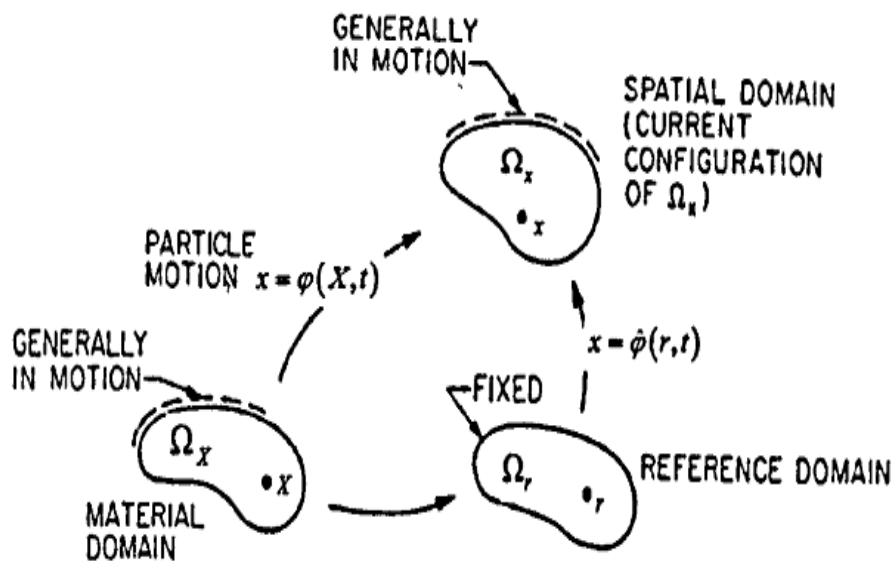


Fig.8.1. Lagrangian domains from Hughes, Liu, Zimmermann, 1989.

In this true Lagrangian scheme the kernel is linked to a set of material points. Any deformation of the underlying material and the Lagrangian kernel adapts with it. No new particles enter or leave the kernel range; it is always around the same set of material points. At first glance, the computational expense of such deformation

seems very high and it requires complex deformation parameters, essentially generating a new kernel for every single particle. But the consequence of no new particle interactions, being created by particles entering or leaving the kernel range, means that nearest neighbour analysis is no longer required; saving considerable computational overheads. Perhaps the biggest problem with this technique occurs in situations with high deformation. The kernel will become extremely distorted and intertwined with other kernels. Again, this technique sacrifices some of the benefits of mesh-free methods in that deformations may become restrained. Although in the case of solid materials extremely large deformations are rare, this technique, or a hybrid approach, could become the de-facto standard for future solid body SPH simulations.

8.4. A multi-CPU approach

A common concern of all dynamic modelling techniques is the length of time required to run large scale simulations. Specific optimizations are best placed in the main iterative loops, as this is where the computer spends most of the resources. Past designers of hydrodynamic SPH, such as Hernquist and Katz, 1989, codes have spent most effort in optimizing the nearest neighbour updates. This is such a computationally intensive and common problem that dedicated hardware has been designed to take the load off general purpose CPUs, see Schumacher et al., 2009. Fortunately the particles in solid material simulations hardly move from their initial positions so fewer nearest neighbour updates are required. To account for vibrations and small rearrangements of particles a slightly larger neighbourhood range should be used to create an initial nearest neighbour list. For larger changes in geometry the

nearest neighbour list can be updated only every hundred or so iterations.

One of the key elements to a small kernel range is that particles do not interact over large distances. This has some disadvantages as a mathematically robust modeling technique, but it allows the four dimensional sample space to be split into a number of non-interacting parts. Interactions between these sections can only occur at the speed of sound, related the kernel size (or looking at it another way the initial packing density of the particles). It therefore becomes advantageous to split the workload of calculated particulate forces between several processors, combining the data only at the point of calculating the timestep. There are two distinct methods of parallelizing SPH allowing each processor to work on a portion of the available map space, or have multiple processors working together each dynamically assigned to a particular nearest neighbour. The latter solution requires shared memory space which is common on Massively-Multi-Processor systems found mainly in government institutions.

Multi box Cluster Systems do not have the luxury of shared memory access and in many cases this makes them harder to code for. The principle is that each processor must share its results with other processors via the relatively slow external interconnect. However SPH may split its map into minimally interacting subsections, the perfect application for such a distributed cluster system. Indeed taking the cluster idea to the extreme, distributed grid based networks via the Internet or an intranet mean that existing office computers can be put to work during idle periods, utilizing CPU cycles that would otherwise go wasted while Internet surfing or document writing. Spare processing power on modern Graphics Processing Units

are being used for scientific computing, Green (2007) demonstrate a particle based model using the CUDA programming language.

In principle a method is required that splits the sample map into domains, each of approximately equal CPU load, so that each domain thread finishes as close to the same time as possible thus reducing wait latency. This usually means that all domains must contain the same number of particles (or to be more accurate the same number of particle interactions), easy to achieve with the initially regular particle spacing found in solid material SPH. Advanced techniques of load balancing can be implemented by extending the size of the fastest finishing domain thread from that of slower neighbours.

A domain contains particles that it has updating control over and all of their nearest neighbours. These are stored in the local computers memory so as to cut down on the slow exchanges between nodes in the cluster. There must be communication between CPUs and this is usually governed by a master node which has the role of keeping track of changes, storing data and generating the initial conditions. If any particles move from one zone to another due to a velocity or by changing the domain size, information about these particles must be moved between CPUs. Small vibrations could lead to particles being swapped on a regular basis so particles should not be initially set on boundaries of domains so that there is room from small perturbations, see Fig.8.2. Every timestep the overlapping domain areas need to be exchanged so that all CPUs have an up to date local map. This setup creates fringe zones between domains that are held in more than one local computer at a time. In order to minimize time spent exchanging information about particles in the fringe the

surface area of domains should be kept as low as possible, using squares (or cubes in 3D) that easily tessellate and maximize volume to surface area, enhancing performance by keeping inter-processor communication down.

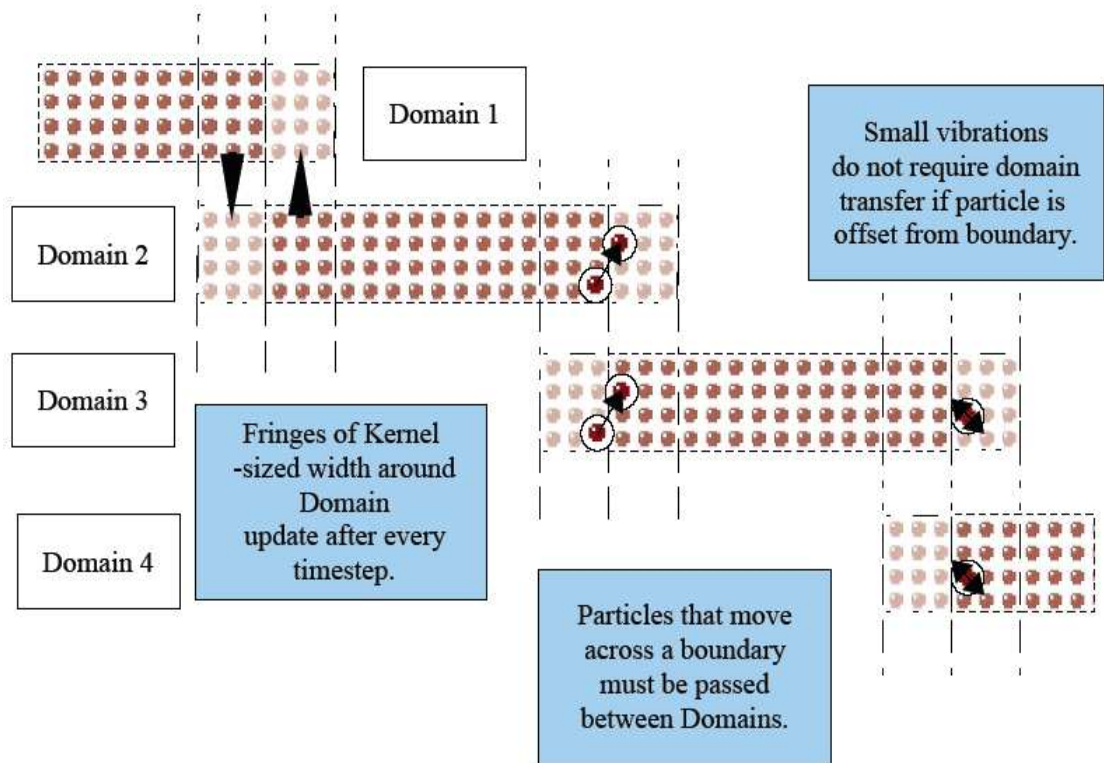


Fig.8.2. A multi-CPU design for SPH simulations

8.5. Future Applications

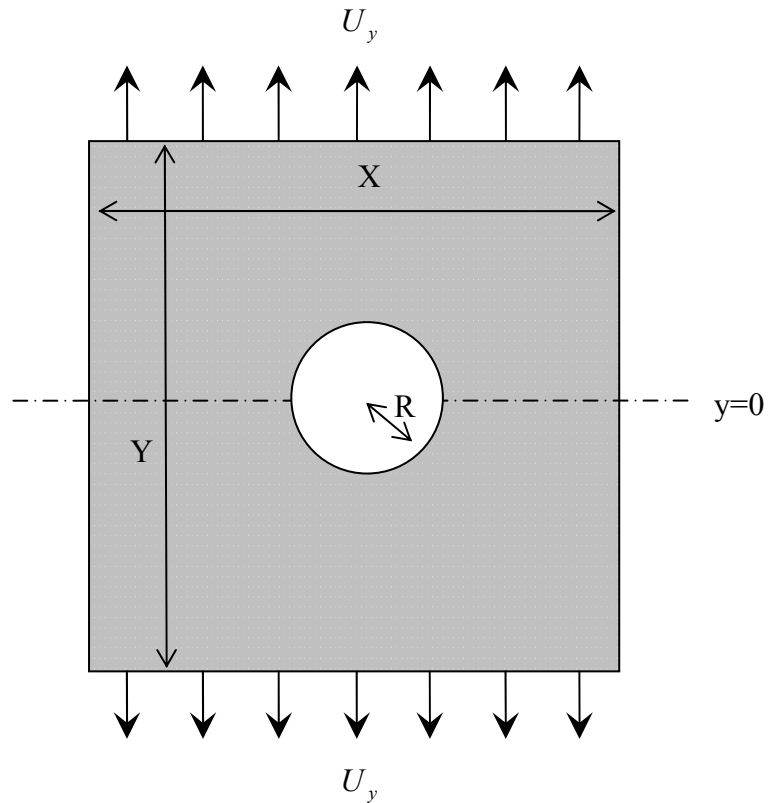
One particular area that is of increasing importance in the field of material science is that of surface coatings. A thin layer of composite material bonded to the surface of a substrate can increase environmental and wear resistance, and reduces or better controls friction and abrasion (often at a weight advantage to non coated materials) Hogmark et al. 2000. Various experimental methods exist in order to measure the properties of tribological coatings from (nano-)indenters Korsunsky et al. 1998 to scratch testers Bull, 1997. These (semi)destructive techniques require skilled analysis to predict what is happening to the coating, material and interface. No known computer modeling techniques exist to aid in the design and evaluation of coatings. An SPH application could fit this niche by offering 3D visualizations of coating damage with surface pileup and large geometry changes.

The full potential of Smooth Particle Hydrodynamics has not yet been explored. It can be implemented to model extremely complex systems and give reasonable approximations to dynamically evolving multi-physics problems that would be extremely difficult to model with traditional Finite Element Methods. SPH will never reproduce high precession details on the local scale, but when looking at the global scale it can deliver model predictions in a robust and accurate way.

Appendix A

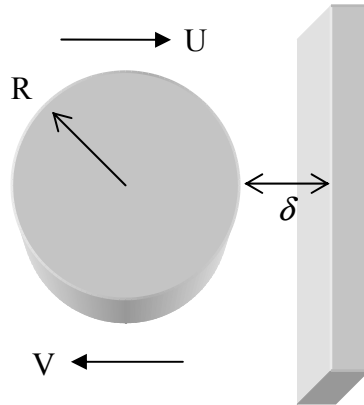
Simulation Setups

A.1. Quasi-static analysis of stress in a plate containing a circular hole (p.27)



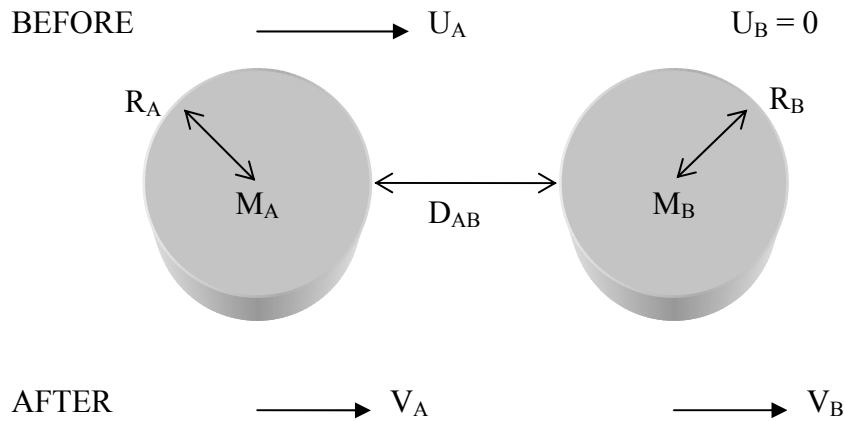
Property			Value
Total Domain (particles)		X	80
		Y	80
Centred Hole, Radius		R	10
Initial Velocity (particles/timestep)	Top Row (Constant)	U_y	0.001
	Bottom Row (Constant)	U_y	-0.001
Number of Particles		N	6090
Particle Mass		m_p	1.0
Density		ρ	1
Young's Modulus		E	1
Poisson's Ratio		ν	0.3
Speed of Sound (particles/timestep)	$c = \sqrt{\frac{E(1-\nu)}{\rho(1+\nu)(1-2\nu)}}$	c	1.16
Artificial Viscosity	See (2.60), p.24	α	1.0
XSPH	See (3.2), p.30	$\tilde{\epsilon}$	0.5
Tensile Instability	See (3.6), p.41	n	6

A.2. Interactions with Solid Wall (p.30)



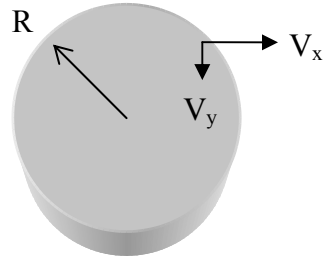
Property	(excluding fixed wall)		Value
Fixed Wall (particles)		X	5
		Y	30
'Ball'	Radius	R	12
Initial Velocities (particles/timestep)	'Ball'	U_x	0.1
Number of Particles	(excluding wall)	N	437
Particle Mass		m_p	1.0
Density		ρ	1
Young's Modulus		E	1
Poisson's Ratio		ν	0.3
Speed of Sound	$c = \sqrt{\frac{E(1-\nu)}{\rho(1+\nu)(1-2\nu)}}$	c	1.16
Artificial Viscosity	See (2.60), p.24	α	1.0
XSPH	See (3.2), p.30	$\tilde{\epsilon}$	0.0 (OFF) & 0.5
Tensile Instability	See (3.6), p.41	n	6

A.3. Conservation of Linear Momentum (p.33)



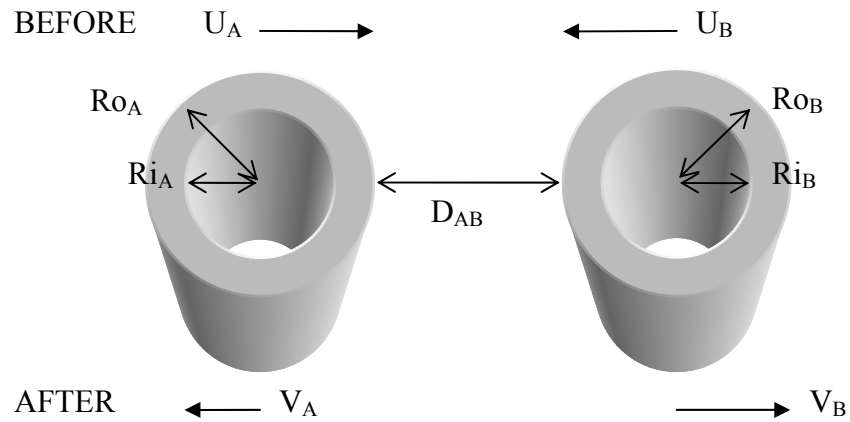
Property			'Ball' A	'Ball' B
'Balls'	Radius	R	12	12
Initial Velocities (particles/timestep)	'Ball'	U_x	0.01c 0.001c 0.0001c	0.0
Number of Particles		N	437	437
Particle Mass		m_p	1.0	0.1 to 0.6
Density		ρ	1	
Young's Modulus		E	1	
Poisson's Ratio		ν	0.3	
Speed of Sound	$c = \sqrt{\frac{E(1-\nu)}{\rho(1+\nu)(1-2\nu)}}$	c	1.16	
Artificial Viscosity	See (2.60), p.24	α	1.0	
XSPH	See (3.2), p.30	$\tilde{\epsilon}$	0.5	
Tensile Instability	See (3.6), p.41	n	6	

A.4. Conservation of Angular Momentum (p.36)



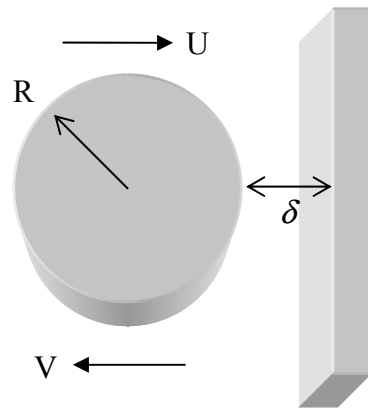
Property			'Ball'
'Ball'	Radius	R	12
Initial Velocities (particles/timestep)	'Ball'	V_x	$0.1(-v_y)$
		V_y	$0.1(v_x)$
Number of Particles		N	437
Particle Mass		m_p	1.0
Density		ρ	1
Young's Modulus		E	1
Poisson's Ratio		ν	0.3
Speed of Sound	$c = \sqrt{\frac{E(1-\nu)}{\rho(1+\nu)(1-2\nu)}}$	c	1.16
Artificial Viscosity	See (2.60), p.24	α	1.0
XSPH	See (3.2), p.30	$\tilde{\epsilon}$	0.0 (OFF) & 0.5
Tensile Instability	See (3.6), p.41	n	6

A.5. Colliding Rubber Rings and the Tensile Instability Correction (p.40)



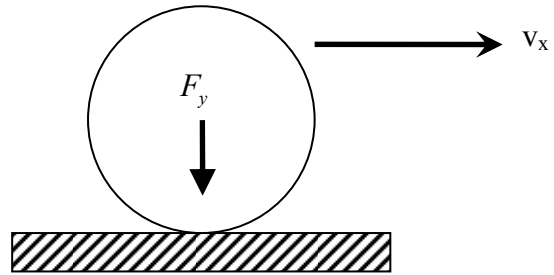
Property			'Cylinder' A	'Cylinder' B
'Cylinder'	Outer Radius	R_o	35	35
	Inner Radius	R_i	30	30
Initial Velocities (particles/timestep)	'Ball'	U_x	0.1	-0.1
Number of Particles		N	1018	1018
Particle Mass		m_p	1.0	
Density		ρ	1	
Young's Modulus		E	1	
Poisson's Ratio		ν	0.3	
Speed of Sound	$c = \sqrt{\frac{E(1-\nu)}{\rho(1+\nu)(1-2\nu)}}$	c	1.16	
Artificial Viscosity	See (2.60), p.24	α	1.0	
XSPH	See (3.2), p.30	$\tilde{\epsilon}$	0.5	
Tensile Instability	See (3.6), p.41	n	OFF	6

A.6. 'Ball Bounce' from Fixed Wall with Penalty Force (p.57)



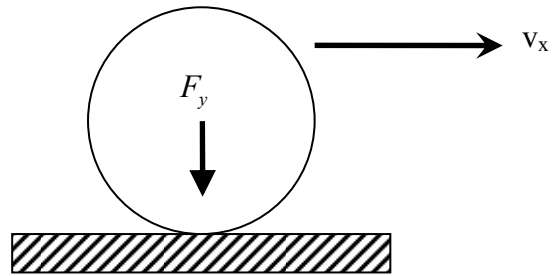
Property			Value
Fixed Wall (particles)	Particle Type A	X	5
		Y	30
'Ball'	Particle Type B Radius	R	10
Initial Velocities (particles/timestep)	'Ball'	U_x	$0.03c$
Number of Particles (excluding wall)		N	317
Particle Mass		m_p	1.0
Density		ρ	1
Young's Modulus		E	1
Poisson's Ratio		ν	0.3
Speed of Sound	$c = \sqrt{\frac{E(1-\nu)}{\rho(1+\nu)(1-2\nu)}}$	c	1.16
Artificial Viscosity	See (2.60), p.24	α	1.0
XSPH	See (3.2), p.30	$\tilde{\epsilon}$	0.5
Tensile Instability	See (3.6), p.41	n	6
Penalty Force		R_{contact}	NONE & 1.0

A.7. Friction (p.61)



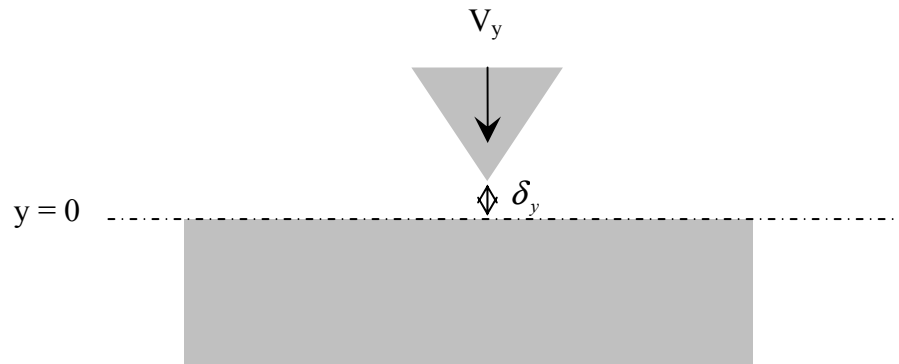
Property			Value
Fixed Surface (particles)	Particle Type A	X	36
		Y	5
‘Ball’	Particle Type B Radius	R	12
Initial Velocities (particles/timestep)	‘Ball’	v_x	0.0001c
Body Force		F_y	-0.01
Number of Particles	(excluding surface)	N	437
Particle Mass		m_p	1.0
Density		ρ	1
Young’s Modulus		E	1
Poisson’s Ratio		ν	0.3
Speed of Sound	$c = \sqrt{\frac{E(1-\nu)}{\rho(1+\nu)(1-2\nu)}}$	c	1.16
Artificial Viscosity	See (2.60), p.24	α	1.0
XSPH	See (3.2), p.30	$\tilde{\epsilon}$	0.5
Tensile Instability	See (3.6), p.41	n	6
Penalty Force		R_{contact}	NONE & 1.0
Coefficient of Friction		μ	NONE & 0.0 to 1.2

A.8. Rolling Contact (p.65)



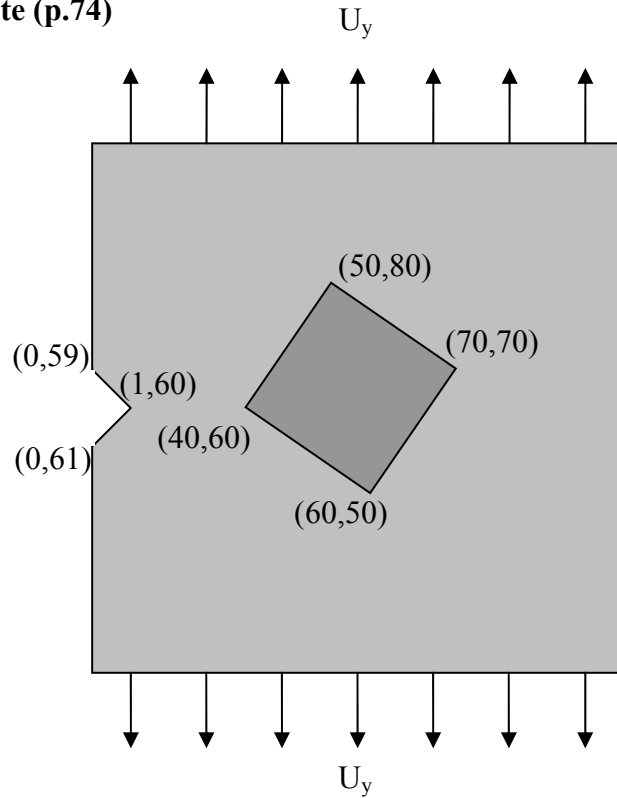
Property			Value
Fixed Surface (particles)	Particle Type A	X	36
		Y	5
‘Ball’	Particle Type B Radius	R	12
Initial Velocities (particles/timestep)	‘Ball’	v_x	0.0001c
Body Force		F_y	-0.01
Number of Particles	(excluding surface)	N	437
Particle Mass		m_p	1.0
Density		ρ	1
Young’s Modulus		E	1
Poisson’s Ratio		ν	0.3
Speed of Sound	$c = \sqrt{\frac{E(1-\nu)}{\rho(1+\nu)(1-2\nu)}}$	c	1.16
Artificial Viscosity	See (2.60), p.24	α	1.0
XSPH	See (3.2), p.30	$\tilde{\epsilon}$	0.0 (OFF)
Tensile Instability	See (3.6), p.41	n	6
Penalty Force		R_{contact}	1.0
Coefficient of Friction		μ	0.0 & 0.6

A.9. Indentation (p.69)



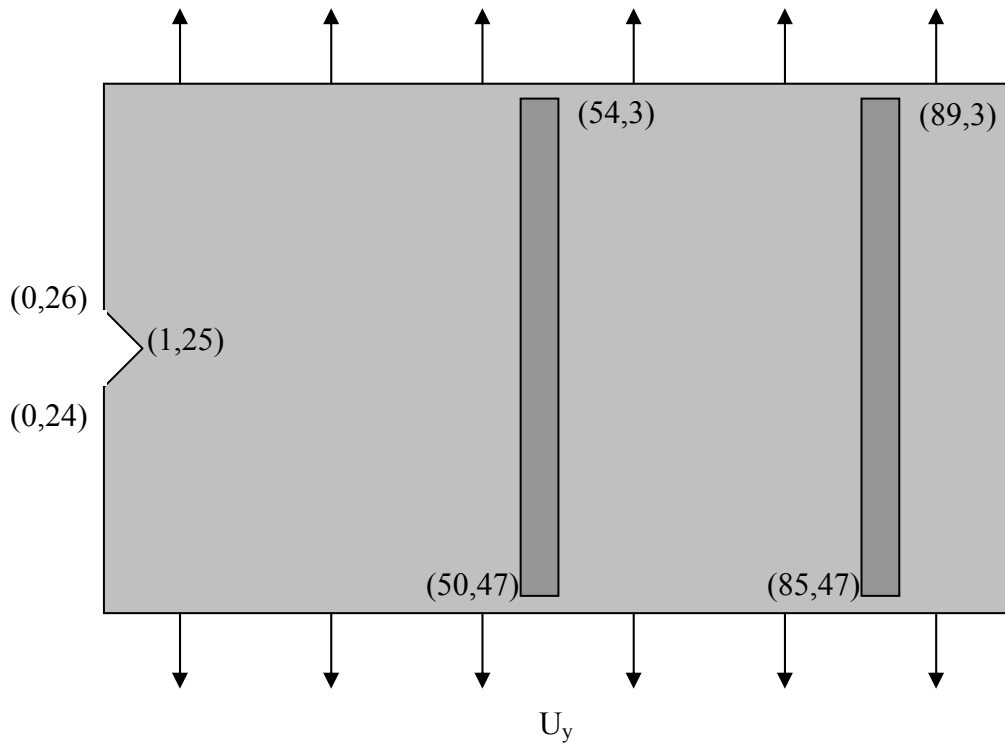
Property			Value
Fixed Surface (particles)	Particle Type A	X	50
		Y	20
Triangular Indenter	Particle Type B (1+3+5+7+9+11+13)	N_{tri}	49
Initial Velocities (particles/timestep)	Displacement Control (Constant Velocity)	V_y	-0.0001
	Bottom Row (Const.)	V_y	0.0
Particle Mass		m_p	1.0
Density		ρ	1
Young's Modulus		E	1
Poisson's Ratio		ν	0.3
Speed of Sound	$c = \sqrt{\frac{E(1-\nu)}{\rho(1+\nu)(1-2\nu)}}$	c	1.16
Artificial Viscosity	See (2.60), p.24	α	1.0
XSPH	See (3.2), p.30	$\tilde{\epsilon}$	0.5
Tensile Instability	See (3.6), p.41	n	6
Penalty Force		R_{contact}	OFF & 1.0
Plastic	Yield Stress	σ_y	OFF & 0.02

A.10. Hard Particulate (p.74)



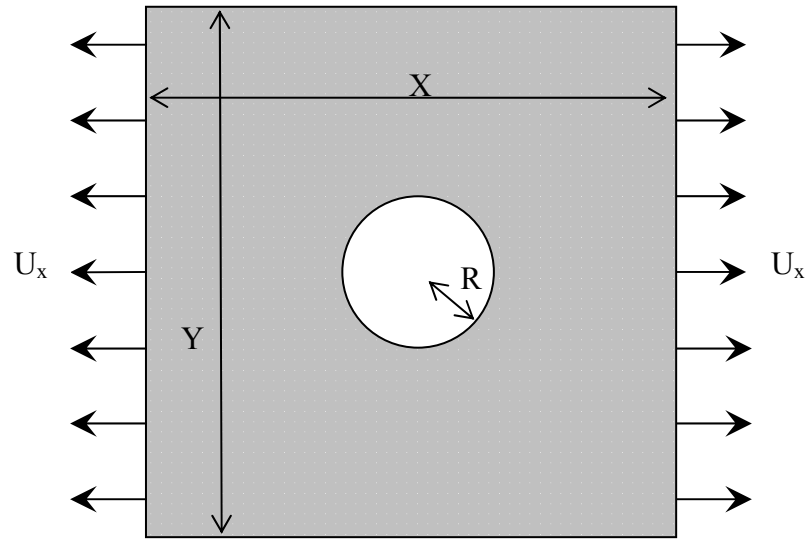
Property	U_y		Substrate	Particle
				(Corners)
Substrate	Particle Type A	X	120	
		Y	120	(40,60)
	Triangular Notch		(0,59)	(60,50)
			(0,61)	(70,70)
			(1,60)	(50,80)
Initial Velocities (particles/timestep)	Top Row (Constant)	U_x	0.001	
	Bottom Row (Const.)	U_x	-0.001	
Particle Type			A	B
Number of Particles		N	13827	570
Particle Mass		m_p	1.0	1.0
Density		ρ	1	1
Young's Modulus		E	1	2
Poisson's Ratio		ν	0.3	0.3
Speed of Sound (in Substrate)	$c = \sqrt{\frac{E(1-\nu)}{\rho(1+\nu)(1-2\nu)}}$	c	1.16	N/A
Artificial Viscosity	See (2.60), p.24	α		1.0
XSPH	See (3.2), p.30	$\tilde{\epsilon}$		0.5
Tensile Instability	See (3.6), p.41	n		6

A.11. Fibre Composite (p.75)



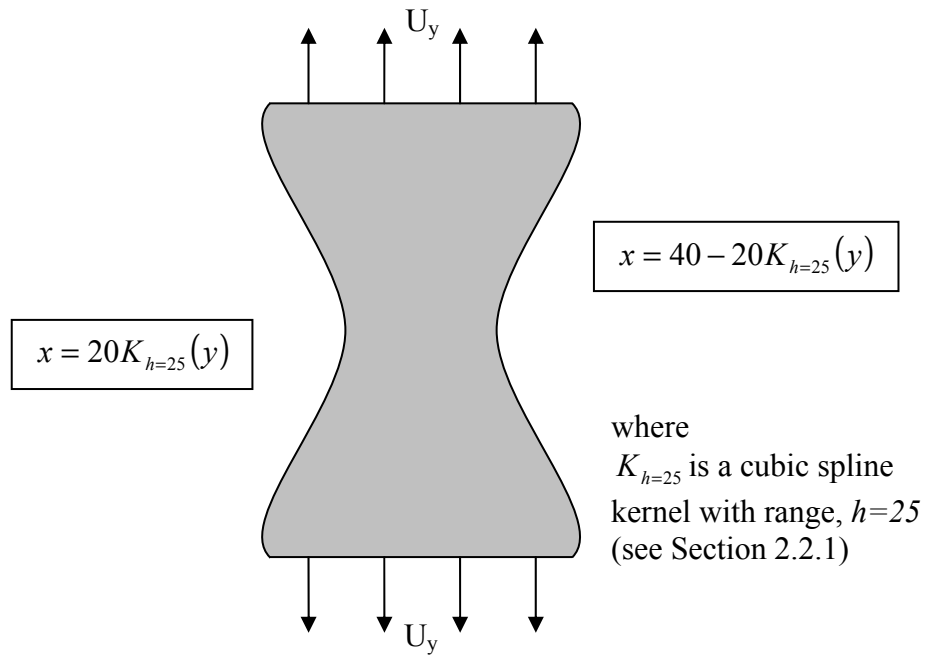
Property			Substrate	Fibres (Corners)
Substrate	Particle Type A	X	100	(50,47)
		Y	50	& (85,47)
	Triangular Notch		(0,24)	
			(0,26)	(85,47)
			(1,25)	& (89,3)
Initial Velocities (particles/timestep)	Top Row (Constant)	U_x	0.001	
	Bottom Row (Const.)	U_x	-0.001	
Particle Type			A	B
Number of Particles		N	4577	2*220
Particle Mass		m_p	1.0	1.0
Density		ρ	1	1
Young's Modulus		E	1	2
Poisson's Ratio		ν	0.3	0.3
Speed of Sound (in Substrate)	$c = \sqrt{\frac{E(1-\nu)}{\rho(1+\nu)(1-2\nu)}}$	c	1.16	N/A
Artificial Viscosity	See (2.60), p.24	α	1.0	
XSPH	See (3.2), p.30	$\tilde{\epsilon}$	0.5	
Tensile Instability	See (3.6), p.41	n	6	

A.12. Grady-Kipp Damage about a Circular Hole (p.80)



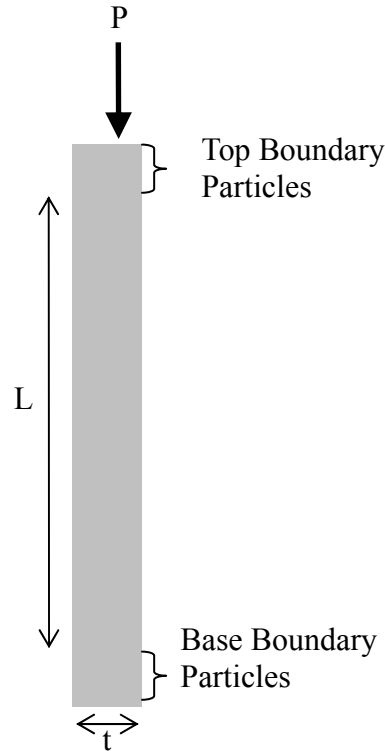
Property			Value
Total Domain (particles)		X	80
		Y	80
Centred Hole, Radius		R	10
Initial Velocity (particles/timestep)	Right Hand Side (Const.)	U_x	0.001
	Left Hand Side (Const.)	U_x	-0.001
Number of Particles		N	6090
Particle Mass		m_p	1.0
Density		ρ	1
Young's Modulus		E	1
Poisson's Ratio		ν	0.3
Speed of Sound (particles/timestep)	$c = \sqrt{\frac{E(1-\nu)}{\rho(1+\nu)(1-2\nu)}}$	c	1.16
Artificial Viscosity	See (2.60), p.24	α	1.0
XSPH	See (3.2), p.30	$\tilde{\epsilon}$	0.5
Tensile Instability	See (3.6), p.41	n	6
Grady-Kipp	(after Gray et al., 2004)	m	8.5
		k	$1.4 \times 10^{19} \text{ cm}^{-2}$

A.13. Damage about slim waisted sample (p.81)



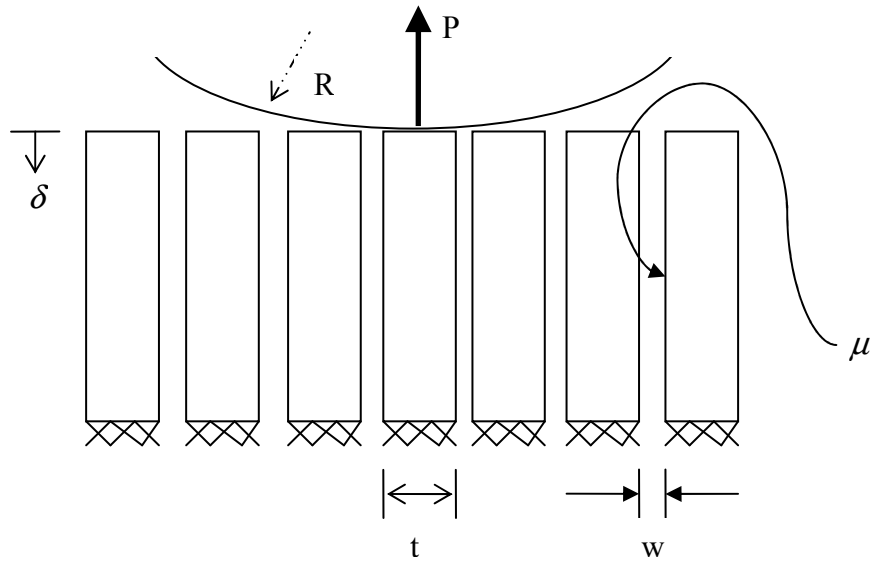
Property			Value
Total Domain (particles)		X	100
		Y	40
Bounded by kernel, K width 100 particles ($h=25$ particles)	Left Hand Side		$x = 20K_{h=25}(y)$
	Right Hand Side		$x = 40 - 20K_{h=25}(y)$
Initial Velocity (particles/timestep)	Top Row (Const.)	U_y	0.001
	Bottom Row (Const.)	U_y	-0.001
Number of Particles		N	3336
Particle Mass		m_p	1.0
Density		ρ	1
Young's Modulus		E	1
Poisson's Ratio		ν	0.3
Speed of Sound (particles/timestep)	$c = \sqrt{\frac{E(1-\nu)}{\rho(1+\nu)(1-2\nu)}}$	c	1.16
Artificial Viscosity	See (2.60), p.24	α	1.0
XSPH	See (3.2), p.30	$\tilde{\epsilon}$	0.5
Tensile Instability	See (3.6), p.41	n	6
Damage Parameters	see (5.4)	κ_0	0.001
		κ_c	0.01

A.14. Buckling Struts (p.92)



Property			Value
Total Domain (particles)		$L+6$	86, 78, 70, 62, 56 & 48
		t	4
Slenderness Ratio		λ	20 to 10
Initial Velocity (particles/timestep)	Top 3 Rows (Constant)	U_y	0.001
	Bottom 3 Rows (Const.)	U_y	0.0
Number of Particles		N	344 to 192
Particle Mass		m_p	1.0
Density		ρ	1
Young's Modulus		E	1
Poisson's Ratio		ν	0.3
Speed of Sound (particles/timestep)	$c = \sqrt{\frac{E(1-\nu)}{\rho(1+\nu)(1-2\nu)}}$	c	1.16
Artificial Viscosity	See (2.60), p.24	α	1.0
XSPH	See (3.2), p.30	$\tilde{\epsilon}$	0.5
Tensile Instability	See (3.6), p.41	n	6

A.15. Thermal Barrier Coatings (p103)



Property			Value
Number of Struts		horz	15
		vert	11
Each Strut (particles)	Strut Length	L	80
	Strut Thickness	t	2×2
	Width between Struts	w	0.02 to 0.4
Constant Velocity	Bottom 3 Rows	U_v	0.0
Central Indenter	Indenter Radius	R	20
	Velocity (Const.)	U_v	0.001c
Number of Particles		N	52800
Particle Mass		m_p	1.0
Density		ρ	1
Young's Modulus		E	1
Poisson's Ratio		ν	0.3
Speed of Sound (particles/timestep)	$c = \sqrt{\frac{E(1-\nu)}{\rho(1+\nu)(1-2\nu)}}$	c	1.16
Artificial Viscosity	See (2.60), p.24	α	1.0
XSPH	See (3.2), p.30	$\tilde{\epsilon}$	0.5
Tensile Instability	See (3.6), p.41	n	6
Penalty Force		R_{contact}	1.0
Coefficient of Friction		μ	0.0 to 1.0

References

Ashby & Jones; 1992; "Engineering Materials 2", Pergamon Press

Ashby, 1989; "Fundamental Principles of Fiber Reinforced Composites", Technomic Publishing.

Belytschko & Black, 1999; "Elastic Crack Growth in Finite Elements with Minimal Remeshing", Int. J. Numer. Meth. Engng 1999; 45: 601-620.

Bluhm, 1969; "Fracture Arrest", Fracture V, pg.1-63, Liebowitz ed., Academic Press

Bonet & Kulasegaram, 2002; "A simplified approach to enhance the performance of smooth particle hydrodynamics methods", Applied Math. & Compu. 126, 133-155.

Broek & Nederveen, 1964; "The influence of loading rate on the residual strength of aluminium alloy sheet specimens", Nat. Aerospace Inst. Amsterdam Rept TR-M-2154.

Broek, 1991; "Elementary Engineering Fracture Mechanics (4th Ed)", Kluwer Academic Publishing.

Bull, 1997; "Failure Mode Maps in the thin film Scratch Adhesion Test", Tribology Intern. 30, 491-498.

Capuzzo-Dolcetta & Lisio, 2000; "A criterion for the choice of the Interpolation Kernel in Smoothed Particle Hydrodynamics", Applied Num. Maths. 34, 363-371.

Chen, Hutchinson & Evans, 2004; "Simulation of the high temperature impression of thermal barrier coatings with columnar microstructure", Acta Mat. 52 p.565-571

Chen, Pan & Wu, 1997; "Large deformation analysis of rubber based on a reproducing kernel particle method", Comp. Mech., vol 19, no.3 Feb 1997.

Dilts, 1999; "Moving-least-squares-particle hydrodynamics I: Consistency and Stability", *Int. J. Numer. Methods Engrg.*, 44, p1115-1155

Fortino & Bilotta, 2004; "Evaluation of the amount of Crack Growth in 2D LEFM problems", *Engrg Fracture Mech.* 71, 1403-1419.

Gingold & Monaghan, 1977; "Smoothed Particle Hydrodynamics – Theory and application to non-spherical stars". *MNRAS* 181, p375-389

Grady & Kipp, 1980; "Continuum modelling of explosive fracture in oil shale". *International Journal of Rock Mechanics and Mining Sciences & Geomechanics Abstracts*, 17, p.147-157

Gray & Monaghan, 2004; "Numerical modelling of stress fields and fracture around magma chambers", *Journal of Volcanology and Geothermal Research*, 135, p.259-283
Gray, Monaghan & Swift, 2001; "SPH Elastic Dynamics", *Comput. Methods Appl. Mech. Engrg.* 190, 6641-6662.

Green, 2007; "CUDA Particles", NVIDIA Whitepaper, Nov. 2007

Griffith, 1921; 'The Phenomena of Rupture and Flow in Solids', *Phil. Trans.* A221, p.163-198.

Gross, 1975; "Special Theoretical Aspects of Dynamic Fracturing", *Ispra* [Abstract]

Guo & Nairn, 2004; "Calculation of J-Integral and Stress Intensity Factors using the Material Point Method", *CMES*, 1-13.

Hammouda, Sallam & Osman, 2004; "Significance of crack tip plasticity to early notch fatigue crack growth", *Int. J. of Fatigue* 26, 173-182.

Hass, 2000; "Directed Vapor Deposition of Thermal Barrier Coatings", Ph.D. Dissertation, University of Virginia. Viewable online at <http://www.ipm.virginia.edu/research/PVD/Pubs/thesis6/>

Hernquist & Katz, 1989; “TreeSPH: A unification of SPH with the Hierarchical Tree Method”, *Astrophysical J. Supp.*, 70, p.419-446.

Hogmark, Jacobson & Larsson, 2000; “Design and Evaluation of Tribological Coatings”, *WEAR*, 246, 20-33.

Hughes, Liu & Zimmermann, 1989; “Lagrangian-Eulerian Finite Element Formulation for Incompressible Viscous Flows.”, *Computer Methods in Applied Mechanics and Engineering* 1989; vol 29; 3: 329-349.

Irwin, 1957; “Analysis of Stresses and Strains near the end of a crack traversing a plate”, *Trans.ASME J.Appl.Mech.*, 24, p.361-364.

Jiang, Zhao & Sun, 2003; “Evaluation of Interfacial crack growth in bimaterial metallic joints loaded by symmetric three-point bending”, *Int. J. of Pressure Vessels and Piping* 80, 129-137.

Jimmack & Touheed, (n.d.); “An Introduction to MPI for Computational Mechanics” (extract).

Jones, 2006; “Buckling of Bars, Plates and Shells”, Bull Ridge Publishing, Blacksburg, Virginia, 2006.

Joyce, Reed & Syngellakis, 2003; “Numerical Modelling of crack shielding and deflection in a multi-layered material system”, *Materials Science and Engineering A342* (2003) 11-22.

Korsunsky, McGurk, Bull & Page, 1998; “On the Hardness of Coated Systems”, *Surface and Coatings Tech.* 99, 171-183.

Kowalenko, 2006; “Parallelization of SPH” Presentation at WCCM VII, Los Angeles, California, USA, 2006

Liu & Liu, 2010;”Smoothed Particle Hydrodynamics (SPH): an Overview and

Recent Developments”, Arch Comput Method Eng, 17, p.25-76

Mandell, Wingate & Schwalbe, 1996; “Simulation of a Ceramic Impact Experiment using the Sphinx Smooth Particle Hydrodynamics Code”, 16th Int. Symposium on Ballistics.

Monaghan, 1997; “SPH and Riemann Solvers”, J. Comp. Phys. 136, 298-307.

Monaghan, 1999; “SPH without a Tensile Instability”, J. Comp. Phys. 159, 290-311.

Mott, 1948; “Fracture of metals: some theoretical considerations”, Engineering, 165, p.16-18.

Oger & Savage, 1999; “Smoothed Particle Hydrodynamics for Cohesive Grains”, Comput. Methods Appl. Mech. Engrg. 180 (1999) 169-183.

Peerlings, 1999; “Enhanced damage modelling for fracture and fatigue”, Eindhoven: Technische Universiteit Eindhoven.

Philips, 2001; “Crystals, defects and microstructures : modeling across scales”, Cambridge University Press.

Rabczuk, Belytschko & Xioa, 2004; ”Stable particle methods based on Lagrangian kernels”, Comput. Methods Appl. Mech. Engrg., 193, p.1035-1063

Rao & Rahman, 2001; “A coupled meshless-finite element method for fracture analysis of cracks”, Int. J. of Pressure Vessels and Piping 78, 647-657.

Rice, 1968; “A path independent integral and the Approximate Analysis of Strain Concentration by Notches and Cracks”, J.Appl.Mech. 35, p.379-386.

Rodriguez-Paz & Bonet, 2003; “A Corrected Smooth Particle Hydrodynamics Method for the Simulation of Debris Flow”, Wiley Periodicals, Inc.

Schulz, Oettel & Bunk, 1996; "Texture of EB-PVD thermal barrier coatings under variable deposition conditions", *Z. Metallkd.*, 87, p.6

Schumacher et al., 2009; "A Hardware Accelerator for k-th Nearest Neighbor Thinning"; Paderborn Center for Parallel Computing, University of Paderborn Fuerstenallee 11, 33102 Paderborn, Germany.

Seo, Min & Lee, 2008;" Application of an improved contact algorithm for penetration analysis in SPH", *International Journal of Impact Engineering*, 35, p.578-588

Stolarska, Chopp, Moës & Belytschko, 2001; "Modelling crack growth by level sets in the extended finite element method", *Int. J. Numer. Meth. Engng* 2001; 51: 943-960.

Sulsky & Schreyer, 1996; "Axisymmetric form of the Material Point Method with applications to upsetting and Taylor Impact Problems", *Comput. Methods Appl. Mech. Engrg.*, 139, p.409-429

Synder, 2003; "Linux Clusters White Paper", IBM.

Ventura, Budyn & Belytschko, 2003; "Vector Level sets for descriptions of propagating cracks in finite elements", *Int. J. Numer. Meth. Engng* 2003; 58: 1571-1592.

Vertanen, 1999; "A parallel Implementations of a Fluid Flow Simulation using Smoothed Particle Hydrodynamics".

Wang, Lu, Hao & Chong (2005); "A full coupled numerical analysis approach for buried structures subject to subsurface blasts", *Computers and Structures*, 83, p.339-356.

Yang & Feng, 2004; "On the normal vector estimation for point cloud data from smooth surfaces", *Computer-Aided Design*, 37, p.1071-1079